Particulate Matter and Ozone: Remote Sensing and Source Attribution

Particulate matter and ozone: Remote sensing and source attribution

A dissertation presented

by

Sungshik Kim

to

The Department of Earth and Planetary Sciences

in partial fulfillment of the requirements

for the degree of

Doctor of Philosophy

in the subject of

Earth and Planetary Sciences

Harvard University

Cambridge, Massachusetts

April 2015

Dissertation Advisor: Professor Daniel J. Jacob Sungshik Kim

Particulate matter and ozone: Remote sensing and source attribution

Abstract

Particulate matter (PM) and tropospheric ozone are air pollutants that are harmful to human health and have broad implications for climate. Despite their importance, there remain large uncertainties related to their sources, evolution in the atmosphere, and impact downwind. In this thesis, I work to address some of these uncertainties through integrated analysis of ground, aircraft, and satellite observations and using both forward and inverse modeling approaches.

A new, high-resolution database of ozone-CO correlations was developed from two separate satellite platforms and was validated against in-situ profiles of the trace gases from commercial aircraft. These correlations were interpreted with a state-of-the-science global chemical transport model (CTM) to infer constraints on ozone sources. The observations supported the major source representation in the model for polluted North American outflow in June-July-August (combustion sources) and for the observed ozone maximum in the South Atlantic during December-January-February (lightning). A major model discrepancy was revealed over the North Pacific in summer and fall that was related to an overestimate of the natural lightning source and an underestimate of East Asian anthropogenic emissions.

Land clearing by fire in Equatorial Asia pollutes the air shed of one of the most densely populated regions in the world, but fires set in different areas have very different public health implications depending on the population downwind. Smoke exposure sensitivity to Equatorial Asian fires for several receptor locations was calculated with the adjoint of a global CTM. Peatswamp fires in southern Sumatra were found to be particularly detrimental to public health

for all years studied, implying that an effective land management policy protecting the remaining peatswamp forests would be of great air quality benefit. This approach can be used to estimate PM exposure for any future fire emission scenario and can be used to provide guidance for targeted land conservation in Equatorial Asia.

We use an ensemble of surface, aircraft, and satellite observations over the Southeast US during the summer-fall of 2013 together with the GEOS-Chem CTM at high resolution to better understand aerosol sources in the region and the relationship between surface PM and aerosol optical depth (AOD). Sulfate and organic aerosol (OA) are the main contributors to surface $PM_{2.5}$ (mass concentration of PM finer than 2.5 μm aerodynamic diameter) and AOD over the Southeast US, with OA acquiring an increasing role over the past decade as anthropogenic emissions have declined. Biogenic isoprene and monoterpenes are the dominant source of OA, and may contribute to sulfate formation through the production of Criegee intermediates as SO_2 oxidants. The vertical profile of aerosol extinction over the Southeast US follows closely that of aerosol mass. The SEAC4RS aircraft data demonstrate that the AODs measured from space are fundamentally consistent with surface $PM_{2.5}$. This implies that satellites can be used reliably to infer $PM_{2.5}$ air quality if a good CTM representation of the aerosol vertical distribution is available.

Table of Contents

Appendix

List of Tables

List of Figures

Acknowledgements

There are so many people that made my graduate career possible and not enough words for me to convey my gratitude.

I first thank my PhD advisor, Daniel Jacob, for his guidance over the past six years. He not only helped to dramatically improve my scientific reasoning, writing, and presentation skills by challenging me at every turn, but was also a constant advocate for me in the greater atmospheric chemistry community. This allowed me to work on several outstanding questions in the field through engaging collaborations that would have otherwise not been possible. I'd also like to thank my thesis committee: Jim Anderson, Scot Martin, and Kelly Chance.

I am grateful to the GEOS-Chem, Aura, SMOKE, and SEAC^{4}RS science teams. In particular, conversations with Randall Martin, Aaron van Donkelaar, Loretta Mickley, Miriam Marlier, Daven Henze, Xiong Liu, Kelly Chance, Jose Jimenez, Karl Froyd, and a host of other tremendous scientists and coauthors helped improve the results presented in this dissertation and they were in general just a fantastic group to work with. Thanks also to the DOE Office of Science for funding this work.

It has been a great privilege to be a part of the Atmospheric Chemistry Modeling Group. The combination of curiosity, intelligence, and kindness in the group is unrivaled and this is reflected in the science. Special thanks to Bob Yantosca and Melissa Suprizio, aka the backbone of GEOS-Chem. Thanks to past and current members including: Chris Holmes, Lin Zhang, Eric Leibensperger, Jenny Fisher, Lee Murray, Kevin Wecht, Eloise Marais, Mike Long, Helen Amos, Chris Miller, Shannon Koplitz, Katie Travis, Lei Zhu, Karen Yu, Alex Turner. You made the research fun.

A special thanks is in order to Brenda Mathieu for her help with day-to-day logistics – she is the reason the group runs as smoothly as it does. Thanks also to Sarah Colgan, Chenoweth Moffatt, Maryorie Grande, Cindy Marsh, and the entire EPS administration for fostering an academic environment that felt like a home away from home.

It is the transient nature of graduate school that people come and go, but during their stay have a profound impact on your life. I am especially grateful to John Crowley, Ben Lee, Hilary Close, Greg Santoni, Justin Parrella, Kristian Bergen, and Erik Chan for advice and distraction from the emotional lows of research.

I want to thank Jien Shim for her love, support, and patience over the past two years, particularly when we've been separated by distance. You were the biggest and most welcome surprise of my graduate school career and I can't help but look forward to our future together.

Last on this list, but first in my heart, I thank my family for their encouragement and support. To Su Jin, the best big sister a little brother could ask for. I am continually amazed at the sacrifices made and hardships faced by my parents, HeeMin and Yun Kim, raising two kids in a foreign country. Thanks – I think we came out okay and sorry for being so difficult and always wanting McDonalds.

This work is for all of you.

Chapter 1.

Overview

Particulate matter (PM) and tropospheric ozone are harmful air pollutants with implications for both human health and climate [*IPCC, 2007*]. Proper source attribution is necessary to inform regulatory action to mitigate these effects. Satellite observations provide dense spatial coverage of these pollutants and are a powerful resource when combined with forward and inverse modeling to better understand their sources, evolution in the atmosphere, and impact downwind, particularly in regions of the world where in-situ measurements are sparse [*Martin, 2008*].

1.1 PM and Ozone: Uncertainties and Implications

Tropospheric ozone is produced from the photochemical oxidation of carbon monoxide (CO), methane (CH_4), and non-methane volatile organic compounds (NMVOCs) in the presence of nitrogen oxides ($NO_x \equiv NO + NO_2$). Current global models can capture the observed large-scale spatial and seasonal patterns of ozone concentrations, but there is still large uncertainty in the driving factors, as reflected by the large differences between models in ozone production and loss rates [*Wild 2007; Wu et al., 2007*] and in source contributions [*Fiore et al., 2009*]. Reducing these uncertainties remains a top priority as it defines how much and in what way ozone can be controlled. This is particularly relevant in the United States today, with an EPA proposal under consideration that would strengthen the National Ambient Air Quality Standard (NAAQS) for ozone from 75 ppb to 65-70 ppb [*Federal Register, 2015*].

Long-term exposure to PM is associated with increased rates of morbidity and mortality [*Dockery et al., 1993; Pope et al., 2009*]. It is estimated that approximately 80% of the world population is exposed to PM levels above the World Health Organization's (WHO) Air Quality Guideline (AQG) and the burden is largest in industrializing nations [*van Donkelaar et al., 2010*]. Anthropogenic activity can significantly increase PM emissions to the atmosphere and degrade air quality downwind. A specific example is open fire burning for land clearing in Equatorial Asia, which is largely driven by the needs of the palm oil industry [*Koh et al., 2011; Mietinen et al., 2012*]. The resulting high smoke concentration affects one of the most densely populated regions of the world. Understanding the source-receptor relationships between where these fires are set and their impact downwind will be key to regional air quality management, but to date have not been fully quantified.

There is considerable interest in using satellite retrievals of aerosol optical depth (AOD), the column integrated light extinction by PM, to map concentrations in surface air [*Liu et al., 2004; H. Zhang et al., 2009; van Donkelaar et al., 2010; Hu et al., 2014*], particularly in regions of the world where in-situ observations are limited. The relationship between PM and AOD is a function of the vertical distribution and optical properties of the aerosol, and is often taken from a global chemical transport model (CTM) simulating the different aerosol types over the depth of the atmospheric column. Aerosol composition is generally dominated by sulfate and organic matter [Q. *Zhang et al., 2007; Jimenez et al., 2009*], thus it is important to evaluate the ability of CTMs to simulate these species and their vertical distributions.

1.2 Research Objectives and Approach

Satellite observations, combined with forward and inverse modeling techniques, are powerful tools that can be used to address uncertainties in PM and ozone source attribution.

A simple, yet effective method for ozone source attribution is to examine the relationship between ozone and CO. *Fishman and Seiler* [1983] first used the sign of the ozone-CO correlation in aircraft observations to distinguish between ozone produced photochemically in the troposphere (positive) and ozone transported down from the stratosphere (negative). Previous studies demonstrated these correlations can be retrieved from space [*Zhang et al., 2006; Voulgarakis et al., 2010*], but they were limited in their ability to infer ozone sources and transport due to sparse sampling and large random retrieval errors for individual scenes in the instrument used (the Tropospheric Emission Spectrometer or TES). The second chapter of this thesis is focused on improving on this situation by exploiting the synergy between two different instruments that are onboard the NASA A-Train constellation of satellites with the following objectives:

1. Develop a high-density global satellite database of ozone-CO correlations using data from the Ozone Monitoring Instrument [OMI; *Levelt et al., 2006*] and the Atmospheric Infrared Sounder [AIRS; *Aumann et al., 2003*], and explore its value for constraining our understanding of the factors controlling ozone.

The traditional method for determining source-receptor relationships in a CTM is to compare concentrations from a control model simulation and a sensitivity simulation where

emissions from a specific industry or region are excluded. If the number of receptors is small, it is far more efficient to approach the problem in reverse. This can be accomplished using the adjoint of the CTM, which allows model sensitivities to be traced back in time through the CTM fields [*Henze et al., 2007*]. In this approach, a single simulation with the adjoint model operating backward in time yields the complete time-dependent footprint of sources contributing to the concentration at a particular receptor site and for any averaging time. The third chapter of this thesis is focused on using this technique applied to smoke exposure in Equatorial Asia with the following objectives:

2. Use the adjoint of the GEOS-Chem CTM to map the sensitivity of smoke concentrations to fire location for selected urban receptor locations in Equatorial Asia to provide a basis to identify where fires could most effectively be restricted to reduce population exposure.

The NASA SEAC^{4}RS aircraft campaign based out of Houston, Texas in August-September 2013 [*Toon et al., 2015*] offers a comprehensive dataset for better understanding the relationship between surface PM and AOD measured from space. The aircraft payload included measurements of aerosol composition, size distributions, and light extinction. The combination of satellite, aircraft, and surface data provides unprecedented constraints. The final chapter of this thesis is focused on an integrated analysis of the multi-platform observations with the following objectives:

3. Use the GEOS-Chem CTM with 0.25^o x 0.3125^o horizontal resolution as a common platform to (1) determine the consistency between different measurements, (2) interpret

the measurements in terms of their implications for the sources and chemistry of aerosols in the Southeast US, (3) explain the seasonal aerosol cycle and the apparent inconsistency between satellite and aerosol measurements, and (4) assess the ability of CTMs to relate satellite measurements of AOD to surface PM concentrations.

1.3 Summary of Results

In Chapter 2 we show the new ozone-CO correlations are highly statistically significant and less noisy than previous satellite-based studies that used sparser data. Comparison to ozone-CO correlations and regression slopes (dO_3/dCO) from commercial aircraft profiles shows good general agreement. We interpret the observed correlations with the GEOS-Chem CTM to infer constraints on ozone sources (combustion, biosphere, stratosphere, and lightning) and demonstrate the utility of this approach for three case studies. The model reproduces the observed positive dO_3/dCO in the extratropical northern hemisphere in spring-summer, driven by combustion sources. Stratospheric influence there is also associated with a positive dO_3/dCO because of the interweaving of stratospheric downwelling with continental outflow. The well-known ozone maximum over the tropical South Atlantic is associated with negative dO_3/dCO in the observations; this feature is reproduced in GEOS-Chem and supports a dominant contribution from lightning to the ozone maximum. A major model discrepancy is found over the Northeast Pacific in summer-fall where dO_3/dCO is positive in the observations but negative in the model. We suggest that this reflects a model overestimate of lightning at northern mid-latitudes combined with an underestimate of the East Asian CO source.

In Chapter 3, we calculate smoke exposure sensitivity to Equatorial Asian fires for

several receptor locations with the adjoint of the GEOS-Chem CTM. We find that peatswamp fires in southern Sumatra are particularly detrimental to public health – Sumatra was responsible for 37% of total fire emissions in Equatorial Asia in 2006, but contributed to 64% of the smoke concentration in Singapore and 63% of the smoke concentration to which the whole Equatorial Asian population was exposed. We show that this disproportionate influence occurred in every year between 2004 and 2009, implying an effective land management policy protecting peatswamp forests in Southeast Sumatra would be of great air quality benefit. The adjoint sensitivities can be used to immediately infer population exposure to smoke for any future fire emission scenario and we demonstrate this for two land use projections for Sumatra. A "Green Vision" projection reduced mean smoke concentrations by a factor of 4 for Singapore and a factor of 2 for the population-weighted mean compared to a scenario with continued rapid plantation expansion. We argue these results can be used to provide guidance for targeted land conservation in Equatorial Asia.

In Chapter 4, we make use of surface, aircraft, and satellite observations over the Southeast US to better understand the relationship between surface PM and AOD measured from space. $PM_{2.5}$ (mass concentration of PM finer than 2.5 μm aerodynamic diameter) surface observations are fairly homogenous across the Southeast US, reflecting regional coherence in stagnation, mixing, and ventilation. Sulfate and organic aerosol (OA) account for the bulk of $PM_{2.5}$. The vertical profile of aerosol light extinction measured from the aircraft follows closely that of aerosol mass. MODIS and MISR satellite AOD retrievals show excellent agreement with surface-based AERONET observations. The overall analysis demonstrates consistency and closure between AODs measured from space and from the surface, aircraft aerosol extinction and mass profiles, and surface $PM_{2.5}$ measurements.

The previously reported summer-to-winter decrease in MODIS AOD data over the Southeast US is driven by a sharp August-to-October transition, in all years. This seasonal transition is caused by declines in both sulfate and OA, due to two common factors. First, a decline in isoprene and monoterpene emissions reduces biogenic secondary OA formation and SO_2 oxidation from the production of Criegee intermediates. Second, transition in the NO_x photochemical regime driven by a sharp drop in UV radiation titrates hydrogen peroxide and associated sulfate production, and also shifts the OA formation mechanism from low-NO_x to high-NO_x conditions.

Previous studies have pointed out an apparent inconsistency between the large seasonal variation of AOD measured from space and the much weaker seasonal variation of $PM_{2.5}$ measured at the surface. We find that this can be largely explained by the seasonal trend in PBL mixing and ventilation, dampening the effect of decreased wintertime PM sources on the surface concentrations. Overall our results show that AODs measured from space are fundamentally consistent with measurements of $PM_{2.5}$ air quality in the Southeast US. This implies that satellite measurements can reliably be used to infer $PM_{2.5}$ if a good CTM representation of PBL mixing and ventilation is available.

References

Aumann, H. H., et al. (2003), AIRS/AMSU/HSB on the Aqua Mission: Design, Science Objectives, Data Products, and Processing Systems, *IEEE T. Geosci. Remote, 41*, 253–264, doi:10.1109/TGRS.2002.808356.

Dockery, D. W., C. A. Pope, X. P. Xu, J. D. Spengler, J. H. Ware, M. E. Fay, B. G. Ferris Jr, and F. E. Speizer (1993), An association between air pollution and mortality in six U.S. cities, *N. Engl. J. Med.*, *329*(24), 1753–1759, doi:10.1056/NEJM199312093292401.

Federal Register (2015), National Ambient Air Quality Standards for Ozone, published online December 2014, retrieved on March 29, 2015 from https://www.federalregister.gov/articles/2014/12/17/2014-28674/national-ambient-air-quality-standards-for-ozone

Fiore, A. M., et al. (2009), Multimodel estimates of intercontinental source receptor relationships for ozone pollution, *J. Geophys. Res., 114*, D04301, doi:10.1029/2008JD010816.

Fishman, J., and W. Seiler (1983), Correlative nature of ozone and carbon monoxide in the troposphere: implications for the tropospheric ozone budget, *J. Geophys. Res., 88*, 3662–3670, doi:10.1029/JC088iC06p03662.

Henze, D. K., A. Hakami, and J. H. Seinfeld (2007), Development of the adjoint of GEOS-Chem, *Atmos. Chem. Phys., 7*, 2413-2433, doi:10.5194/acp-7-2413- 2007.

Hu, X., L. A. Walker, A. Lyapustin, Y. Wang, and Y. Liu (2014), 10-year spatial and temporal trends of $PM_{2.5}$ concentrations in the southeastern US estimated using high-resolution satellite data, *Atmos. Chem. Phys., 14,* 6301-6314, doi:10.5194/acp-14-6301-2014.

IPCC (2007), Climate Change 2007: The Physical Scientific Basis, Contribution of Working Group I to the Fourth Assessment Report of the Intergovernmental Panel on Climate Change, edited by: Solomon, S., et al., Cambridge University Press, Cambridge, United Kingdom and New York, NY, USA.

Jimenez, J., et al. (2009), Evolution of organic aerosols in the atmosphere, *Science, 326*(5959), 1525-1529, doi:10.1126/science.1180353.

Koh, L. P., and J. Ghazoul (2010), Spatially explicit scenario analysis for reconciling agricultural expansion, forest protection, and carbon conservation in Indonesia, *Proc. Natl. Acad. Sci., 107,* 11140-11144, doi:10.1073/pnas.1000530107.

Levelt, P. F., G. H. J. van den Oord, M. R., Dobber, A. Malkki, H. Visser, J. de Vries, P. Stammes, J. O. V. Lundell, and H. Saari (2006), The Ozone Monitoring Instrument, *IEEE T. Geosci. Remote*, *44*, 1093–1101, doi:10.1109/TGRS.2006.872333.

Liu Y., R. J. Park, D. J. Jacob, Q. Li, V. Kilaru, and J. A. Sarnat (2004), Mapping annual mean ground-level $PM_{2.5.}$ concentrations using Multiangle Imaging Spectroradiometer aerosol optical thickness over the contiguous United States, *J. Geophys, Res., 109,* D22206,

doi:10.1029/2004JD005025.

Martin, R. (2008), Satellite remote sensing of surface air quality, *Atmos. Environ., 42,* 7823-7843, doi:10.1016/j.atmosenv.2008.07.018.

Mietinnen, J., A. Hooijer, C. Shi, D. Tollenaar, R. Vernimmen, S. C. Liew, C. Malins, and S. E. Page (2012), Extent of industrial plantations on Southeast Asian peatlands in 2010 with analysis of historical expansion and future projections, *GCB Bioenergy, 4,* 908-918, doi:10.1111/j.1757-1707.2012.01172.x.

Pope III, C. A., M. Ezzati, and D. W. Dockery (2009), Fine-particulate air pollution and life expectancy in the United States, *N. Engl. J. Med., 360*(4), 376–386, doi:10.1056/NEJMsa0805646.

Toon, O. B., et al. (2015), Planning, implementation, and scientific goals of the Studies of Emissions and Atmospheric Composition, Clouds, and Climate Coupling by Regional Surveys ($SEAC^4RS$) field mission, in prep.

van Donkelaar, A., R. V. Martin, M. Brauer, R. Kahn, R. Levy, C. Verduzco, and P. J. Villeneuve (2010), Global estimates of ambient fine particulate matter concentrations from satellite-based aerosol optical depth: development and application, *Environ. Health Perspect., 118(6),* 847-855, doi:10.1289/ehp.0901623.

Voulgarakis, A., P. J. Telford, A. M. Aghedo, P. Braesicke, G. Faluvegi, N. L., Abraham, K. W. Bowman, J. A. Pyle, D. T. Shindell (2010), Global multi-year O_3-CO correlation patterns from models and TES satellite observations, *Atmos. Chem. Phys., 11*, 5819–5838, doi:10.5194/acp-10-2491-2010.

Wild, O. (2007), Modeling the global tropospheric ozone budget: exploring the variability in current models, *Atmos. Chem. Phys., 7*, 2643–2660, doi:10.5194/acp-7-2643-2007.

Wu, S., L. J. Mickley, D. J. Jacob, J. A. Logan, R. M. Yantosca, and D. Rind (2007), Why are there large differences between models in global budgets of tropospheric ozone?, *J. Geophys. Res., 112*, D05302, doi:10.1029/2006JD007801.

Zhang, H., R. M. Hoff, and J. A. Engel-Cox (2009), The relation between Moderate Resolution Imaging Spectroradiometer (MODIS) aerosol optical depth and $PM_{2.5}$ over the United States: a geographical comparison by U.S. Environmental Protection Agency regions, *J. Air Waste Manage. Assoc.,* 59:11, 1358-1369, doi:10.3155/1047-3289.59.11.1358.

Zhang, L., et al. (2006), Ozone-CO correlations determined by the TES satellite instrument in continental outflow regions, *Geophys. Res. Lett., 33*, L18804, doi:10.1029/2006GL026399.

Zhang, Q., et al. (2007), Ubiquity and dominance of oxygenated species in organic aerosols in anthropogenically-influenced Northern Hemisphere midlatitudes, *Geophys. Res. Lett., 34,* L13801, doi:10.1029/2007GL029979.

Chapter 2.

Global ozone-CO correlations from OMI and AIRS: constraints on tropospheric ozone sources[1]

Abstract

We present a global data set of free tropospheric ozone-CO correlations with $2^o \times 2.5^o$ spatial resolution from the Ozone Monitoring Instrument (OMI) and Atmospheric Infrared Sounder (AIRS) satellite instruments for each season of 2008. OMI and AIRS have near daily global coverage of ozone and CO respectively and observe coincident scenes with similar vertical sensitivities. The resulting ozone-CO correlations are highly statistically significant (positive or negative) in most regions of the world, and are less noisy than previous satellite-based studies that used sparser data. Comparison with ozone-CO correlations and regression slopes (dO_3/dCO) from MOZAIC aircraft profiles shows good general agreement. We interpret the observed ozone-CO correlations with the GEOS-Chem chemical transport model to infer constraints on ozone sources. Driving GEOS-Chem with different meteorological fields generally shows consistent ozone-CO correlation patterns, except in some tropical regions where the correlations are strongly sensitive to model transport error associated with deep convection. GEOS-Chem reproduces the general structure of the observed ozone-CO correlations and regression slopes, although there are some large regional discrepancies. We examine the model sensitivity of dO_3/dCO to different ozone sources (combustion, biosphere, stratosphere, and

[1]Kim, P. S., D. J. Jacob, X. Liu, J. X. Warner, K. Yang, K. Chance, V. Thouret, and P. Nedelec (2013), Global ozone-CO correlations from OMI and AIRS: constraints on tropospheric ozone sources, *Atmos. Chem. Phys., 13,* 9321-9335, doi:10.5194/acp-13-9321-2013.

lightning NO_x) by correlating the ozone change from that source to CO from the standard simulation. The model reproduces the observed positive dO_3/dCO in the extratropical northern hemisphere in spring-summer, driven by combustion sources. Stratospheric influence there is also associated with a positive dO_3/dCO because of the interweaving of stratospheric downwelling with continental outflow. The well-known ozone maximum over the tropical South Atlantic is associated with negative dO_3/dCO in the observations; this feature is reproduced in GEOS-Chem and supports a dominant contribution from lightning to the ozone maximum. A major model discrepancy is found over the Northeast Pacific in summer-fall where dO_3/dCO is positive in the observations but negative in the model, for all ozone sources. We suggest that this reflects a model overestimate of lightning at northern mid-latitudes combined with an underestimate of the East Asian CO source.

2.1 Introduction

Tropospheric ozone is produced by the photochemical oxidation of carbon monoxide (CO), methane (CH_4), and non-methane volatile organic compounds (NMVOCs) in the presence of nitrogen oxides ($NO_x \equiv NO + NO_2$). It is a potent greenhouse gas and harmful surface air pollutant, with implications for climate, human health, and agricultural productivity [*IPCC, 2007*]. Current global models can capture the observed large-scale spatial and seasonal patterns of ozone concentrations but there is large uncertainty in the driving factors, as reflected by the large differences between models in ozone production and loss rates [*Wild, 2007; Wu et al., 2007*] and in source contributions [*Fiore et al., 2009*]. We present here a high-density global satellite database of ozone-CO correlations using data from the Ozone Monitoring Instrument

[OMI; *Levelt et al., 2006*] and the Atmospheric Infrared Sounder [AIRS; *Aumann et al., 2003*], and explore its value for constraining our understanding of the factors controlling ozone.

Many studies have used ozone-CO correlations derived from in situ observations to constrain ozone sources and transport. CO is emitted from incomplete combustion and has an atmospheric lifetime of a few months against oxidation. *Fishman and Seiler* [1983] first used the sign of the ozone-CO correlation in aircraft observations to distinguish between ozone produced photochemically in the troposphere (positive) and transported down from the stratosphere (negative). Positive surface air correlations observed in aged pollution and biomass burning plumes have been used to infer ozone production efficiencies (OPEs) and continental export [*Parrish et al., 1993; Chin et al., 1994; Hirsch et al., 1996; Mao and Talbot, 2004; Jaffe and Wigder, 2012*]. Negative correlations may result from ozone chemical loss and surface deposition [*Cardenas et al., 1998; Parrish et al., 1998; Harris et al., 2000*]. Observations from aircraft and remote mountain sites show that ozone-CO correlations extend into the free troposphere and on intercontinental scales, although they then reflect mixing of air masses as well as chemistry [*Andreae et al., 1994; Mauzerall et al., 1998; Zahn et al., 2002; Honrath et al., 2004; Hudman et al., 2007*]. Interleaving of stratospheric intrusions with polluted continental outflow can complicate the fine-scale correlations in the free troposphere [*Parrish et al., 2000; Nowak et al., 2004; Price et al., 2004; Liang et al., 2007*].

Coincident satellite observations providing global coverage of ozone and CO have become available over the past decade from the NASA A-Train constellation. The vertical resolution of satellite retrievals is typically limited to 1-2 pieces of information in the troposphere. *Zhang et al.* [2006] first demonstrated that ozone-CO correlations could be derived from Tropospheric Emission Spectrometer (TES) retrievals of the mid-troposphere [*Beer et al.,*

2001]. *Hegarty et al.* [2009, 2010] examined ozone-CO correlations from TES grouped by the predominant synoptic circulation patterns over North America, and found a well-defined positive relationship in continental export in spring-summer. *Voulgarakis et al.* [2011] used TES data from 2005-2008 to derive global ozone-CO correlation statistics for December-January and July-August, and compared to results from two global models. They concluded that a systematic underestimate of the TES-derived ozone-CO correlations by the UKCA model was likely caused by model transport errors.

All previous ozone-CO correlation analyses from space have used ozone and CO satellite data from the TES instrument. A drawback is the limited coverage of TES due to lack of cross-track scanning. Individual satellite retrievals have large random error, compromising correlation analyses unless large ensembles are considered. Correlation analyses using TES have had to aggregate the data over ~1,000 km spatial domains and/or over several years. Even so, the random retrieval error is problematic when diagnosing ozone-CO correlations [*Zhang et al., 2006*].

In this work, we produce a new database of ozone-CO correlations from space using ozone retrievals from OMI and CO retrievals from AIRS. These two instruments aboard the NASA A-Train observe the same scenes with near-coincidence (<15 minutes). They use different spectral bands (OMI in the UV, AIRS in the thermal IR) but their vertical sensitivities are similar. Both provide near-daily global coverage. This allows us to calculate robust statistical relationships between ozone and CO with much less error and finer spatiotemporal resolution than previous satellite studies. We evaluate the resulting product with ozone-CO correlation data from MOZAIC aircraft profiles (www.iagos.fr). Here we present global ozone-CO correlations for each season of 2008 on a $2^{o} \times 2.5^{o}$ grid, and we use the global GEOS-Chem chemical

transport model (CTM) to interpret these correlations. A subsequent paper will examine interannual variability.

2.2 Data and Methods

2.2.1 OMI

The OMI instrument is onboard the NASA Aura satellite with an equator crossing time of ~13:45 LT. It measures solar backscatter at 270-500 nm. The nadir footprint is 13 × 24 km^2, with near-daily global coverage from its 2600 km cross-track pushbroom scanner. We use the Level 2G product of PROFOZ ozone profile retrievals by *X. Liu et al.* [2010], with a few major modifications described below. This retrieval is based on the optimal estimation method of *Rodgers* [2000]. It reports partial ozone columns for 24 layers extending from the surface to ~0.1 hPa. The retrieved vertical profile of partial ozone columns, described by the vector $\hat{\mathbf{x}}$, can be expressed as

$$\hat{\mathbf{x}} = \mathbf{A}\mathbf{x} + (\mathbf{I} - \mathbf{A})\mathbf{x_a} + \boldsymbol{\epsilon} \qquad [1]$$

where **A** is the averaging kernel matrix, **x** is the true vertical profile, **I** is the identity matrix, $\mathbf{x_a}$ is the a priori estimate, and $\boldsymbol{\epsilon}$ is the retrieval error. The averaging kernel matrix represents the sensitivity of the retrieval to the true profile.

To speed up processing, the retrieval is done here at a nadir resolution of 52 × 48 km^2 by averaging (co-adding) 4 / 8 OMI UV1 (270-310 nm) / UV2 (310-330 nm) pixels. A major change to the retrieval presented by *X. Liu et al.* [2010] is the constraint on measurement error.

Recent downward revision of the OMI measurement error [*Braak, 2010*], together with further reduction of this error through co-adding, results in unrealistically small observational error specification (~0.035% at 320 nm under tropical clear conditions) that causes spurious variability in the retrieval. This is most likely due to other unaccounted measurement and forward modeling errors. Therefore a minimum measurement error of 0.2% in the spectral region of 300-330 nm is imposed. In addition, *X. Liu et al.* [2010] used effective O_3 cross-sections and performed calculations at the OMI spectral grid resolution, which causes radiance errors up to 0.2-0.6% at some wavelengths (with spectral position and magnitude errors varying with solar zenith angle). In the new algorithm, the radiative transfer calculation is done using VLIDORT [*Spurr, 2006*] as in *X. Liu et al.* [2010], but is now performed at selected wavelengths, interpolated to a fine grid of 0.05 nm using weighting functions, and is then convolved with OMI slit functions. This new scheme can reduce the radiance errors to typically less than 0.1%.

The PROFOZ retrievals typically have 0.5-1.0 degrees of freedom for signal (DOFS), usually peaking at 700-500 hPa. We filter out poor retrievals by requiring that the average and root mean square (RMS) fitting residuals provided by the retrieval for the UV-2 channel be less than 3% of the measurement error, and we also exclude data poleward of 60° due to high solar zenith angles.

The a priori estimate for the PROFOZ retrieval uses the *McPeters et al.* [2007] ozone profile climatology, which depends on calendar month and latitude. This adds variability to the retrieved profiles that is not actually measured. We remove this variability as in *Zhang et al.* [2006] by reprocessing the OMI retrievals to use a fixed a priori profile everywhere, which we choose as the mean annual *McPeters et al.* [2007] profile for 30° S - 30° N.

Intercomparison of the OMI PROFOZ and TES ozone retrievals by *Zhang et al.* [2010]

shows that the two exhibit similar geographic and seasonal variability with differences generally within ±10 ppbv. Validation of the OMI PROFOZ retrieval with ozonesonde profiles shows a global mean positive bias of 2.8 ppb in the troposphere [*Zhang et al., 2010*], which we subtract from the retrieved values.

2.2.2 AIRS

The AIRS instrument is onboard the NASA Aqua satellite with an equator crossing time of ~13:30 LT. AIRS retrieves CO by observing thermal emission around the 4.7 μm vibrational fundamental band. We use the Level 2 CO profiles from the version 5 (v5) AIRS retrieval (available for download through ftp://airspar1u.ecs.nasa.gov). A detailed description of the retrieval algorithm is available in *Susskind et al.* [2003]. We use the Support retrieval product, which includes higher resolution profiles than the Standard product, reporting CO partial columns on 100 pressure levels between 1100 and 0.016 hPa. AIRS CO retrievals typically have ~0.8 DOFS with sensitivity generally peaking between 600 and 300 hPa [*Warner et al., 2007*]. The AIRS a priori is a fixed vertical profile from *Deeter et al.* [2003] up to 10.25 hPa and from the Air Force Geophysics Laboratory (AFGL) standard atmosphere profile above.

Validation of the AIRS v5 retrieval with aircraft vertical profiles shows a positive bias of 6-10% in the northern hemisphere [*McMillan et al., 2011*] with a larger positive bias in the southern hemisphere [*Yurganov et al., 2008, 2010; Warner et al., 2010*]. To correct for this bias we scale AIRS profiles down by 10%. We remove retrievals that do not have quality flag QA = 0 provided in the retrieval product as well as any profiles with surface temperature reported as less than 250 K. For consistency with OMI, we limit our analysis to the daytime retrievals.

2.2.3 GEOS-Chem

We use the GEOS-Chem global CTM (version 9-01-02, http://geos-chem.org), originally described by *Bey at al.* [2001] and *Park et al.* [2004], to interpret the observed satellite ozone-CO relationships. GEOS-Chem is driven by Goddard Earth Observing System (GEOS-5) assimilated meteorological data from the NASA Global Modeling and Assimilation Office (GMAO). The GEOS-5 meteorological data have a native horizontal resolution of 0.5° × 0.67° with 72 vertical pressure levels and 6-h temporal frequency (3-h for surface variables and mixing depths). We degrade the horizontal resolution to 2° × 2.5° for input to GEOS-Chem. The model results presented here are for 2008 following a 1-year initialization.

Global anthropogenic emissions of CO, NO_x, and SO_2 are from the EDGAR 3.2 monthly inventory for 2000 [*Olivier and Berdowski, 2001*] while anthropogenic NMVOC emissions are from the RETRO monthly global inventory for 2000 [*van het Bolscher et al., 2008*]. The default inventories are scaled for subsequent years on the basis of economic data [*van Donkelaar et al., 2008*] and regional overwrites are used where available. These include the US EPA NEI inventory for 2005, Asian emissions from *Q. Zhang et al.* [2009] for 2006, the EMEP inventory for Europe [*Vestreng and Klein, 2002*] for 2005, the CAC emission inventory for Canada for 2005, and the BRAVO emission inventory for Mexico [*Kuhns et al., 2005*] for 1999. Global shipping emissions are from ICOADS, as implemented in GEOS-Chem by *Lee et al.* [2011]. Global biofuel emissions are from *Yevich and Logan* [2003]. Biomass burning emissions are from the Global Fire Emission Database version 3 (GFED3) inventory with monthly resolution [*Giglio et al., 2010; van der Werf et al., 2010*]. Biogenic VOC emissions are from the Model of Emissions of Gases and Aerosols from Nature (MEGAN) inventory of *Guenther et al.* [2006]. The present simulation also includes conversion of HO_2 to H_2O in aerosol particles [*Mao et al.,*

2013].

Lightning NO_x emissions are constrained by an OTD/LIS climatology of lightning flash observations from satellites as described by *Sauvage et al.* [2007] and *Murray et al.* [2012], with timing and vertical distribution determined by GEOS-Chem deep convection. The global lightning NO_x source is 6 Tg N a^{-1} [*Martin et al., 2007*] with higher NO_x yield per flash at northern mid-latitudes compared to the tropics [*Hudman et al., 2007*].

Vertical profiles of ozone and CO in the stratosphere are simulated in GEOS-Chem using GEOS-5 transport, as in the troposphere, but with climatological production and loss rate constants. Production and loss rate constants for ozone in the stratosphere are computed locally with the Linoz algorithm of *McLinden et al.* [2000], while those for CO are specified on a monthly basis from the 2-D model of *Schneider et al.* [1999].

Previous evaluations of the ozone and CO simulations with OMI and AIRS by *Zhang et al.* [2010] and *Kopacz et al.* [2010] showed that GEOS-Chem is in general consistent with observations. However, several regional biases were apparent in these studies. In particular, the ozone simulation of *Zhang et al.* [2010] underestimated ozone in the tropics while overestimating ozone in the northern subtropics and southern mid-latitudes. We will discuss these biases in the context of the present simulation below.

2.2.4 Correlation Statistics

We average the individual OMI ozone and AIRS CO profile retrievals over a 2° × 2.5° horizontal grid, based on the center of the satellite footprint, for each day of 2008. We focus on the 700-400 hPa columns, where both instruments have maximum sensitivity. These are computed by adding the corresponding partial columns in the retrievals, with linear interpolation

as necessary. For clarity of presentation, we convert the partial columns to the corresponding column mixing ratios. We compute the 700-400 hPa DOFS by adding the corresponding elements of the diagonal of the averaging kernel matrix and remove scenes with DOFS less than 0.1.

We compute seasonal ozone-CO correlation statistics, specifically the correlation coefficient (*r)* and unweighted reduced-major-axis (RMA) regression slope (dO_3/dCO), for the 3-month time series (DJF, MAM, JJA, SON) of the ozone and CO mixing ratios for each grid square.

For comparison to the satellite data, we archive GEOS-Chem daily output at the local satellite overpass time and regrid it vertically to the instrument retrieval levels. Since GEOS-Chem has little predictive capability in the stratosphere due to the use of climatological chemical rates, we replace the simulated profiles above the tropopause with the observed profiles as in *Zhang et al.* [2006]. The simulated ozone and CO profiles are then smoothed with the instrument averaging kernels to account for the measurement sensitivity. The ozone-CO statistics from GEOS-Chem are calculated using the same methodology as the satellite data described above.

Random noise in individual ozone and CO profile retrievals degrades the ozone-CO correlations but this can be greatly reduced by averaging (central limit theorem). The high density of OMI and AIRS observations is of considerable advantage for this purpose. After data filtering, there are typically 10-30 OMI and AIRS profiles binned daily in each $2^o \times 2.5^o$ grid square where data are available, with more profiles at lower latitudes. Tests applying random retrieval error to the GEOS-Chem profiles, as in *Zhang et al.* [2006], indicate little effect of retrieval noise on the simulated ozone-CO correlations from OMI and AIRS. This is in contrast

to the TES results of *Zhang et al.* [2006] and *Voulgarakis et al.* [2011] where the correlations were found to be significantly degraded by that noise.

2.2.5 Evaluation with MOZAIC Aircraft Data

We evaluate the ozone-CO correlations and regression slopes derived from OMI/AIRS with in-situ aircraft profiles over commercial airports in 2006 and 2008 from the Measurements of OZone, water vapour, carbon monoxide and nitrogen oxides by in-service AIrbus airCraft (MOZAIC) program [*Marenco et al., 1998*; www.iagos.fr]. MOZAIC ascent/descent profiles extend up to a permanent 12 km limit. The profiles are vertically interpolated to the satellite retrieval grids and smoothed with the mean instrument averaging kernel matrix for the corresponding day and 2° × 2.5° horizontal gridsquare. The 700-400 hPa ozone and CO mixing ratios are then calculated for MOZAIC in the exact same manner as for the OMI/AIRS data described in Section 2.4. We require at least 10 MOZAIC vertical profiles with coincident satellite data at a site in a given season to derive ozone-CO correlations. This requirement is satisfied in those two years for three MOZAIC sites in Europe (Frankfurt, London, Vienna), four sites in the US (Atlanta, Dallas, Philadelphia, Portland), two sites in Asia (Hyderabad, Tokyo), and one site in Africa (Windhoek). Only Windhoek, Namibia has sufficient data for all four seasons.

2.3 Global Ozone-CO Correlation Patterns

Figure 2.1 shows global maps of the 2008 seasonal mean mixing ratios for AIRS CO and OMI ozone at 700 – 400 hPa. CO is highest over and downwind of combustion source regions

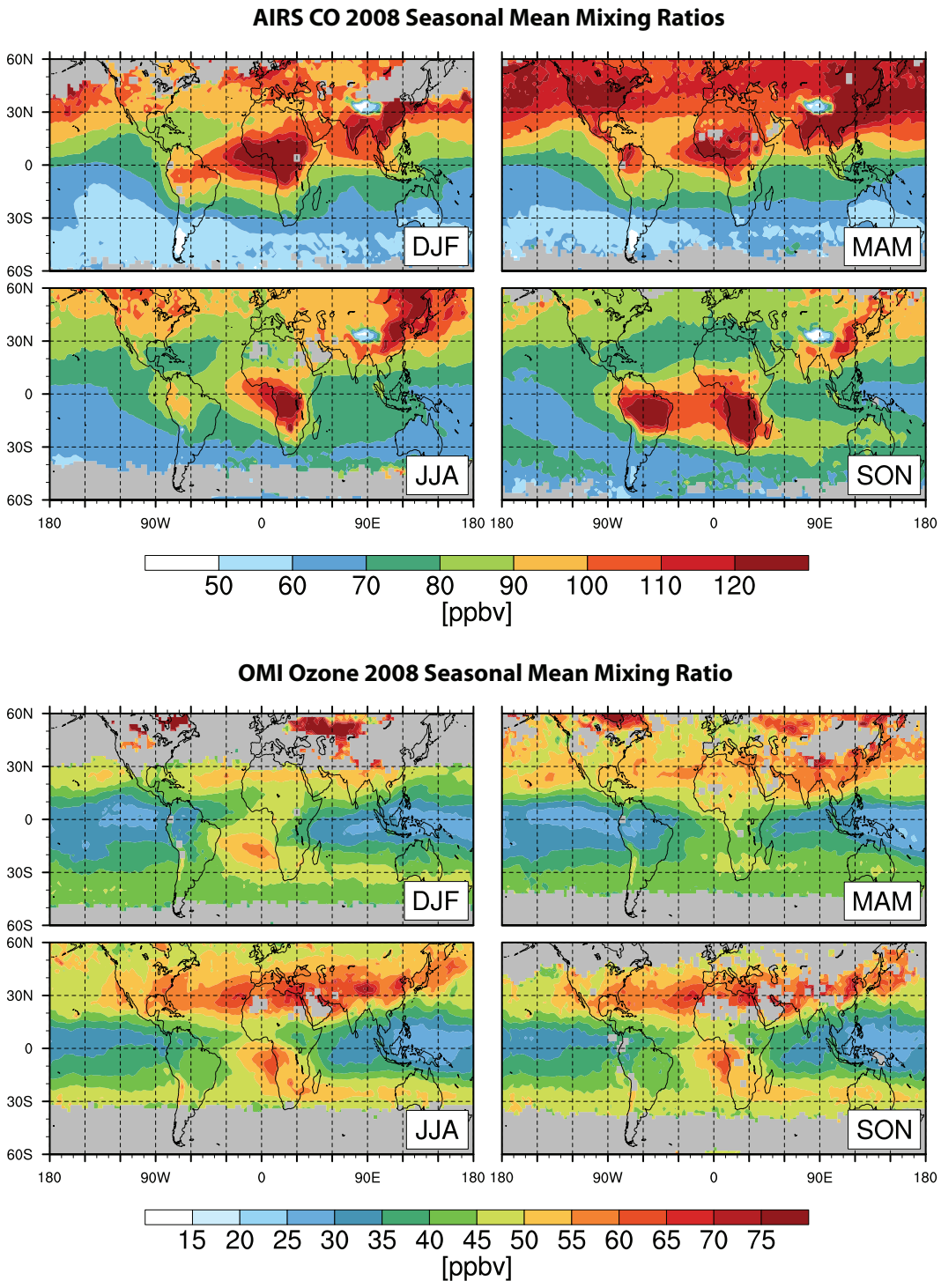

Figure 2.1: (Top) Seasonal mean AIRS CO mixing ratios at 700-400 hPa for 2008. Data are plotted on the $2^{o} \times 2.5^{o}$ GEOS-Chem grid. Gray indicates insufficient data. (Bottom) Same but for OMI ozone mixing ratios at 700-400 hPa.

(fossil fuel, seasonal fires). The spring maximum is primarily driven by photochemical loss of CO from reaction with OH. Ozone features include the well-known spring-summer maximum in the northern extratropics [*Monks, 2000*] and minimum over the tropics except for biomass burning regions and the South Atlantic [*Martin et al., 2002*]. Ozone at southern mid-latitudes peaks in winter-spring, reflecting a combination of stratospheric and biomass burning influences [*Zhang et al., 2010*].

Comparison of **Figure 2.1** to the corresponding seasonal mean distributions for ozone and CO simulated by GEOS-Chem (see **Appendix**) shows that the model generally reproduces the large-scale patterns and seasonal cycles of both species. Biases in the ozone simulation are similar to those reported by *Zhang et al.* [2010].

Figures 2.2 and **2.3** show the observed seasonal ozone-CO correlation coefficients and RMA regression slopes (dO_3/dCO) from OMI and AIRS and compares them to the corresponding GEOS-Chem values. The correlations are in general highly statistically significant. Strong positive correlations are observed in all seasons in the northern subtropics, particularly downwind of the continents. The strongest correlations are in MAM and JJA, with r exceeding 0.8 over the western Pacific. GEOS-Chem shows prominent discrepancies over Eurasia and the Northeast Pacific in JJA and SON where model correlations are negative. Quantitative discussion of correlations over the North Atlantic and Northeast Pacific will be presented in the next section.

Observed correlations in the tropics show positive or negative values depending on region. Positive correlations in the northern tropics appear to be an extension of the subtropics. The strongest negative correlation is over the Caribbean in JJA, with r exceeding -0.7. This reflects lightning influence as discussed below. The well-known ozone maximum over the

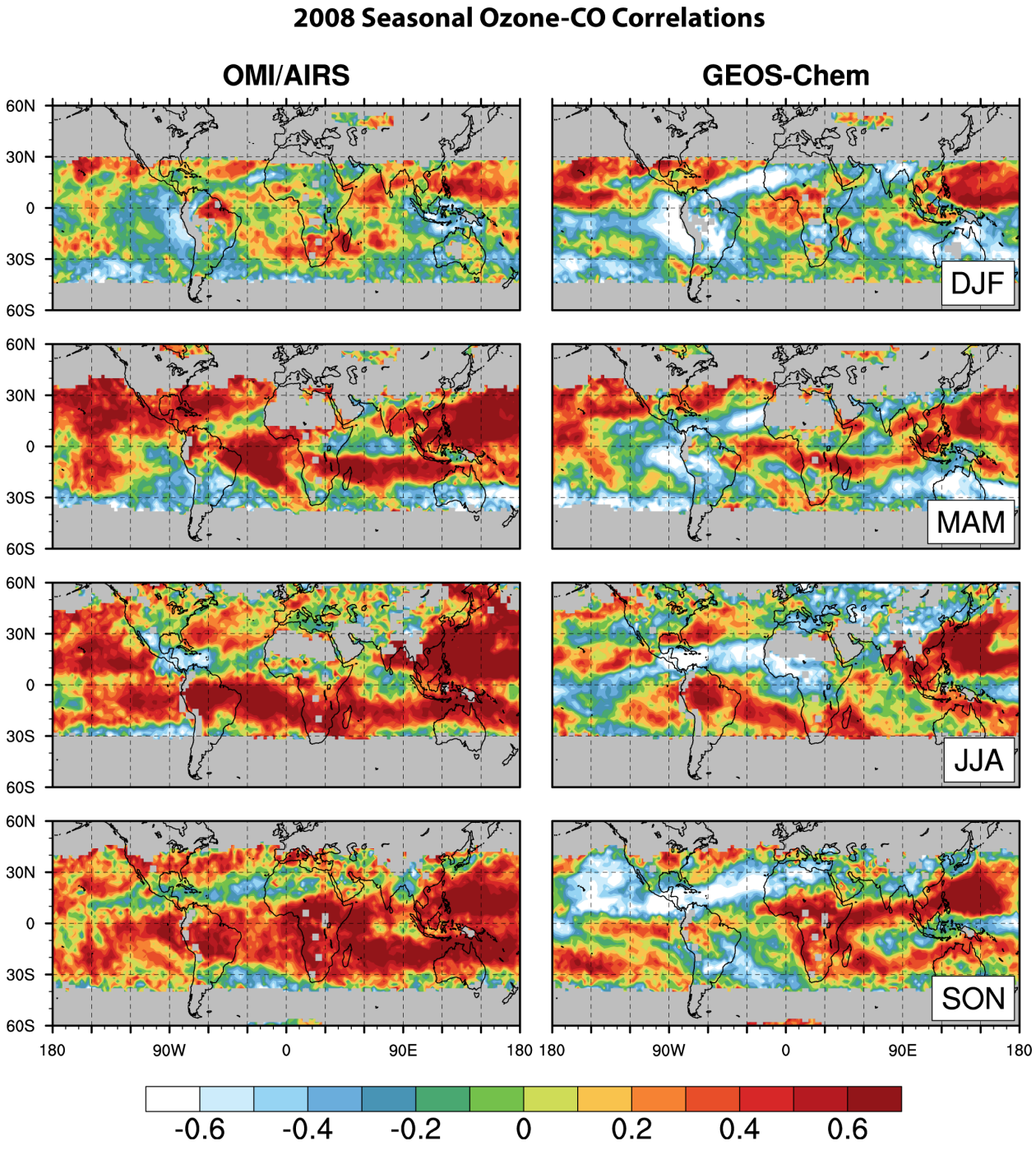

Figure 2.2: Ozone-CO correlation coefficients (r) for OMI/AIRS and GEOS-Chem for each season of 2008. The correlation coefficients are computed from daily data at 700-400 hPa on the $2^{o} \times 2.5^{o}$ GEOS-Chem grid. Gray indicates insufficient data.

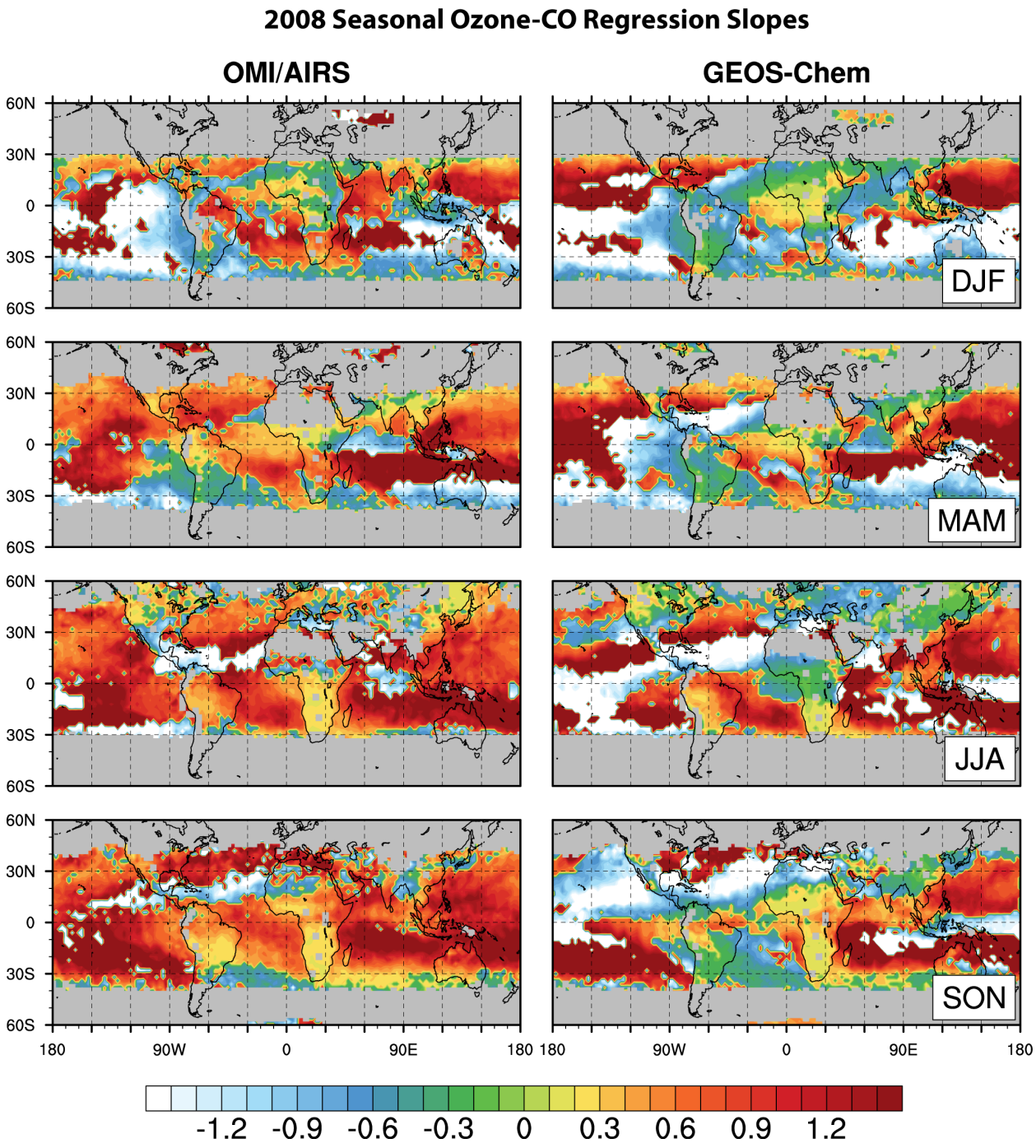

Figure 2.3: Same as **Figure 2.2** but for the ozone-CO reduced-major-axis regression slope ($dO_3/d\mathrm{CO}$).

tropical South Atlantic also features a negative correlation and this will be examined quantitatively in the next section.

The observed OMI/AIRS correlations reported here are generally consistent with previous TES results for July 2005 [*Zhang et al., 2006*], spring seasonal composites for the North Atlantic [*Hegarty et al., 2009*], and the four-year global July-August results [*Voulgarakis et al., 2011*]. The higher data density from OMI/AIRS provides finer-scale information. We find regional discrepancies with the *Voulgarakis et al.* [2011] TES analysis for December-January, for example in the sign of *r* over Indonesia. This may reflect interannual variability or actual inconsistency between the TES and OMI/AIRS product. We will address this issue in future work.

Figure 2.4 compares the OMI/AIRS RMA regression slopes (dO_3/dCO) to the corresponding MOZAIC aircraft values for each season of 2006 and 2008. Full statistics are listed in the **Appendix**. The MOZAIC slopes are positive and significant in all seasons, and this is consistent with the local OMI/AIRS slopes (no MOZAIC data are available where OMI/AIRS observes negative slopes). The *r* values from OMI/AIRS are in the same range as for MOZAIC. The slopes are strongly correlated with $r = 0.63$ although dO_3/dCO values from OMI/AIRS are 20% larger than from MOZAIC. The largest dO_3/dCO value in both cases is over Hyderabad in SON 2008, reflecting the contrast between polluted continental air and clean maritime tropical air. The smallest dO_3/dCO value in both cases (with strong correlation, see **Appendix**) is over Namibia in JJA 2008 and is typical of biomass burning plumes [*Mauzerall et al., 1998*].

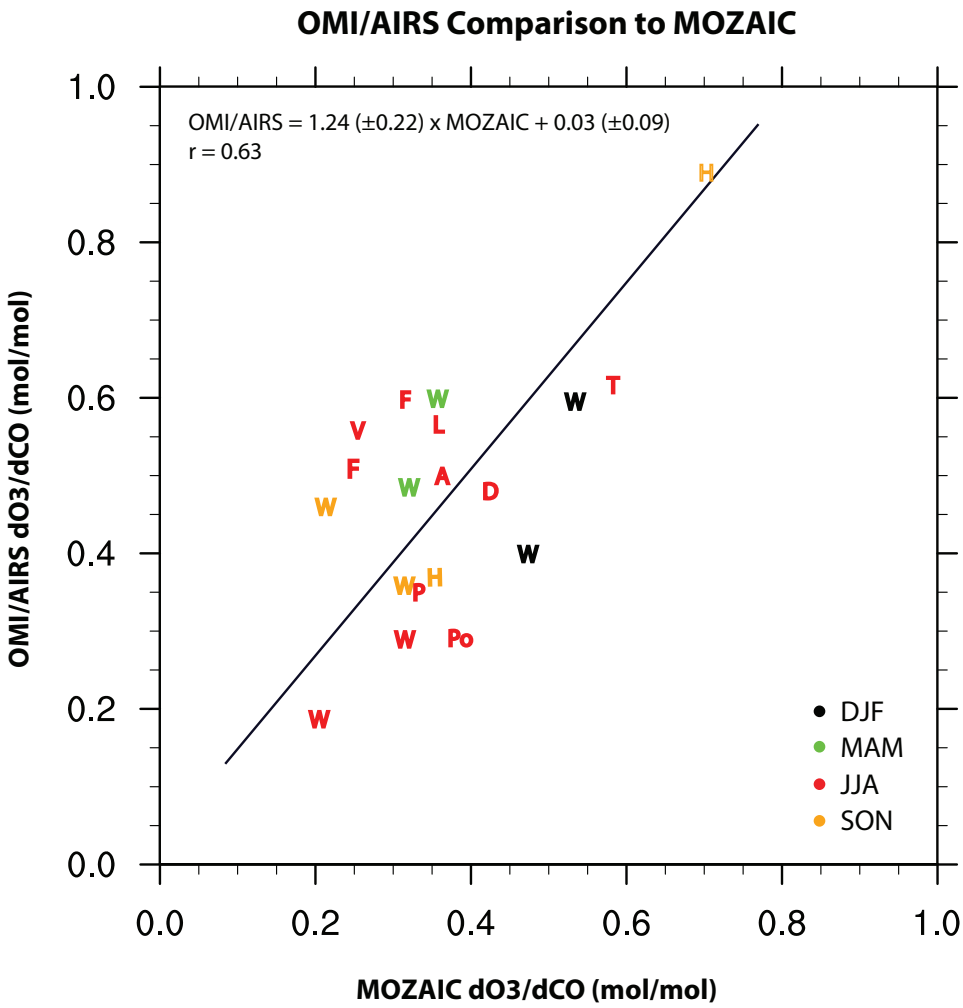

Figure 2.4: Comparison of ozone-CO reduced-major-axis (RMA) regression slopes (dO$_3$/dCO) at 700-400 hPa of the MOZAIC and OMI/AIRS observations. The RMA linear fit is shown inset with bootstrap errors. Values are shown for all MOZAIC vertical profile locations with n > 10 for individual seasons of 2006 and 2008. Complete comparison statistics are in the **Appendix**. The station locations are W: Windhoek, Namibia; Po: Portland, USA; D: Dallas, USA; A: Atlanta, USA; P: Philadelpha, USA; L: London, UK; F: Frankfurt, Germany; V: Vienna, Austria; T: Tokyo, Japan; and H: Hyderabad, India.

2.4 Interpretation of the Ozone-CO Relationship

Ozone-CO correlations reflect a combination of transport and chemistry. In pollution outflow mixing with a relatively clean background, the ozone-CO relationship gives a measure of the OPE for that pollution source region [*Parrish et al., 1993; Hirsch et al., 1996*]. In

stratospheric intrusions mixing with tropospheric air, the ozone-CO relationship reveals the stratospheric influence on ozone [*Fishman and Seiler, 1983*]. In general, however, the relative contributions of transport and chemistry in driving the ozone-CO relationship are not obvious, especially in the free troposphere where the chemistry is relatively slow and pollution enhancements are relatively weak. Previous studies for the free troposphere have highlighted how interpretation of ozone-CO correlations is complicated by mixing of combustion plumes with variable background [*Mauzerall et al., 1998*] or by interleaving of stratospheric intrusions with polluted continental outflow [*Parrish et al., 2000; Nowak et al., 2004; Price et al., 2004; Liang et al., 2007*]. These complications motivate the use of a CTM to interpret the observed ozone-CO relationships.

Two previous studies have used CTMs to interpret observed ozone-CO correlations from satellites. *Zhang et al.* [2008] found positive ozone-CO correlation coefficients in two transpacific pollution events in both the TES retrievals and GEOS-Chem. They interpreted the observed correlations as indicative of Asian pollution influence on ozone, since the correlation disappeared in the model in a sensitivity simulation without Asian emissions. *Voulgarakis et al.* [2011] conducted sensitivity simulations with perturbed emissions in the G-PUCCINI and UKCA models to examine the importance of different sources in driving the global correlation patterns. They found that emissions were important for changing the strength of the correlation downwind of source regions, with biomass burning in the tropics capable of changing the sign.

Here we use the GEOS-Chem CTM to interpret the OMI-AIRS ozone-CO correlations presented in **Figure 2.2**. Our aim is to use the observed correlations as constraints on the model representation of ozone sources. This can be compromised if the simulated correlations are highly sensitive to model transport error. In that case, comparison to observed correlations would

mainly serve as a convoluted test of model transport. Thus we first examine the sensitivity of the ozone-CO correlations in GEOS-Chem to model transport error, diagnose the features that appear to be robust against this transport error, and then conduct a more focused examination of the sensitivity to ozone sources for regions of particular interest.

2.4.1 Sensitivity to Model Transport Error

We examined the impact of model transport errors on the ozone-CO relationship simulated with GEOS-Chem by comparing the standard simulation driven by GEOS-5 meteorological data to a simulation driven by the previous-generation GEOS-4 meteorological data for the same year. Here we used 2006, the last year for which GEOS-4 data are available. GEOS-5 and GEOS-4 are very different in terms of both model physics (they use different general circulation models) and data assimilated. Previous studies have compared GEOS-5 and GEOS-4 simulations of CO [*Liu et al., 2010*] and CO_2 [*Feng et al., 2011; Parazoo et al., 2012*] and shown large differences reflecting the different convective parameterizations.

Figure 2.5 shows ozone-CO correlations in JJA 2006 from OMI/AIRS, GEOS-Chem driven by GEOS-4, and GEOS-Chem driven by GEOS-5. The OMI/AIRS JJA correlations for 2006 (El Niño) are similar to the 2008 (La Niña) results shown in **Figure 2.2**, with slight differences over the United States and Southeast Asia. We find that the ozone-CO correlations simulated by GEOS-Chem using GEOS-5 and GEOS-4 meteorological fields generally show similar spatial patterns. The main differences are in the tropics, where GEOS-4 tends to simulate weaker negative correlations than GEOS-5.

Overall, we conclude that model transport errors can have significant regional impacts on simulated ozone-CO correlations. In some areas such as the Equatorial West Pacific, this

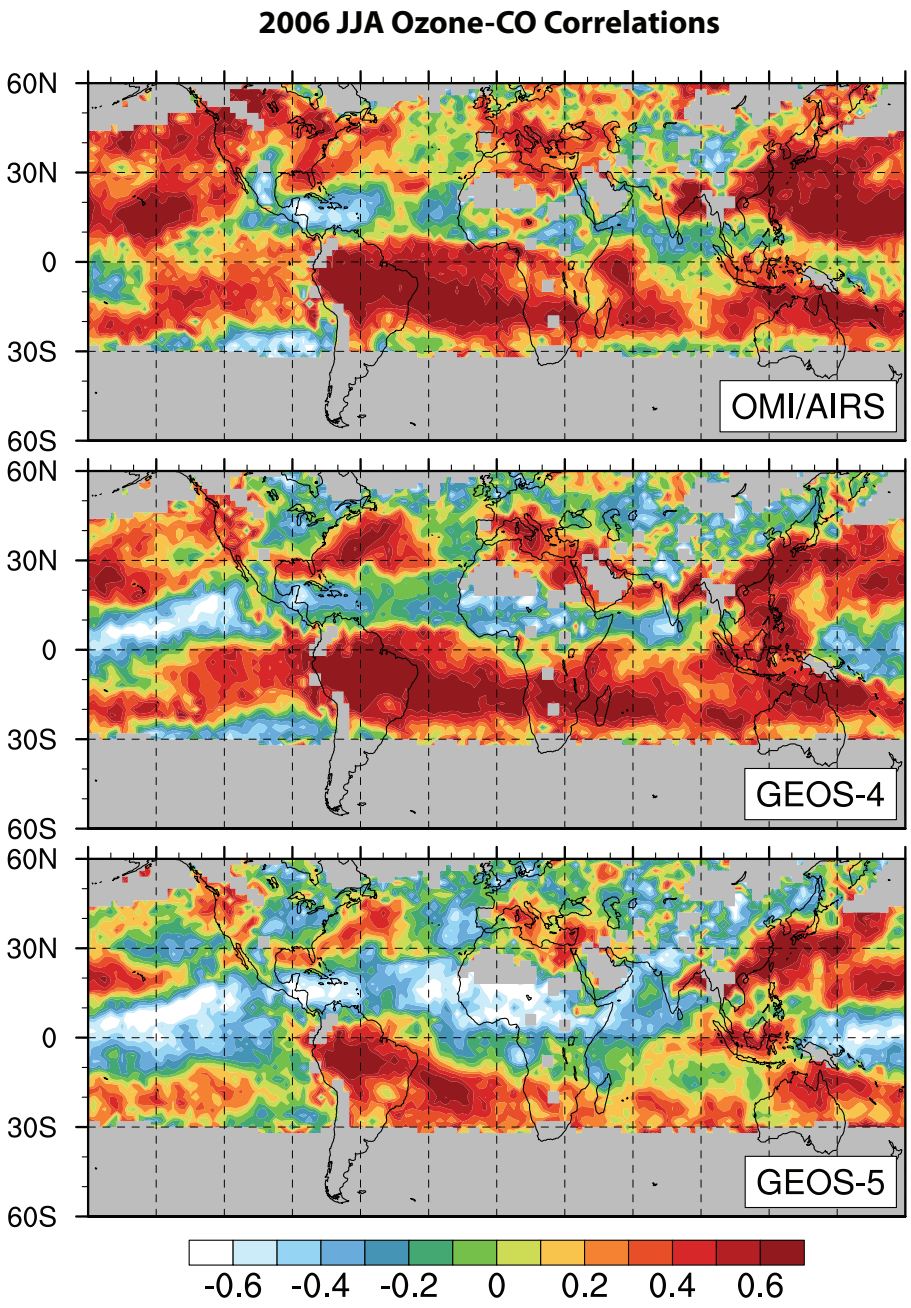

Figure 2.5: Ozone-CO correlation coefficients (r) at 700-400 hPa for JJA 2006 from OMI/AIRS and from GEOS-Chem driven by GEOS-4 and GEOS-5 meteorology. Gray indicates insufficient data (see text).

completely compromises the ability to interpret dO_3/dCO in terms of ozone sources. In most regions, however, the general correlation patterns are sufficiently robust against model transport errors (at least for GEOS-5 vs. GEOS-4) that we can investigate them further to diagnose

contributions from ozone sources.

2.4.2 Sensitivity to Ozone Sources

We now examine here whether the observed ozone-CO relationships can be used to place constraints on combustion (NO_x, CO, VOCs), biogenic (VOCs), lightning (NO_x), and stratospheric sources of ozone. All four are considered to be major sources of ozone, but their relative importance in different regions of the troposphere is uncertain [*Stevenson et al., 2006; Wu et al., 2007; Terao et al., 2008; Baray et al., 2012*]. Starting from the standard GEOS-Chem simulation described in Section 2.2 and with results shown in **Figures 2.2** and **2.3** and in the **Appendix**, our approach is to conduct sensitivity simulations with individual sources shut off. Here we aggregate fossil fuels and biomass burning in the combustion source, with the understanding that the latter will mainly affect the tropics.

Zhang et al. [2006] and *Voulgarakis et al.* [2011] previously diagnosed the influence of individual sources on the ozone-CO relationship as the change in the ozone-CO correlation or slope (dO_3/dCO) between their standard CTM simulation and a sensitivity simulation with that source shut off. However, this does not provide a proper measure of the influence of the source on ozone because the ozone-CO relationship is then affected by changes in both ozone and CO. A more appropriate approach is to correlate CO from the standard simulation with the ozone difference between the standard and sensitivity simulations. *Chin et al.* [1994] previously used this approach to interpret ozone-CO relationships from eastern North American surface sites in terms of ozone production.

We illustrate our approach in **Figure 2.6**, which shows the simulated ozone-CO relationships at 700-400 hPa for a $2^o \times 2.5^o$ grid square in JJA in the western North Atlantic (38°

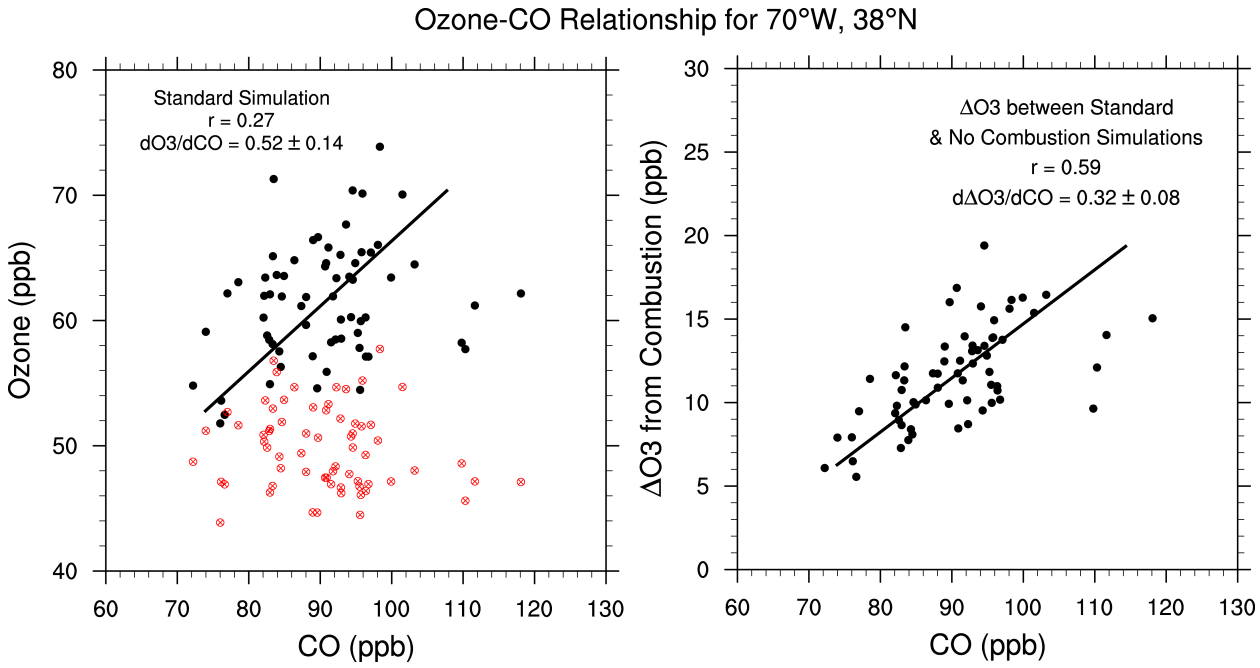

Figure 2.6: Ozone-CO relationships at 700-400 hPa in JJA 2008 over the western North Atlantic ($2^o \times 2.5^o$ grid square centered at 38° N, 70° W). Values are GEOS-Chem model results sampled daily at the local OMI and AIRS satellite overpass times and weighted by the vertical sensitivity of the instruments. In the left panel, ozone concentrations in black are from the standard simulation and in red for the sensitivity simulation including no combustion sources. CO concentrations are from the standard simulation in both cases. The right panel shows the ozone difference ΔO_3 between the standard and sensitivity simulations as a function of CO from the standard simulation, with slope $d\Delta O_3/dCO$. All regression lines are obtained by the reduced-major-axis (RMA) method and the slope bound is the 95% confidence interval calculated from nonparametric bootstrapping.

N, 70° W) receiving polluted continental outflow from North America (*Zhang et al.* [2006] had previously examined the ozone-CO relationships observed from TES and aircraft for the same region). In the left panel of **Figure 2.6**, ozone from the standard simulation is shown in black and ozone from a simulation without combustion sources is shown in red, both plotted against CO from the standard simulation. The ozone-CO slope and 95% confidence interval calculated using nonparametric bootstrapping for the standard simulation are shown inset. We see that the ozone-CO correlation disappears without combustion sources, indicating that it provides a test of combustion influence. This is quantified in the right panel by plotting the ozone difference ΔO_3

between the standard and no combustion simulations against CO from the standard simulation. We find a strong positive slope $d\Delta O_3/dCO$ that can explain the majority of dO_3/dCO from the standard simulation.

Global maps of $d\Delta O_3/dCO$ for different ozone sources and seasons are presented in the **Appendix** and can be used to interpret the dO_3/dCO slopes in **Figure 2.3**. Here we focus our discussion on three illustrative regions of particular interest: (1) the North Atlantic in JJA (30° - 40° N, 60° - 80° W), where US pollution outflow is known to take place and has been previously diagnosed from observed ozone-CO correlations; (2) the South Atlantic in DJF (0° - 20° S, 30° W - 10° E), where different explanations have been proposed for the origin of the observed ozone maximum; and (3) the Northeast Pacific in SON (20° - 40° N, 120° - 160° W), where significant intercontinental transport of Asian pollution is expected. As shown in **Figure 2.3**, GEOS-Chem reproduces the observed dO_3/dCO from OMI/AIRS for (1) and (2) but fails for (3).

Figure 2.7 shows the observed and simulated dO_3/dCO for the three above regions along with $d\Delta O_3/dCO$ calculated for simulations without combustion, biogenic, lightning NO_x, and stratospheric ozone sources for 2008. The statistics are calculated by aggregating all of the daily average ozone and CO data contained within the region boundaries. We also include in **Figure 2.7** the observed dO_3/dCO for 2006, along with model values for that year using both GEOS-5 and GEOS-4 meteorology. These allow us to examine interannual variability and the effect of transport errors as discussed above. Error bounds in **Figure 2.7** represent the standard deviation calculated from all nonparametric bootstrap slope realizations for each grid within the region boundaries.

Figure 2.7: Regional bar plots of ozone-CO statistics for a) the western North Atlantic *(30° - 40° N, 60° - 80° W)* in JJA; b) the South Atlantic *(0° - 20° S, 30° W - 10° E)* in DJF; and c) the East Pacific *(20° - 40° N, 120° - 160° W)* in SON. From left to right, the bars show $d\mathrm{O_3}/d\mathrm{CO}$ for OMI/AIRS, GEOS-Chem driven by GEOS-4, and GEOS-Chem driven by GEOS-5 in 2006; $d\mathrm{O_3}/d\mathrm{CO}$ for OMI/AIRS and GEOS-Chem driven by GEOS-5 in 2008; and $d\Delta\mathrm{O_3}/d\mathrm{CO}$ for simulations without combustion sources, biogenic sources, stratospheric influence, and lightning $\mathrm{NO_x}$ emissions for 2008. See text for explanation of error bounds.

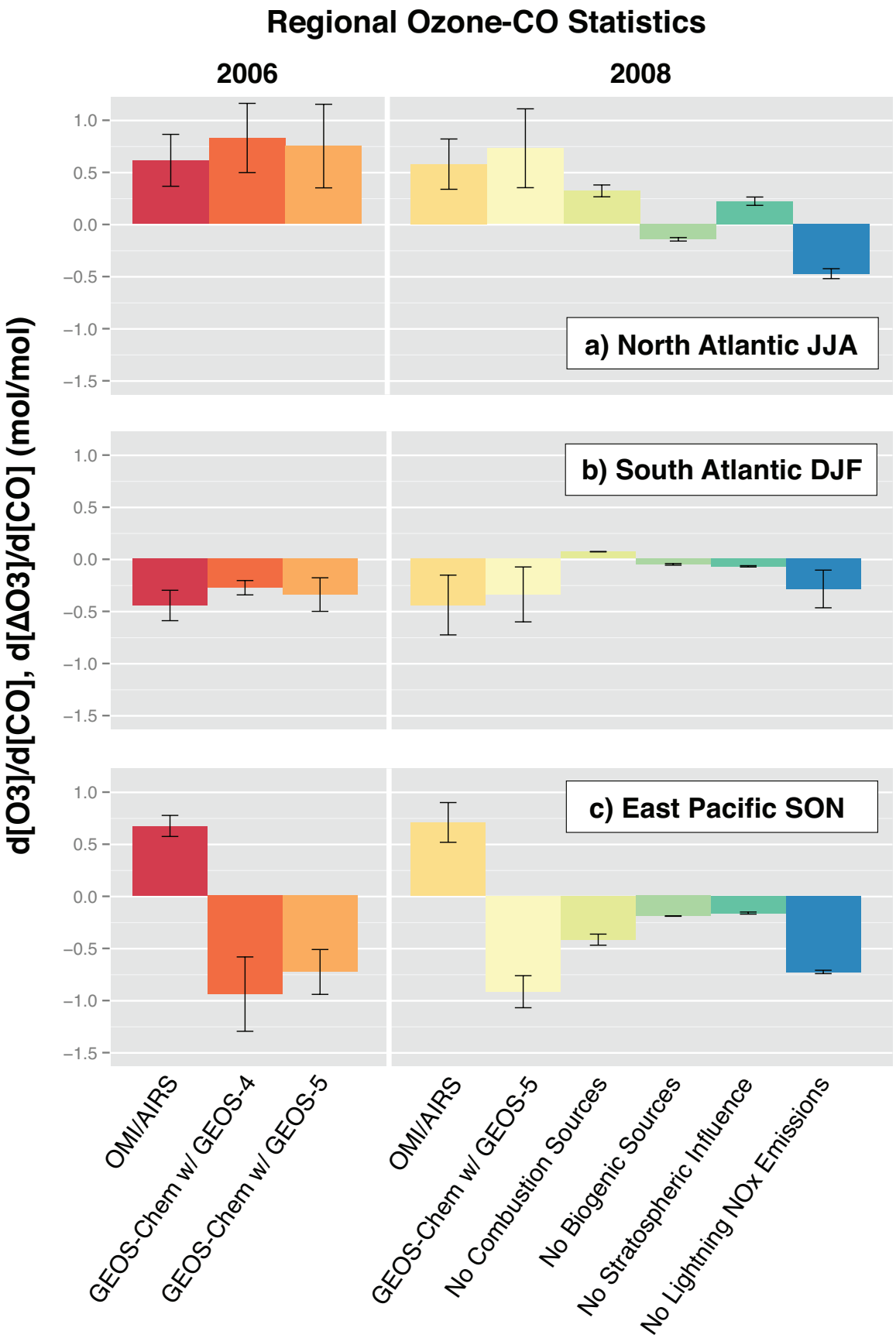
Regional Ozone-CO Statistics
2006
2008
d[O3]/d[CO], d[ΔO3]/d[CO] (mol/mol)
1.0
0.5
0.0
−0.5
−1.0
−1.5
a) North Atlantic JJA
b) South Atlantic DJF
c) East Pacific SON
OMI/AIRS
GEOS-Chem w/ GEOS-4
GEOS-Chem w/ GEOS-5
OMI/AIRS
GEOS-Chem w/ GEOS-5
No Combustion Sources
No Biogenic Sources
No Stratospheric Influence
No Lightning NOx Emissions

2.4.2.1 North Atlantic in JJA

The observed ozone-CO relationship at northern mid-latitudes in JJA shows a consistent positive correlation in continental outflow. Here we focus on the North Atlantic (top panel of **Figure 2.7**) but results are similar for the NW Pacific. The GEOS-Chem $d\mathrm{O_3}/d\mathrm{CO}$ agrees well with the observed slope of 0.72 ± 0.30 for 2008. The observed slopes show little difference between 2006 (0.76 ± 0.31) and 2008. The GEOS-Chem results using GEOS-5 and GEOS-4 in 2006 are consistent, suggesting that the ozone-CO relationship is robust against errors in transport.

From the $d\Delta\mathrm{O_3}/d\mathrm{CO}$ values in **Figure 2.7** we see that the $\mathrm{O_3}$-CO correlation over the North Atlantic in JJA reflects a major contribution from combustion sources. Surface observations over the eastern US in summer typically show a $d\mathrm{O_3}/d\mathrm{CO}$ value of 0.3–0.5, with higher values in more recent studies reflecting a decrease in CO emissions [*Chin et al., 1994; Hirsch et al., 1996; Mao and Talbot, 2004; Hudman et al., 2008, 2009*]. We find in our sensitivity simulation that $d\Delta\mathrm{O_3}/d\mathrm{CO}$ from combustion sources decreases from west to east across the North Atlantic while $d\mathrm{O_3}/d\mathrm{CO}$ remains roughly constant, suggesting little sustained photochemical production following lifting of the surface air to the free troposphere. The observed and simulated $d\mathrm{O_3}/d\mathrm{CO}$ fall within the range of slopes observed by *Honrath et al*. [2004] at a mountaintop site in the Azores for 2001 and 2003.

Air mixing down from the stratosphere makes a significant contribution to the ozone-CO regression slope, as shown in **Figure 2.7**. A remarkable result is that this effect is positive, whereas stratospheric influence is commonly thought to be associated with a negative ozone-CO correlation [*Fishman and Seiler, 1983*]. As shown by *Cooper et al.* [2002], stratospheric influence over the western North Atlantic is associated with the dry air stream (DA) of mid-

latitudes cyclones, mixing with the warm conveyor belt (WCB) that lifts continental pollution to the free troposphere. This would lead to positive correlation of pollution and stratospheric influences when smoothed vertically over the averaging kernel of the satellite observations. A number of studies have shown ozone pollution plumes over the northern mid-latitude oceans to be interweaved with stratospheric influence [*Parrish et al. 2000; Nowak et al., 2004; Price et al., 2004; Liang et al., 2007*].

Lightning NO_x has a large negative influence on dO_3/dCO over the North Atlantic, comparable in magnitude to the positive influence from combustion sources (top panel of **Figure 2.7**). Lightning NO_x produces both ozone and OH with high efficiency [*Labrador et al., 2004*], and OH oxidizes CO, thus leading in general to a negative $d\Delta O_3/dCO$ effect.

2.4.2.2 South Atlantic in DJF

Tropical tropospheric ozone shows a persistent maximum over the South Atlantic associated with strong subsidence [*Thompson et al., 2000; Sauvage et al., 2006*]. The DJF ozone maximum is clearly seen by OMI (bottom panel of **Figure 2.1**) and is well reproduced by GEOS-Chem (see **Appendix**). The sources contributing to this maximum are not well understood. Different studies have argued for major contributions from combustion sources, including biomass burning in Africa [*Thompson et al., 1996; Jourdain et al., 2007*] and long-range transport of pollution [*Chatfield et al., 2004*], lightning NO_x [*Martin et al., 2002; Sauvage et al. 2007*], and intrusions of Northern Hemispheric air [*Waugh and Polvani, 2000; Martin et al., 2002*].

We see from the middle panel of **Figure 2.7** that the observed regression slope for the region is negative with a value of -0.49 ± .31. Good consistency is found between GEOS-Chem

(either GEOS-5 or GEOS-4) and observations, and between 2006 and 2008. Model sensitivity studies indicate that the ozone-CO relationship is determined principally by lightning NO_x emissions. This implies that the ozone variability in the region is driven by lightning as suggested previously by *Sauvage et al.* [2007]. The negative ozone-CO correlation associated with the lightning NO_x source reflects ozone production in the upper troposphere followed by strong subsidence of this photochemically aged air over the South Atlantic [*Jacob et al., 1996; Martin et al., 2002*]. The $d\Delta O_3/dCO$ values in **Figure 2.7** suggest that stratospheric and combustion sources, including biomass burning, make little contribution to the ozone maximum over the South Atlantic.

2.4.2.3 North Pacific in SON

The dO_3/dCO values derived from OMI and AIRS are positive in all seasons over the northeastern Pacific poleward of 20^o N (**Figure 2.3**). GEOS-Chem reproduces this in DJF and MAM, but has negative slopes in JJA that extend across the entire eastern North Pacific by SON. The SON discrepancy is summarized in the bottom panel of **Figure 2.7**. A slope of 0.76 ± 0.20 is observed in 2008 (similar in 2006), but GEOS-Chem simulates a negative slope using either GEOS-5 or GEOS-4 meteorology. The consistency between GEOS-5 and GEOS-4 suggests that an error in sources is responsible for the poor simulation.

The model shows negative $d\Delta O_3/dCO$ over the region from all ozone sources including combustion (bottom panel of **Figure 2.7**). This is because air masses over the Northeast Pacific are very remote from sources, having been transported across the Pacific and subsiding slowly around the Pacific High. Ozone is produced efficiently in the subsiding air masses [*Hudman et al., 2004; Zhang et al., 2008*] while CO is oxidized. **Figure 2.7** shows that lightning is the

principal driver of the negative dO_3/dCO values in GEOS-Chem.

Even in the absence of lightning influence, however, we see from **Figure 2.7** that GEOS-Chem would still produce negative dO_3/dCO values over the Northeast Pacific. This may reflect a model underestimate of CO emissions from East Asia, as supported by the underestimate of AIRS CO mixing ratios (compare the top panel of **Figure 2.1** with the model output in the **Appendix**) and by the work of *Kopacz et al.* [2010] who found from an inverse analysis using AIRS CO data that GEOS-Chem underestimates CO sources in China by up to a factor of two in SON. Such a bias in CO emissions could cause the $d\Delta O_3/dCO$ values from Asian pollution over the Northeast Pacific to flip from positive to negative.

2.5 Summary

Ozone-CO correlations provide a valuable constraint to test models of tropospheric ozone but have hitherto been limited to in-situ measurements and sparse satellite observations. By using satellite instruments with near-daily global coverage of the same scenes, OMI for ozone and AIRS for CO, we constructed a global data set of ozone-CO correlations in the free troposphere on a $2^o \times 2.5^o$ grid with seasonal resolution and for individual years. The high data density avoids the degradation of the correlations by instrument noise that was a problem in previous satellite studies. The correlation coefficients r are highly significant, showing strong positive values in continental outflow in the northern extratropics. The tropics and southern hemisphere show seasonally varying patterns of positive and negative correlations. Evaluation with MOZAIC aircraft vertical profiles shows good consistency in correlation and regression slope patterns.

We interpreted the satellite-derived ozone-CO correlations with the GEOS-Chem

chemical transport model to explore the constraints that they place on the model sources of ozone. By driving the model with different meteorological fields for the same year, we diagnosed the effect of model transport error on the correlations. This effect is large in some regions of the tropics, where the ozone-CO correlations are then of little value as a test of ozone sources. In general, however, we find that correlation patterns are consistent for different meteorological fields as well as different years, and can therefore be used as a test of ozone sources.

We tested the model sensitivity of the ozone-CO regression slope, $d\mathrm{O_3}/d\mathrm{CO}$, to different sources by conducting a series of sensitivity simulations with individual sources shut off (combustion, biosphere, stratosphere, lightning $\mathrm{NO_x}$). From these we calculated the source influence, $d\Delta\mathrm{O_3}/d\mathrm{CO}$, by correlating the ozone change from each source with CO from the standard simulation. The results provide global information on the sources responsible for the ozone-CO correlations in the model, thus enabling interpretation of comparisons of simulated and observed $d\mathrm{O_3}/d\mathrm{CO}$. Complete results are in the **Appendix**. We focused our discussion on three regions of particular interest.

The northern extratropics show strong positive $d\mathrm{O_3}/d\mathrm{CO}$ in spring-summer that is driven by combustion sources and provides a test of the model simulation of continental outflow and intercontinental transport of ozone pollution. Remarkably, we find that stratospheric influence in the region is also associated with a positive $d\Delta\mathrm{O_3}/d\mathrm{CO}$ value, reflecting its interweaving with continental outflow.

The well-known tropical ozone maximum over the South Atlantic features a strongly negative $d\mathrm{O_3}/d\mathrm{CO}$, consistent for different years and meteorological data sets. GEOS-Chem reproduces this observation and attributes it to lightning. Previous model studies had reached a range of conclusions as to the origin of the South Atlantic ozone maximum, but the independent

information from the ozone-CO correlations provides evidence of a dominant lightning source.

The Northeast Pacific is a region of particular interest for transpacific ozone pollution. Here we find that GEOS-Chem fails to reproduce the observed ozone-CO correlation in summer-fall, yielding negative dO_3/dCO values when the observations show positive values. Remarkably, all ozone sources in the model yield negative $d\Delta O_3/dCO$ values in that region. This reflects the remote subsiding environment, where ozone is produced while CO is oxidized as air masses subside slowly around the Pacific High. Further analysis combined with independent evidence suggests that correcting this model bias would require both a reduction in the lightning source at northern mid-latitudes and an increase in CO emissions in East Asia.

We have shown in this paper that the combination of OMI ozone and AIRS CO provides a robust global data set of ozone-CO correlations in the free troposphere, and that these correlations provide a powerful tool for testing ozone sources in global models. In future work we will exploit this data set further to examine interannual variability in ozone-CO correlations and the implications for our understanding of ozone sources.

Acknowledgements

This work was funded by the NASA Aura Program and in part by the Department of Energy Office of Science Graduate Fellowship Program (DOE SCGF), made possible in part by the American Recovery and Reinvestment Act of 2009, administered by ORISE-ORAU under contract no. DE-AC05-06OR23100. The authors acknowledge the support of the MOZAIC program by the European Commission, EADS, Airbus, and the airlines (Lufthansa, Austrian, Air France, and Air Namibia) who carry the MOZAIC equipment free of charge and who have performed the maintenance since 1994. The MOZAIC database is supported by ETHER (CNES and INSU-CNRS).

References

Andreae, M. O., B. E. Anderson, D. R. Blake, J. D. Bradshaw, J. E. Collins, G. L. Gregory, G. W. Sachse, and M. C. Shipham (1994), Influence of plumes from biomass burning on atmospheric chemistry over the equatorial and tropical South Atlantic during CITE 3, *J. Geophys. Res., 99*(D6), 12793-12808, doi:10.1029/94JD00263.

Aumann, H. H., et al. (2003), AIRS/AMSU/HSB on the Aqua Mission: Design, Science Objectives, Data Products, and Processing Systems, *IEEE T. Geosci. Remote, 41*, 253–264, doi:10.1109/TGRS.2002.808356.

Baray, J.-L., V. Duflot, F. Posny, J.-P. Cammas, A. M. Thompson, F. Gabarrot, J.-L. Bonne, and G. Zeng (2012), One year ozonesonde measurements at Kerguelen Island (49.2^{o} S, 70.1^{o} E): Influence of stratosphere-to-troposphere exchange and long-range transport of biomass burning plumes, *J. Geophys. Res., 117*, D06305, doi:10.1029/2011JD016717.

Beer, R., T. A. Glavich, and D. M. Rider (2001), Tropospheric emission spectrometer for the Earth Observing System's Aura satellites, *Appl. Opt., 40*, 2356-2367, doi:10.1364/AO.40.002356.

Bey, I., D. J. Jacob, R. M. Yantosca, J. A. Logan, B. Field, A. M. Fiore, Q. Li, H. Liu, L. J. Mickley, and M. Schultz (2001), Global modeling of tropospheric chemistry with assimilated meteorology: Model description and evaluation, *J. Geophys. Res., 106*(D19), 23073-23096, doi:10.1029/2001JD000807.

Braak, R. (2010), Bug fix for GDPS measurement noise calculation algorithm, KNMI, Technical Note TN-OMIE-KNMI-935.

Cardenas, L. M., J. F. Austin, R. A. Burgess, K. C. Clemitshaw, S. Dorling, S. A. Penkett, and R. M. Harrison (1998), Correlations between CO, NOy, O3, and non-methane hydrocarbons and their relationships with meteorology during winter 1993 on the north Norfolk coast, U.K., *Atmos. Environ., 32,* 3339-3351, doi:10.1016/S1352-2310(97)00445-7.

Chatfield, R. B., H. Guan, A. M. Thompson, and J. C. Witte (2004), Convective lofting links Indian Ocean air pollution to paradoxical South Atlantic ozone maxima, *Geophys. Res. Lett., 31,* L06103, doi:10.1029/2003GL018866.

Chin, M., D. J. Jacob, J. W. Munger, D. D. Parrish, and B. G. Doddridge (1994), Relationship of ozone and carbon monoxide over North America and its implication for ozone production and transport, *J. Geophys. Res., 99*(D7), 14565-14573, doi:10.1029/94JD00907.

Cooper, O. R., J. L. Moody, D. D. Parrish, M. Trainer, T. B. Ryerson, J. S. Holloway, G. Hubler, F. C. Fehsenfeld, and M. J. Evans (2002), Trace gas composition of midlatitude cyclones over the western North Atlantic Ocean: A conceptual model, *J. Geophys. Res., 107,* D04056, doi:10.1029/2001JD000901.

Deeter, M. N., et al. (2003), Operational carbon monoxide retrieval algorithm and selected

results for the MOPITT instrument, *J. Geophys. Res., 108*(D14), 4399, doi:10.1029/2002JD003186.

Feng, L., P. I. Palmer, Y. Yang, R. M. Yantosca, S. R. Kawa, J.-D. Paris, H. Matsueda, and T. Machida (2011), Evaluating a 3-D transport model of atmospheric CO_2 using ground-based, aircraft, and space-borne data, *Atmos. Chem. Phys., 11*, 2789-2803, doi:10.5194/acp-11-2789-2011.

Fiore, A. M., et al. (2009), Multimodel estimates of intercontinental source receptor relationships for ozone pollution, *J. Geophys. Res., 114*, D04301, doi:10.1029/2008JD010816.

Fishman, J., and W. Seiler (1983), Correlative nature of ozone and carbon monoxide in the troposphere: implications for the tropospheric ozone budget, *J. Geophys. Res., 88*, 3662–3670, doi:10.1029/JC088iC06p03662.

Giglio, L., J. T. Randerson, G. R. van der Werf, P. S. Kasibhatla, G. J. Collatz, D. C. Morton, and R. S. DeFries (2010), Assessing variability and long-term trends in burned area by merging multiple satellite fire products, *Biogeosciences, 7*, 1171-1186, doi:10.5194/bg-7-1171-2010.

Guenther, A., T. Karl, P. Harley, C. Wiedinmyer, P. I. Palmer, and C. Geron (2006), Estimates of global terrestrial isoprene emissions using MEGAN (Model of Emissions of Gases and Aerosols from Nature), *Atmos. Chem. Phys, 6*, 3181- 3210, doi:10.5194/acp-6-3181-2006.

Harris, J. M., E. J. Dlugokencky, S. J. Oltmans, P. P. Tans, T. J. Conway, P. C. Novelli, K. W. Thoning, and J. D. W. Kahl (2000), An interpretation of trace gas correlations during Barrow, Alaska, winter dark periods, 1986-1997, *J. Geophys. Res., 105*(D13), 17267-17278, doi:10.1029/2000JD900167.

Hegarty J. D., H. Mao, and R. Talbot (2009), Synoptic influences on springtime tropospheric O3 and CO over the North American export region observed by TES, *Atmos. Chem. Phys., 9*, 3755–3776, doi:10.5194/acp-9-3755-2009.

Hegarty J. D., H. Mao, and R. Talbot (2010), Winter- and summertime continental influences on tropospheric O3 and CO observed by TES over the western North Atlantic Ocean, *Atmos. Chem. Phys., 10*, 3723-3741, doi:10.5194/acp-10-3723-2010.

Hirsch, A. I., J. W. Munger, D. J. Jacob, L. W. Horowitz, and A. H. Goldstein (1996), Seasonal variation of the ozone production efficiency per unit NOx at Harvard Forest, Massachusetts, *J. Geophys. Res., 101*(D7), 12659-12666, doi:10.1029/96JD00557.

Honrath, R. E., R. C. Owen, M. Val Martin, J. S. Reid, K. Lapina, P. Fialho, M. P. Dziobak, J. Kleissl, and D. L. Westphal (20040, Regional and hemispheric impacts of anthropogenic and biomass burning emissions on summertime CO and O3 in the North Atlantic lower free troposphere, *J. Geophys. Res., 109,* D24310, doi:10.1029/2004JD005147.

Hudman, R. C., et al. (2004), Ozone production in transpacific Asian pollution plumes and implications for ozone air quality in California, J. Geophys. Res., 109, D23S10, doi:10.1029/2004JD004974.

Hudman, R. C., et al. (2007), Surface and lightning sources of nitrogen oxides over the United States: magnitudes, chemical evolution, and outflow, *J. Geophys. Res., 112*, D12S05, doi:10.1029/2006JD007912.

Hudman, R. C., L. T. Murray, D. J. Jacob, D. B. Millet, S. Turquety, S. Wu, D. R. Blake, A. H. Goldstein, J. Holloway, and G. W. Sachse (2008), Biogenic versus anthropogenic sources of CO in the United States, *Geophys. Res. Lett., 35*, L04801, doi:10.1029/2007GL032392.

Hudman, R. C., L T. Murray, D. J. Jacob, S. Turquety, S. Wu, D. B. Millet, M. Avery, A. H. Goldstein, and J. Holloway (2009), North American influence on tropospheric ozone and the effects of recent emission reductions: Constraints from ICARTT observations, *J. Geophys. Res., 114*, D07302, doi:10.1029/2008JD010126.

IPCC (2007), Climate Change 2007: The Physical Scientific Basis, Contribution of Working Group I to the Fourth Assessment Report of the Intergovernmental Panel on Climate Change, edited by: Solomon, S., et al., Cambridge University Press, Cambridge, United Kingdom and New York, NY, USA.

Jacob, D. J., et al. (1996), Origin of ozone and NO_x in the tropical troposphere: A photochemical analysis of aircraft observations over the South Atlantic basin, *J. Geophys. Res., 101*(D19), 24235-24250, doi:10.1029/96JD00336.

Jaffe, D. A., and N. L. Wigder (2012), Ozone production from wildfires: A critical review, *Atmos. Environ., 51*, 1-10, doi:10.1016/j.atmosenv.2011.11.062.

Jourdain, L., et al. (2007), Tropospheric vertical distribution of tropical Atlantic ozone observed by TES during the north African biomass burning season, *Geophys. Res. Lett., 34,* L04810, doi:10.1029/2006GL028284.

Kopacz, M. A., et al. (2010), Global estimates of CO sources with high resolution by adjoint inversion of multiple satellite datasets (MOPITT, AIRS, SCIAMACHY, TES), *Atmos. Chem. Phys., 10,* 855-876, doi:10.5194/acp-10-855-2010.

Kuhns, H., M. Green, and V. Etyemezian (2003), Big Bend Regional Aerosol and Visibility Observational (BRAVO) Study Emissions Inventory, Report prepared for BRAVO Steering Committee, Desert Research Institute, Las Vegas, Nevada.

Labrador, L. J., R. von Kuhlmann, and M. G. Lawrence (2004), Strong sensitivity of the global mean OH concentration and the tropospheric oxidizing efficiency to the source of NO_x from lightning, *Geophys. Res. Lett., 31,* L06102, doi:10.1029/2003GL019229.

Lee, C., R. V. Martin, A. van Donkelaar, H. Lee, R. R. Dickerson, J. C. Hains, N. Krotkov, A.

Richter, K. Vinnikov, and J. J Schwab (2010), SO_2 emissions and lifetimes: Estimates from inverse modeling using in situ and global, space-based (SCIAMACHY and OMI) observations, *J. Geophys. Res., 116*, D06304, doi:10.1029/2010JD014758.

Levelt, P. F., G. H. J. van den Oord, M. R., Dobber, A. Malkki, H. Visser, J. de Vries, P. Stammes, J. O. V. Lundell, and H. Saari (2006), The Ozone Monitoring Instrument, *IEEE T. Geosci. Remote*, *44*, 1093–1101, doi:10.1109/TGRS.2006.872333.

Liang, Q., et al. (2007), Summertime influence of Asian pollution in the free troposphere over North America, *J. Geophys. Res., 112*, D12S11, doi:10.1029/2006JD007919.

Liu, J., J. A. Logan, D. B. A. Jones, N. J. Livesey, I. Megretskaia, C. Carouge, and P. Nedelec (2010), Analysis of CO in the tropical troposphere using Aura satellite data and the GEOS-Chem model: insight into transport characteristics of the GEOS meteorological products, *Atmos. Chem. Phys., 10*, 12207-12232, doi:10.5194/acp-10-12207-2010.

Liu, X., P. K. Bhartia, K. Chance, R. J. D. Spurr, and T. P. Kurosu (2010), Ozone profile retrievals from the Ozone Monitoring Instrument, *Atmos. Chem. Phys., 10*, 2521-2537, doi:10.5194/acp-10-2521-2010.

Mao, H., and R. Talbot (2004), O3 and CO relationships in New England: temporal variations and relationships, *J. Geophys. Res., 109,* D21304, doi:10.1029/2004JD004913.

Mao, J., S. Fan, D. J. Jacob, and K. R. Travis (2013), Radical loss in the atmosphere from Cu-Fe redox coupling in aerosols, *Atmos. Chem. Phys., 13*, 509-519, doi:10.5194/acp-13-509-2013.

Marenco, A., et al. (1998), Measurement of ozone and water vapor by Airbus in-service aircraft: the MOZAIC airborne program, an overview, *J. Geophys. Res., 103*, 631-642, doi:10.1029/98JD00977.

Martin, R. V., et al. (2002), Interpretation of TOMS observations of tropical tropospheric ozone with a global model and in situ observations, *J. Geophys. Res., 107*(D18), 4351, doi:10.1029/2001JD001480.

Martin, R. V., B. Sauvage, I. Folkins, C. E. Sioris, C. Boone, P. Bernath, and J. Ziemke (2007), Space-based constraints on the production of nitric oxide by lightning, *J. Geophys. Res., 112,* D09309, doi:10.1029/2006JD007831, 2007.

Mauzerall, D. L., J. A. Logan, D. J. Jacob, B. E. Anderson, D. R. Blake, J. D. Bradshaw, B. Heikes, G. W. Sachse, H. B. Singh, and R. W. Talbot (1998), Photochemistry in biomass burning plumes and implications for tropospheric ozone over the tropical south Atlantic, *J. Geophys. Res., 103*(D7), 8401-8424, doi:10.1029/97JD02612.

McLinden, C. A., S. C. Olsen, B. Hannegan, O. Wild, M. J. Prather, and J. Sundet (200), Stratospheric ozone in 3-D models: A simple chemistry and cross-tropopause flux, *J. Geophys. Res., 105*(D11), 14653-14666, doi:10.1029/2000JD900124.

McMillan, W. W., K. D. Evans, C. D. Barnet, E. Maddy, G. W. Sachse, and G. S. Disken (2011), Validating the AIRS Version 5 CO retrieval with DACOM in situ measurements during INTEX-A and –B, *IEEE T. Geosci. Remote, 49*(7), 2802-2813, doi:10.1109/TGRS.2011.2106505.

McPeters, R. D., G. J. Labow, and J. A. Logan (2007), Ozone climatological profiles for satellite retrieval algorithms, *J. Geophys. Res., 112*, D05308, doi:10.1029/2005JD006823.

Monks, P. S (2000), A review of the observations and origins of the spring ozone maximum, *Atmos. Environ., 34*, 3545-3561, doi:10.1016/S1352-2310(00)00129-1.

Murray, L. T., D. J. Jacob, J. A. Logan, R. C. Hudman, and W. J. Koshak (2012), Optimized regional and interannual variability of lightning in a global chemical transport constrained by LIS/OTD satellite data, *J. Geophys. Res., 117*, D20307, doi:10.1029/2012JD017934.

Nowak, J. B., et al. (2004), Gas-phase chemical characteristics of Asian emission plumes observed during ITCT 2K2 over the eastern North Pacific Ocean, *J. Geophys. Res., 109*, D23S19, doi:10.1029/2003JD004488.

Olivier, J. G. J., and J. J. M. Berdowski (2001), Global emissions sources and sinks, in: The Climate System, edited by: Berdowski, J., R. Guicherit, and B. J. Heij, A. A. Balkema Publisher/Swets & Zeitlinger Publishers, Lisse, The Netherlands, 33-78.

Parazoo, N. C., A. S. Denning, S. R. Kawa, S. Pawson, and R. Lokupitiya (2012), CO_2 flux estimation errors associated with moist atmospheric processes, *Atmos. Phys. Chem., 12,* 6405-6416, doi:10.5194/acp-12-6405-2012.

Park, R. J., D. J. Jacob, B. D. Field, R. M. Yantosca, and M. Chin (2004), Natural and transboundary pollution influences on sulfate-nitrate-ammonium aerosols in the United States: implications for policy, *J. Geophys. Res., 109*, D15204, doi:10.1029/2003JD004473.

Parrish, D. D., J. S. Holloway, M. Trainer, P. C. Murphy, F. L. Forbes, and F. C. Fehsenfeld (1993), Export of North American pollution ozone to the North Atlantic Ocean, *Science, 259,* 1436-1439, doi:10.1126/science.259.5100.1436.

Parrish, D. D., M. Trainer, J. S. Holloway, J. E. Lee, M. S. Warshawsky, F. C. Fehsenfeld, G. L. Forbes, and J. L. Moody (1998), Export of North American ozone pollution to the North Atlantic Ocean, *J. Geophys. Res., 103*, 13357-13376, doi:10.1029/98JD00376.

Parrish, D. D., J. S. Holloway, R. Jakoubek, M. Trainer, T. B. Ryerson, G. Hubler, and F. C. Fehsenfeld (2000), Mixing of anthropogenic pollution with stratospheric ozone: A case study from the North Atlantic wintertime troposphere, *J. Geophys. Res., 105*, 24363-24374, doi:10.1029/2000JD900291.

Price, H. U., D. A. Jaffe, O. R. Cooper, and P. V. Doskey (2004), Photochemistry, ozone production, and dilution during long-range transport episodes from Eurasia to the northwest United States, *J. Geophys. Res., 109*, D23S13, doi:10.1029/2003JD004400.

Rodgers, C. D (2000), Inverse method for atmospheric sounding: Theory and practice, World Sci., Hackensack, New Jersey.

Sauvage, B., V. Thouret, A. M. Thompson, J. C. Witte, J.-P. Cammas, P. Nedelec, and G. Athier (2006), Enhanced view of the "tropical Atlantic ozone paradox" and "zonal wave one" from the in situ MOZAIC and SHADOZ data, *J. Geophys. Res., 111*, D1, doi:10.1029/2005JD006241.

Sauvage, B., R. V. Martin, A. van Donkelaar, and J. R. Ziemke (2007), Quantification of the factors controlling tropical tropospheric ozone and the South Atlantic maximum, *J. Geophys. Res., 112,* D11309, doi:10.1029/2006JD008008.

Schneider, H. R., D. B. A. Jones, G. Y. Shi, and M. B. McElroy (2000), Analysis of residual mean transport in the stratosphere, 1. Model description and comparison with satellite data, *J. Geophys. Res., 105*, 19991-20011, doi:10.1029/2000JD900213.

Spurr, R. J. D (2006), VLIDORT: A linearized pseudo-spherical vector discrete ordinate radiative transfer code for forward model and retrieval studies in multilayer scattering media, *J. Quant. Spectrosc. Ra., 102*, 316-342, doi:10.1016/j.jqsrt.2006.05.005.

Stevenson, D. S., et al. (2006), Multimodel ensemble simulations of present-day and near-future tropospheric ozone, *J. Geophys. Res., 111*, D08301, doi:10.1029/2005JD006338.

Susskind, J., C. D. Barnet, and J. M. Blaisdell (2003), Retrieval of atmospheric and surface parameters from AIRS/AMSU/HSB data in the presence of clouds, *IEEE T. Geosci. Remote, 41*, 2, 390–409, doi:10.1109/TGRS.2002.808236.

Terao, Y., J. A. Logan, A. R. Douglass, and R. S. Stolarski (2008), Contribution of stratospheric ozone to the interannual variability of tropospheric ozone in the northern extratropics, *J. Geophys. Res., 113*, D18309, doi:10.1029/2008JD009854.

Thompson, A. M., K. E. Pickering, D. P. McNamara, M. R. Schoeberl, R. D. Hudson, J. H. Kim, E. V. Browell, V. W. J. H. Kirchoff, and D. Nganga (1996), Where did tropospheric ozone over southern Africa and the tropical Atlantic come from in October 1992? Insights from TOMS, GTE TRACE A, and SAFARI 1992, *J. Geophys. Res., 101*(D19), 24251-24278, doi:10.1029/96JD01463.

Thompson, A. M., B. G. Doddridge, J. C. Witte, R. D. Hudson, W. T. Luke, J. E. Johnson, JB. J. Johnson, S. J., Oltmans, and R. Weiler (2000), A tropical Atlantic paradox: Shipboard and satellite views of a tropospheric ozone maximum and wave-one in January–February 1999, *Geophys. Res. Lett., 27*, 3317–3320, doi:10.1029/1999GL011273.

van der Werf, G. R., J. T. Randerson, L. Giglio, G. J. Collatz, M. Mu, P. S. Kasibhatla, D. C. Morton, R. S. DeFries, Y. Jin, and T. T. van Leeuwen (2010), Global fire emissions and the contribution of deforestation, savanna, forest, agricultural, and peat fires (1997-2009), *Atmos. Chem. Phys., 10,* 11707-11735, doi:10.5194/acp-10-11707-2010.

van Donkelaar, A., et al. (2008), Analysis of aircraft and satellite measurements from the Intercontinental Chemical Transport Experiment (INTEX-B) to quantify long-range transport of East Asian sulfur to Canada, *Atmos. Chem. Phys. 8*, 2999-3014, doi:10.5194/acp-8-2999-2008.

van het Bolscher, M., J. Pereira, A. Spessa, S. Dalsoren, T. van Nojie, and S. Szopa (2008), REanalysis of the TROpospheric chemical composition over the past 40 years: A long-term global modeling study of tropospheric chemistry funded under the 5th EU framework programme, edited by: Schultz, M., and S. Rast, Rep. EVK2-CT-2002-00170, Max Planck Inst. for Meteorol., Hamburg, Germany, 1-77.

Vestreng, V., and H. Klein, H (2002), Emission data reported to UN-ECE/EMEP. Quality assurance and trend analysis and Presentation of WebDab, MSC-W Status Report 2002, Norwegian Meteorological Institute, Oslo, Norway.

Voulgarakis, A., P. J. Telford, A. M. Aghedo, P. Braesicke, G. Faluvegi, N. L., Abraham, K. W. Bowman, J. A. Pyle, D. T. Shindell (2010), Global multi-year O_3-CO correlation patterns from models and TES satellite observations, *Atmos. Chem. Phys., 11*, 5819–5838, doi:10.5194/acp-10-2491-2010.

Warner, J. X., M. M. Comer, C. D. Barnet, W. W. McMillan, W. Wolf, E. Maddy, and G. Sachse (2007), A comparison of satellite tropospheric carbon monoxide measurements from AIRS and MOPITT during INTEX-A, *J. Geophys, Res., 112*, D12S17, doi:10.1029/2006JD007925.

Warner, J. X., Z. Wei, L. L. Strow, C. D. Barnet, L. C. Sparling, G. Diskin, and G. Sachse, G (2010), Improved agreement of AIRS tropospheric carbon monoxide products with other EOS sensors using optimal estimation retrievals, *Atmos. Chem. Phys., 10*, 9521-9533, doi:10.5194/acp-10-9521-2010.

Waugh, D. W., and L. M. Polvani (2000), Climatology of Intrusions into the Tropical Upper Troposphere, *Geophys. Res. Lett., 27*, 3857-3860, doi:10.1029/2000GL012250.

Wild, O. (2007), Modeling the global tropospheric ozone budget: exploring the variability in current models, *Atmos. Chem. Phys., 7*, 2643–2660, doi:10.5194/acp-7-2643-2007.

Wu, S., L. J. Mickley, D. J. Jacob, J. A. Logan, R. M. Yantosca, and D. Rind (2007), Why are there large differences between models in global budgets of tropospheric ozone?, *J. Geophys. Res., 112*, D05302, doi:10.1029/2006JD007801.

Yevich, R., and J. A. Logan (2003), An assesment of biofuel use and burning of agricultural

waste in the developing world, *Global Biogeochem. Cycles, 17*(4), 1095, doi:10.1029/2002GB001952.

Yurganov, L. N., W. W. McMillan, A. V. Dzhola, E. I. Grechko, N. B. Johnes, and G. R. van der Werf (2008), Global AIRS and MOPITT CO measurements: Validation, comparison, and links to biomass burning variations and carbon cycle, *J. Geophys. Res., 113*, D09301, doi:10.1029/2007JD009229.

Yurganov, L., W. W. McMillan, E. Grechko, and A. Dzhola (2010), Analysis of global and regional CO burdens measured from space between 2000 and 2009 and validated by ground-based solar tracking spectrometers, *Atmos. Chem. Phys., 10*, 3479-3494, doi:10.5194/acp-10-3479-2010.

Zahn, A., C. A. M. Brenninkmeijer, W. A. H. Asman, P. J. Crutzen, G. Heinrich, H. Fischer, J. W. M. Cuijpers, and P. F. J. van Velthoven (2002), Budgets of O3 and CO in the upper troposphere: CARIBIC passenger aircraft results 1997-2001, *J. Geophys. Res., 107*(D17), 4337, doi:10.1029/2001JD001529.

Zhang, L., et al. (2006), Ozone-CO correlations determined by the TES satellite instrument in continental outflow regions, *Geophys. Res. Lett., 33*, L18804, doi:10.1029/2006GL026399.

Zhang, L., et al. (2008), Transpacific transport of ozone pollution and the effect of recent Asian emission increases on air quality in North America: an integrated analysis using satellite, aircraft, ozonesonde, and surface observations, *Atmos. Chem. Phys., 8,* 6117-6136, doi:10.5194/acp-8-6117-2008.

Zhang, L., D. J. Jacob, X. Liu, J. A. Logan, K. Chance, A. Eldering, and B. R. Bojkov (2010), Intercomparison methods for satellite measurements of atmospheric composition: application to tropospheric ozone from TES and OMI, *Atmos. Chem. Phys., 10*, 4725-4739, doi:10.5194/acp-10-4725-2010.

Zhang, Q., et al. (2009), Asian emissions in 2006 for the NASA INTEX-B mission, *Atmos. Chem. Phys., 9*, 5131–5153, doi:10.5194/acp-9-5131-2009.

Chapter 3.

Sensitivity of population smoke exposure to fire locations in Equatorial Asia[1]

Abstract

High smoke concentrations in Equatorial Asia, primarily from land conversion to oil palm plantations, affect a densely populated region and represent a serious but poorly quantified public health concern. Continued expansion of the oil palm industry is expected but the resulting population exposure to smoke is highly dependent on where this expansion takes place. We use the adjoint of the GEOS-Chem chemical transport model to map the sensitivity of smoke concentrations in major Equatorial Asian cities, and for the population-weighted region, to the locations of the fires. We find that fires in southern Sumatra are particularly detrimental, and that a land management policy protecting peatswamp forests in Southeast Sumatra would be of great public health benefit. Our adjoint sensitivities can be used to immediately infer population exposure to smoke for any future fire emission scenario.

3.1 Introduction

Global palm oil production has more than doubled since 2000 in response to soaring demand [*FAO, 2013*]. Indonesia and Malaysia together account for 86% of the world's

[1]Kim, P. S., D. J. Jacob, L. J. Mickley, S. N. Koplitz, M. E. Marlier, R. S. DeFries, S. S. Myers, B. N. Chew, and Y. H. Mao (2015), Sensitivity of population smoke exposure to fire locations in Equatorial Asia, *Atmos. Environ., 102,* 11-17, doi:10.1016/j.atmosenv.2014.09.045.

production and Indonesia plans to further double its output by 2020 [*AFP, 2009; Koh and Ghazoul, 2010*]. The demand for palm oil is driving rapid deforestation to clear land for new plantations [*Koh et al., 2011; Miettinen et al. 2012*]. The area covered by oil palm plantations in Indonesia tripled from 2000 to 2012 [*FAO, 2013*]. The land is mainly cleared and managed by fire. The resulting smoke pollutes the airshed of one of the most densely populated regions of the world. According to *Marlier et al.* [2013], the unusually large fire season of 1997 resulted in 10,000 excess deaths from smoke exposure in Equatorial Asia. More recently, Sumatran fires in June 2013 caused a 24-h maximum particulate matter (PM) concentration of 300 μg m^{-3} in Singapore, far exceeding the 25 μg m^{-3} air quality guideline from the World Health Organization [*WHO, 2005*].

The fire season in Equatorial Asia is typically July - November (dry season), with large interannual variation in intensity [*van der Werf et al., 2010*] driven in part by the El Nino-Southern Oscillation and associated dryness [*Reid et al., 2012, 2013*]. Presently there is less interannual variability in the location of the fires, with land conversion mostly occurring in the South Sumatran lowlands and the southern and western coasts of Borneo [*Miettinen et al., 2010*].

The fire plumes are transported by the prevailing southwesterly flow (**Figure 3.1**) such that some population centers are minimally affected by the smoke (e.g., Jakarta), while others are heavily affected (e.g., Singapore). Fires in different areas have very different public health implications depending on the population downwind. Public health costs could be reduced by targeting sensitive areas for conservation while allowing palm oil development in other areas. Previous studies have examined the transport of smoke in Equatorial Asia using chemical transport model (CTM) simulations [*Heil et al., 2007; Hyer and Chew, 2010; Wang et al., 2013*] and trajectory analyses [*Koe et al. 2001; He et al. 2010; Atwood et al., 2013*]. They have

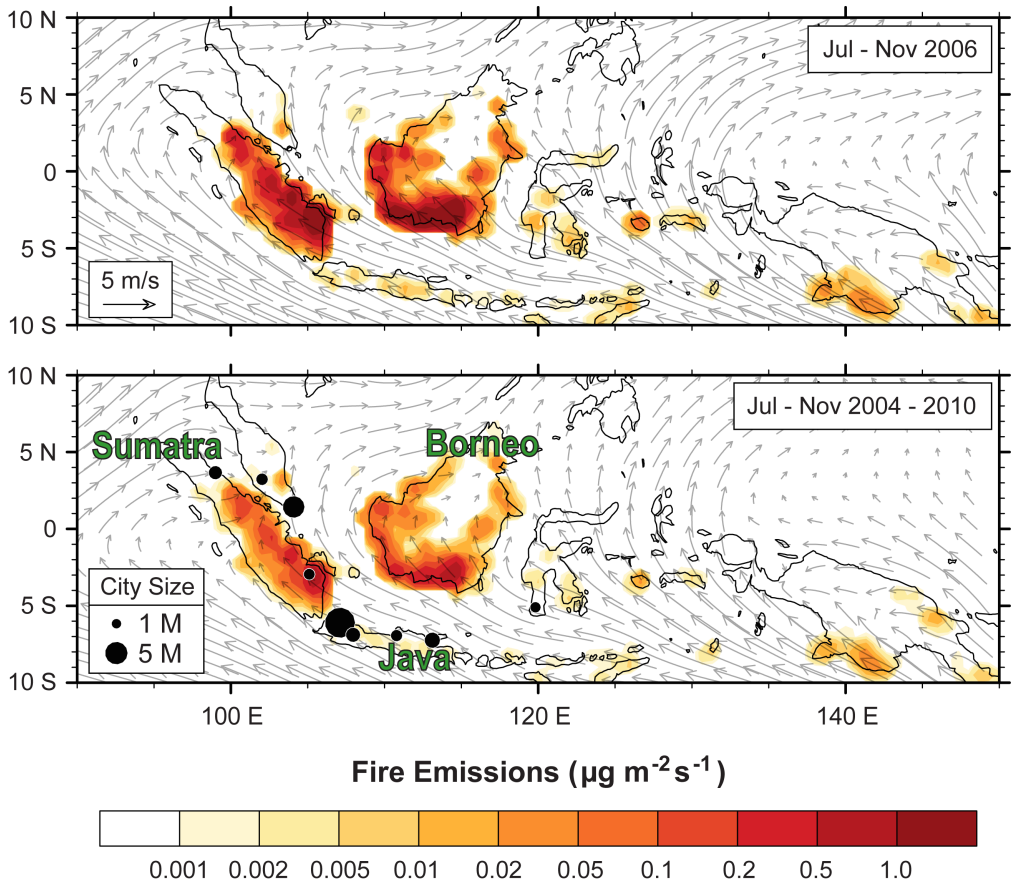

Figure 3.1: Fire emissions and mean 0-1 km vector winds in Equatorial Asia in July - November. The top panel is for 2006 (a high fire year) and the bottom panel is the 2004-2010 mean. Fire emissions are from the GFED3 inventory, increased by 50% to account for small fires (see text). Winds are from GEOS-5 assimilated meteorological data. Also shown are the locations of cities with more than one million people.

highlighted the importance of peat burning in Sumatra and Borneo on downstream surface air quality [*Heil et al., 2007*] as well as the complexity of local scale meteorological phenomena, including the sea-breeze effect and surface topography [*Wang et al., 2013*].

Here we use the adjoint of the GEOS-Chem CTM [*Bey et al., 2001; Henze et al., 2007*] to map the sensitivity of smoke concentrations to fire location for selected urban receptor locations in Equatorial Asia as well as for the entire population of the region. The adjoint is a computationally efficient method to determine the sensitivity of model output to many input

parameters [*Errico and Vukicevic, 1992*]. Our work provides a basis to identify where fires could most effectively be restricted to reduce population exposure, and to readily determine the exposure associated with any future land management scenarios.

3.2 Materials and Methods

3.2.1 The GEOS-Chem CTM and its Adjoint

We use GEOS-Chem v8-02-01 (www.geos-chem.org) driven by assimilated meteorological data from the Goddard Earth Observing System (GEOS-5) of the NASA Modeling and Assimilation Office (GMAO). The data have a native horizontal resolution of 0.50° x 0.67° with 72 pressure levels and 6-h temporal frequency (3-h for surface variables and mixing depths). We focus on simulating primary PM (smoke) emitted by the fires as organic and black carbon (OC/BC). The OC/BC simulation in GEOS-Chem is described by *Wang et al.* [2011]. Open fire emissions are from the GFED3 inventory [*Giglio et al., 2010; van der Werf et al., 2010*] with monthly resolution. The standard GFED3 product does not consider small fires, which account for one third of total fire emissions in Equatorial Asia [*Randerson et al., 2012*]. We therefore increase the GFED3 emissions by 50%.

Figure 3.1 shows the spatial distribution of fire emissions in Equatorial Asia for 2006 and for 2004-2010, and **Figure 3.2** (top panel) shows the interannual variability in total fire emissions for the region. 2006 was a high fire year associated with El Nino conditions [*van der Werf et al., 2010; Reid et al., 2012*] while 2010 had almost no fires. The fires are mainly in Sumatra and Borneo for all years. Sumatra accounts for 36-60% of total regional emissions depending on the year (2004-2009). Emissions are highest in the peatlands of southeastern

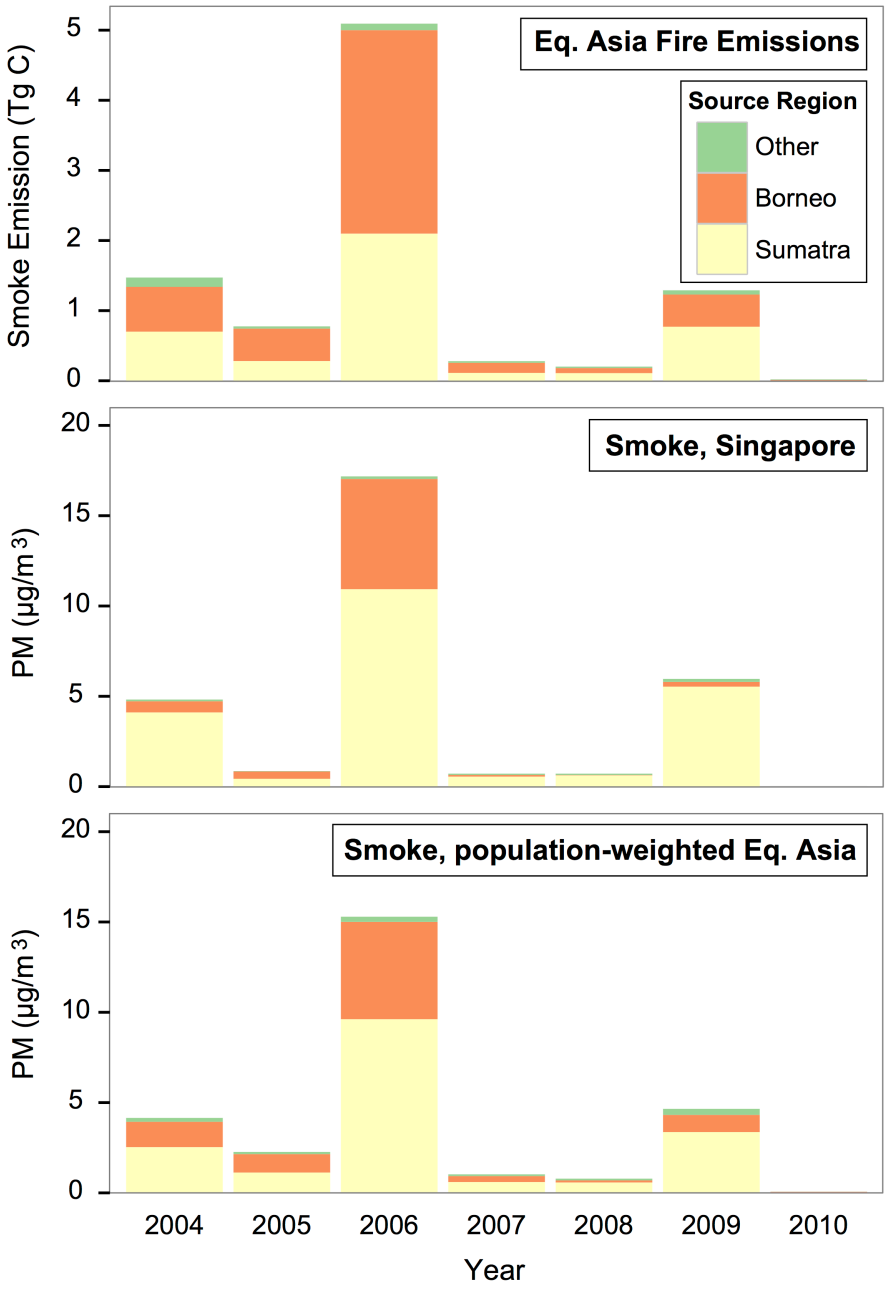

Figure 3.2: Interannual variability in smoke emissions and associated population exposure in Equatorial Asia (domain of **Figure 3.1**). The top panel shows total July-November emissions and the bottom panels show mean July-November smoke concentrations for Singapore and for population-weighted Equatorial Asia computed from the GEOS-Chem adjoint (Equation 1) with 2006 meteorology. The smoke concentrations are partitioned into contributions from fires in Borneo, Sumatra, and other regions.

Sumatra and southern Borneo.

The GEOS-Chem results presented here are for a simulation with the native 0.50^o x 0.67^o horizontal resolution over East Asia [70^o – 150^o E, 11^o S – 55^o N; *Chen et al., 2009*], nested within a global simulation with 4^o x 5^o horizontal resolution that provides dynamic boundary conditions. We focus on the 2006 fire season (July - November) following a 1-year initialization. As shown in **Figure 3.1**, the boundary layer winds (0-1 km) in 2006 were typical of the 2004 - 2010 mean.

We use the GEOS-Chem adjoint version 34 [*Kopacz et al., 2011*] for source attribution of the simulated smoke concentrations at selected receptor sites (Singapore, Palembang, and Jakarta) and for the whole population-weighted Equatorial Asia region (population distribution from http://web.ornl.gov/sci/landscan). The adjoint simulation is conducted for the July - November duration of the fire season [t_o, t_1]. A single simulation with the adjoint model operating backward in time over [t_1, t_o] yields the complete time-dependent footprint of sources contributing to the smoke concentrations at a particular receptor site and for any averaging time. The GEOS-Chem adjoint has previously been used in this manner to determine the origin of BC/OC aerosols in the Himalayas [*Kopacz et al., 2011*].

Smoke concentrations in GEOS-Chem are proportional to emissions so that the total smoke mass concentration $PM(\mathbf{x_R}, t')$ at receptor site $\mathbf{x_R}$ and time t' is given by

$$PM(\mathbf{x_R}, t') = \int_{t_o}^{t'} \iint_{\mathbf{x}} \frac{\partial PM(\mathbf{x_R}, t')}{\partial E(\mathbf{x}, t)} E(\mathbf{x}, t)\, d\mathbf{x}\, dt \qquad [1]$$

where $E(\mathbf{x}, t)$ is the emission flux (g m^{-2} s^{-1}) at location $\mathbf{x}$ and time $t < t'$, t_o is the beginning of the fire season, and the spatial integration is over the entire emitting domain. One adjoint simulation conducted over the time period [t_1, t_o] provides the ensemble of sensitivities $\partial PM(\mathbf{x_R}, t')/\partial E(\mathbf{x}, t)$

for PM at a selected receptor site $\mathbf{x_R}$ and at all times t' to the emissions for all domain grid squares ($\mathbf{x}$) and all prior times (t < t'). Instead of a single receptor location, the adjoint can also provide the same ensemble of sensitivities for the population-weighted mean smoke concentration ($\overline{PM}$) over the entire Equatorial Asia domain (i.e. $\partial\overline{PM}$(t')/∂E($\mathbf{x}$, t)).

3.2.2 Surface PM_{10} Observations

Measurements of 24-h mean PM_{10} (mass concentration of particulate matter finer than 10 μm aerodynamic diameter) are available from a network of surface sites [*Hyer and Chew, 2010*] maintained by the Malaysian Department of the Environment (http://www.doe.gov.my/) and the Singaporean National Environment Agency (http://www.nea.gov.sg/). The site locations (marked on the map in **Figure 3.3**) are predominantly in urban areas and away from the main fire locations. We estimate the smoke concentration at each site in the observations by subtracting the mean concentration for the bracketing non-burning months (June and December).

3.2.3 Future Fire Scenarios

The adjoint sensitivities ∂PM($\mathbf{x_R}$, *t'*)/∂E($\mathbf{x}$, *t*) described in Section 3.2.1 can be used with Equation 1 to immediately derive population exposure to smoke under any future emission scenario E($\mathbf{x}$, *t*). Here we examine the impact of two possible 2009 - 2032 future emission scenarios for Sumatra described by *Marlier et al.* [2014]: a "High Oil Palm" scenario with continued rapid plantation expansion (including into peatswamps where fuel loads are particularly high), and a "Green Vision with Peat Protection" scenario that promotes sustainable development and where all remaining peatswamp forests are preserved. *Marlier et al.* [2014] give mean Sumatran emissions of 256 Gg a^{-1} for present-day (2004-2010), 414 Gg a^{-1} for the

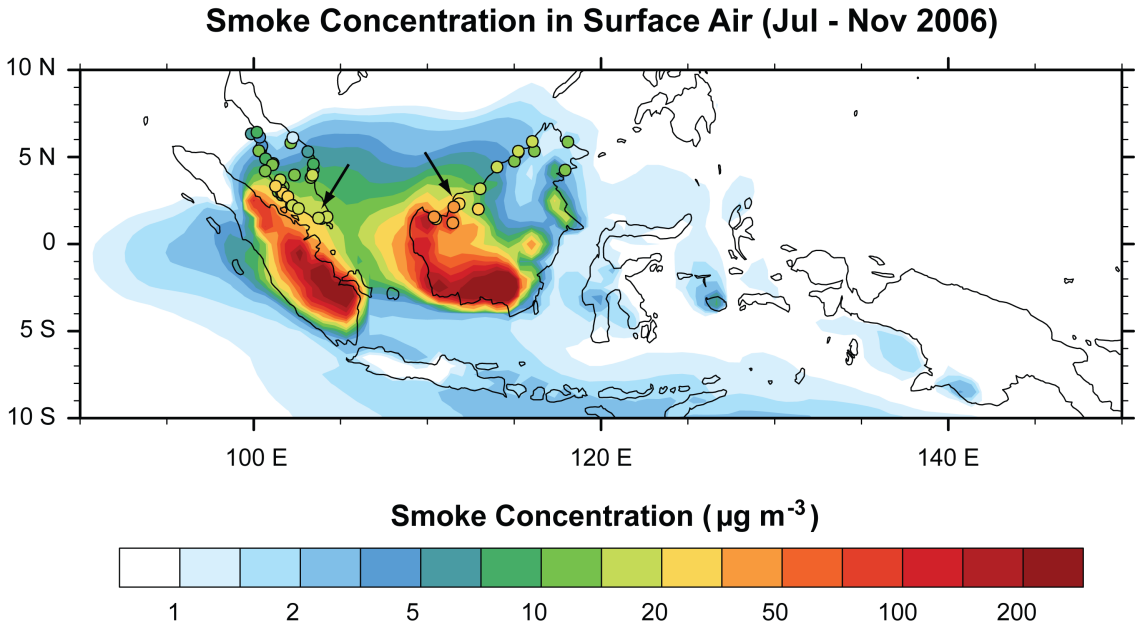

Figure 3.3: Mean smoke concentration in surface air for July – November 2006, observed at a network of sites (circles; see text for details) and simulated by GEOS-Chem. Arrows point to the locations of Singapore and Sibu (western Borneo) for which time series of concentrations are shown in **Figure 3.4**.

High Oil Palm scenario, and 186 Gg a^{-1} for the Peat Protection scenario. Their present-day emission estimates are 40% lower than ours for the same time period, likely due to their explicit treatment of small fires compared to our application of a 50% increase to the standard GFED3 product. We have some confidence in our estimate on the basis of better comparisons to observed smoke concentrations (next section). The *Marlier et al.* [2014] present-day Sumatran emissions nevertheless serve as a baseline against which their future projections can be compared.

3.3 Results and Discussion

3.3.1 Smoke Concentrations

The mean surface air smoke concentrations in July-November 2006 observed at the

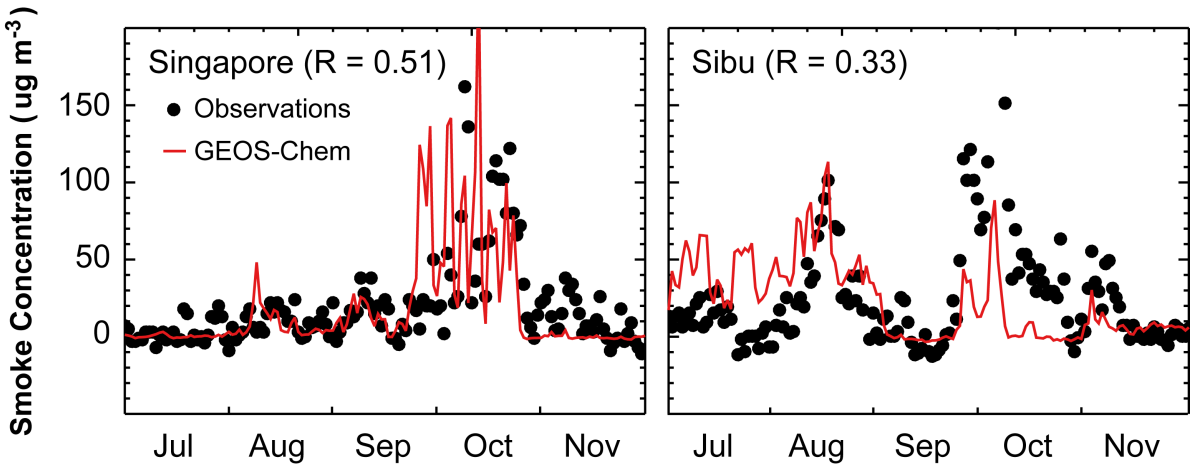

Figure 3.4: Time series of observed and simulated 24-h surface mean smoke concentrations at Singapore and Sibu (western Borneo). Temporal correlation coefficients are inset. Site locations are indicated by arrows in **Figure 3.3**.

surface monitoring stations and simulated by GEOS-Chem are shown in **Figure 3.3**. Observed smoke concentrations are typically 10-50 μg m^{-3} above the baseline PM_{10} of 21-71 μg m^{-3} inferred from June and December observations. The smoke concentrations and spatial patterns are well captured by the model, with a mean relative bias of -27% and a spatial correlation coefficient $r = 0.84$ for the ensemble of sites ($n = 50$). The model misses the smoke influence in northeastern Borneo and this likely reflects difficulty in simulating transport around the Tama Abu mountain range [*Wang et al., 2013*]. The model simulates July-November mean concentrations in excess of 100 μg m^{-3} in large areas of southern Sumatra and southern Borneo but no observations are available there. The city of Palembang (1.5 million people) in southern Sumatra experiences a seasonal mean concentration of 300 μg m^{-3} in the model.

Time series of simulated and observed smoke concentrations are shown in **Figure 3.4** for Singapore and for Sibu (western Borneo, where mean observed smoke concentrations are particularly high as shown in **Figure 3.3**). Time series for all other sites are in the **Appendix**. The model often does not capture the magnitude and timing of individual events and this is

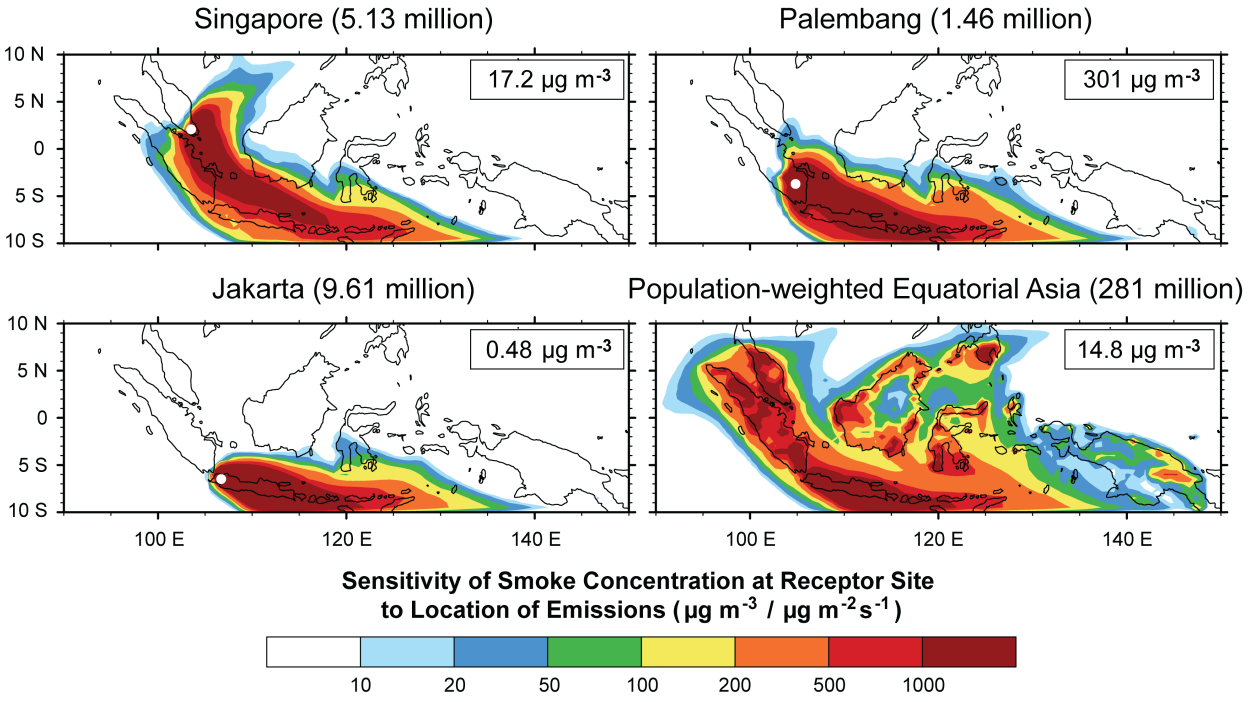

Figure 3.5: Sensitivity of mean smoke concentrations in July - November 2006 to the location of fire emissions for three large cities and for all of Equatorial Asia weighted by population (city locations indicated by white circles, population in parentheses). Values are GEOS-Chem adjoint mean sensitivities. The simulated July - November mean smoke concentration for each receptor is shown inset.

attributable at least in part to errors in the timing of emissions and in small-scale plume transport. The temporal correlation coefficient *r* for 24-h smoke concentrations at individual sites ranges from 0.7 to no correlation (four sites in western Borneo).

3.3.2 GEOS-Chem Adjoint Sensitivities

Figure 3.5 shows the sensitivities of mean smoke concentrations at Singapore, Palembang, Jakarta, and population-weighted Equatorial Asia during July – November 2006 to the mean fire emissions over the same time period. Sensitivities are generally largest for fires to the southeast, reflecting the prevailing flow (**Figure 3.1**). Singapore is particularly sensitive to fires in southeastern Sumatra. Jakarta is not sensitive to fires in Sumatra or Borneo. The

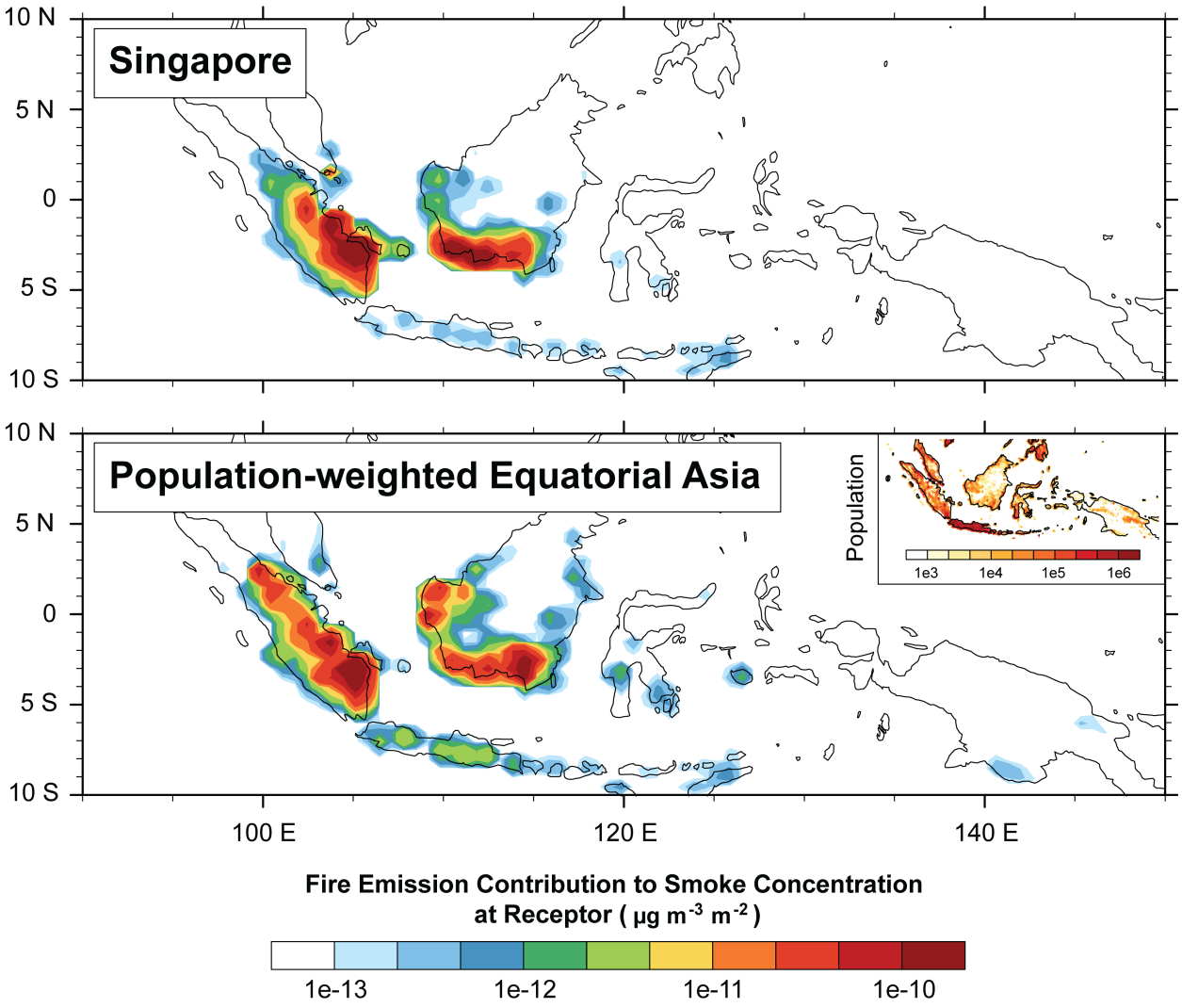

Figure 3.6: Spatially resolved contributions of fire emissions to July - November 2006 mean smoke concentrations in Singapore (top) and for all of Equatorial Asia weighted by the population distribution shown inset (bottom).

Equatorial Asian population as a whole is much more sensitive to fires in Sumatra than in Borneo. It is most sensitive to fires in Java because of high population density but fire activity there is low.

The sensitivities computed in this manner can be combined with knowledge of emission patterns to map the contributions from different source regions to the smoke concentrations at the receptor sites (Equation 1). **Figure 3.6** shows the contributions to mean smoke concentrations for

July-November 2006 in Singapore and for population-weighted Equatorial Asia. Sumatra was responsible for 37% of total fire emissions in Equatorial Asia in 2006 but contributed to 64% of the smoke concentration in Singapore and 63% of the smoke concentration to which the whole Equatorial Asian population was exposed. Suppressing fires in southeastern Sumatra would be of particular public health benefit both for Singapore and for Equatorial Asia as a whole.

There is large year-to-year variability in present day fire emissions and the relative contributions from Sumatra and Borneo (**Figure 3.2**). We applied Equation 1 to individual years of 2004-2010 and results are shown in the bottom panels of **Figure 3.2** as the regional contributions from Sumatra and Borneo to smoke concentration at Singapore and for population-weighted Equatorial Asia. Despite this variability in fire emissions, we find that Sumatran fires contribute the majority of the smoke burden for Singapore and for population-weighted Equatorial Asia in all years in 2004 - 2009.

We can use the adjoint sensitivities to readily estimate the smoke exposure for any future land management scenario and this is illustrated in **Figure 3.7** with the Sumatra fire scenarios of *Marlier et al.* [2014]. The Figure shows the fire emissions for the different scenarios, and inset are the mean July-November PM concentrations in Singapore and population-weighted Equatorial Asia contributed by the fires. Values are much lower than **Figure 3.1** because they are for an average fire season, consider only Sumatran fires, and assume a lower base emission estimate, as discussed above. The smoke concentration in Singapore drops for both future scenarios compared to present-day due to a shift of emissions away from Southeast Sumatra where Singapore is most sensitive (**Figure 3.5**). By contrast, the population-weighted mean concentration increases by 60% under the High Oil Palm scenario. The Green Vision with Peat Protection scenario reduces mean smoke concentrations relative to the High Oil Palm scenario

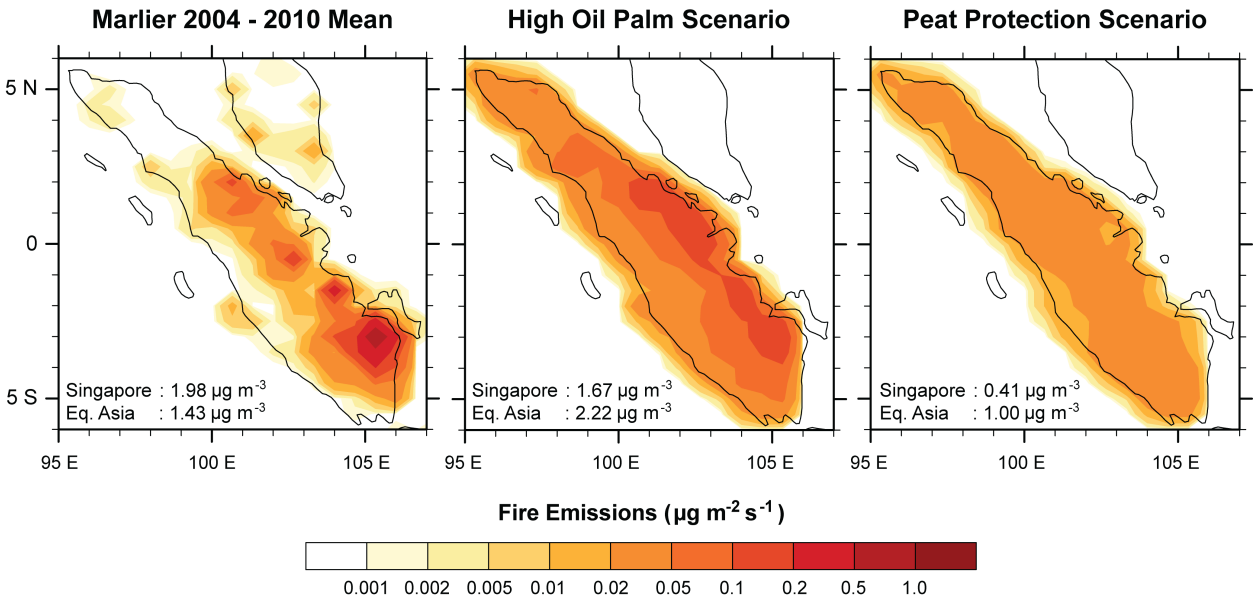

Figure 3.7: Mean July – November fire emissions in Sumatra from *Marlier et al.* [2014] for the present (2004 – 2010) and for two future scenarios, "High Oil Palm" and "Green Vision with Peat Protection" (see text). The emissions are plotted on the same scale as **Figure 3.1**. The Sumatran contribution to simulated July - November mean smoke concentration for Singapore and for population-weighted Equatorial Asia is shown inset.

by a factor of 4 for Singapore and a factor of 2 for the population-weighted mean.

The adjoint sensitivities computed here (**Figure 3.5**) allow immediate inference of smoke concentrations at selected receptor sites for any fire scenario. The smoke concentrations can be converted to public health costs using standard methods [*Johnston et al., 2012; Marlier et al., 2013*]. In this manner and together with the work of *Marlier et al.* [2014], an integrated system can be developed for policy analysts to quantify the health cost endpoints of different land management options for the region. We plan to improve our tool in the future through the generation of adjoint sensitivities for other years to yield probability distribution functions of smoke concentrations that account for interannual variability in meteorology. Use of a finer-resolution regional CTM to generate the adjoint sensitivities could also provide an improved simulation of smoke transport and more geographically precise source-receptor relationships. A

GEOS-Chem capability at 0.25^{o} x 0.3125^{o} (25 x 25 km^2) has recently been developed [*Kim et al., 2014*] and can be applied in the future.

Acknowledgements

Data supporting **Figures 3.3** and **3.4** is available upon request to BNC. Input files necessary for GEOS-Chem are available at http://geos-chem.org/. This work was funded by the Rockefeller Foundation and the Gordon and Betty Moore Foundation through the Health & Ecosystems: Analysis of Linkages (HEAL) program, and by a Department of Energy Office of Science Graduate Fellowship to PSK made possible in part by the American Recovery and Reinvestment Act of 2009, administered by ORISE-ORAU under contract no. DE-AC05-06OR23100. The authors would like to thank Singapore's National Environment Agency and Malaysia's Department of Environment for collecting and archiving the surface air quality data. We thank Zifeng Lu for his assistance with the population data. We thank two anonymous reviewers for their helpful comments that led to improvements to the manuscript.

References

AFP (May, 27, 2009), Indonesia to double palm oil production by 2020, AFP Asian Edition. Available at http://www.thefreelibrary.com/Indonesia+to+double+palm +oil+production+by+2020-a01611882134.

Atwood, S. A., J. S. Reid, S. M. Kreidenweis, L. E. Yu, S. V. Salinas, B. N. Chew, R. Balasubramanian (2013), Analysis of source regions for smoke events in Singapore for the 2009 El Nino burning season, *Atmos. Environ., 78,* 219-230, doi:10.1016/j.atmosenv.2013.04.047.

Bond, T. C., E. Bhardwaj, R. Dong, R. Jogani, S. Jung, C. Roden, D. G. Streets, and N. M. Trautmann (2007), Historical emissions of black and organic carbon aerosol from energy-related combustion, 1850-2000, *Global Biogeochem. Cycles, 21,* GB2018, doi:10.1029/2006GB002840.

Chen, D., Y. Wang, M. B. McElroy, K. He, R. M. Yantosca, and P. Le Sager (2009), Regional CO pollution and export in China simulated by the high-resolution nested-grid GEOS-Chem model, *Atmos. Chem. Phys., 9,* 3825-3839, doi:10.5194/acp-9-3825-2009.

Errico, R. M., and T. Vukicevic (1992), Sensitivity Analysis Using an Adjoint of the PSU-NCAR Mesoscale Model, *Mon. Wea. Rev., 120,* 1644-1660.

FAO (2013), FAOSTAT: Statistical Databases and Data-Sets, Food and Agriculture Organization of the United Nations (FAO), Rome, Italy.

Giglio, L., J. T. Randerson, G. R. van der Werf, P. S. Kasibhatla, G. J. Collatz, D C. Morton, and R. S. DeFries (2010), Assessing variability and long-term trends in burned area by merging multiple satellite fire products, *Biogeosciences, 7,* 1171-1186, doi:10.5194/bg-7-1171-2010.

He, J., B. Zielinska, and R. Balasubramanian (2010), Composition of semi-volatile organic compounds in the urban atmosphere of Singapore: influence of biomass burning, *Atmos. Chem. Phys., 10,* 11401-11413, doi:10.5194/acp-10-11401-2010.

Heil, A., B. Langmann, and E. Aldrian (2007), Indonesian peat and vegetation fire emissions: Study on factors influencing large-scale smoke haze pollution using a regional atmospheric chemistry model, *Mitig. Adapt. Strat. Glob. Change, 12,* 113-133, doi:10.1007/s11027-006-9045-6.

Henze, D. K., A. Hakami, and J. H. Seinfeld (2007), Development of the adjoint of GEOS-Chem, *Atmos. Chem. Phys., 7,* 2413-2433, doi:10.5194/acp-7-2413-2007.

Hyer, E. J., and B. N. Chew (2010), Aerosol transport model evaluation of an extreme smoke episode in Southeast Asia, *Atmos. Environ., 44,* 1422-1427, doi:10.1016/j.atmosenv.2010.01.043.

Johnston, F. H., S. B. Henderson, Y. Chen, J. T. Randerson, M. Marlier, R. S. DeFries, P. Kinney, D. M. J. S. Bowman, and M. Brauer (2012), Estimated Global Mortality Attributable to Smoke from Landscape Fires, *Environ. Health Perspect., 120,* 695 – 701, doi:10.1289/ehp.1104422.

Kim, P. S., D. J. Jacob, J. A. Fisher. J. L. Jimenez, J. W. Hair, K. R. Travis, L. Zhu, K. Yu (2014, April), Interpretation of SEAC^{4}RS Aerosol Observations over the Southeast US with the GEOS-Chem Chemical Transport Model, Poster presented at the SEAC^{4}RS Science Team Meeting, Boulder, CO.

Koe, L. C. C., A. F. Arellano, and J. L. McGregor (2001), Investigating the haze transport from 1997 biomass burning in Southeast Asia: Its impact upon Singapore, *Atmos. Environ., 35,* 2723-2734, doi:10.1016/s1352-2310(00)00395-2.

Koh, L. P. and J. Ghazoul (2010), Spatially explicit scenario analysis for reconciling agricultural expansion, forest protection, and carbon conservation in Indonesia, *Proc. Natl. Acad. Sci., 107,* 11140-11144, doi:10.1073/pnas.1000530107.

Koh, L. P., J. Miettinen, S. C. Liew, and J. Ghazoul (2011), Remotely sensed evidence of tropical pealand conversion to oil palm, *Proc. Natl. Acad. Sci., 108,* 5127-5132, doi:10.1073/pnas.1018776108.

Kopacz, M., D. L. Mauzerall, J. Wang, E. M. Leibensperger, D. K. Henze, and K. Singh (2011), Origin and radiative forcing of black carbon transported to the Himalayas and Tibetan Plateau, *Atmos. Chem. Phys., 11,* 2837-2852, doi:10.5194/acp-11-2837-2011.

Marlier, M. E., R. S. DeFries, A. Voulgarakis, P. L. Kinney, J. T. Randerson, D. T. Shindell, Y. Chen, and G. Faluvegi (2013), El Nino and health risks from landscape fire emissions in southeast Asia, *Nature Climate Change, 3,* 131-136, doi:10.1038/nclimate1658.

Marlier, M. E., R. DeFries, D. Pennington, E. Nelson, E. M. Ordway, J. Lewis, S. N. Koplitz, and L. J. Mickley (2014), Future fire emissions associated with projected land use change in Sumatra, *Global Change Biology,* doi:10.1111/gcb.12691, In Press.

Miettinen, J., C. Shi, and S. C. Liew (2010), Deforestation rates in insular Southeast Asia between 2000 and 2010, *Global Change Biology, 17,* 2261-2270, doi:10.1111/j.1365-2486.2011.02398.x.

Mietinnen, J., A. Hooijer, C. Shi, D. Tollenaar, R. Vernimmen, S. C. Liew, C. Malins, and S. E. Page (2012), Extent of industrial plantations on Southeast Asian peatlands in 2010 with analysis of historical expansion and future projections, *GCB Bioenergy, 4,* 908-918, doi:10.1111/j.1757-1707.2012.01172.x.

Oak Ridge National Laboratory (ORNL): LandScan High Resolution Global Population Data Set (http://web.ornl.gov/sci/landscan/landscan_documentation.shtml), Oak Ridge National

Laboratory, Oak Ridge, TN, USA, 2011.

Randerson, J. T., Y. Chen, G. R. van der Werf, B. M. Rogers, and D. C. Morton (2012), Global burned area and biomass burning emissions from small fires, *J. Geophys. Res., 117,* G04012, doi:10.1029/2012JG002128.

Reid, J. S., P. Xian, E. J. Hyer, M. K. Flatau, E. M. Ramirez, F. J. Turk, C. R. Sampson, C. Zhang, E. M. Fukada, and E. D. Maloney (2012), Mulit-scale meteorological conceptual analysis of observed active fire hotspot activity and smoke optical depth in the Maritime Continent, *Atmos. Chem. Phys., 12,* 2117 - 2147, doi:10.5194/acp-12-2117-2012.

Reid, J. S., E. J. Hyer, R. S. Johnson, B. N. Holben, R. J. Yokelson, J. Zhang, J. R. Campbell, S. A. Christopher, L. DiGirolamo, L. Giglio, R. E. Holz, C. Kearney, J. Miettinen, E. A. Reid, F. J. Turk, J. Wang, P. Xian, G. Zhao, R. Balasubramanian, B. N. Chew, S. Janjai, N. Lagrosas, P. Lestari, N.-H. Lin, M. Mahmud, A. X. Nguyen, B. Norris, N. T. K. Oanh, M. Oo, S. V. Salinas, E. J. Welton, S. C. Liew (2013), Observing and understanding the Southeast Asian aerosol system by remote sensing: An initial review and analysis for the Seven Southeast Asian Studies (7SEAS) program, *Atmos. Res., 122*, 403-468, doi:10.1016/j.atmosres.2012.06.005.

van der Werf, G. R., J. T. Randerson, L. Giglio, G. J. Collatz, M. Mu, P. S. Kasibhatla, D. C. Morton, R. S. DeFries, Y. Jin, and T. T. Leeuwen (2010), Global fire emissions and the contribution of deforestation, savanna, forest, agricultural, and peat fires (1997-2009), *Atmos. Chem. Phys., 10,* 11707-11735, doi:10.5194/acp-10-11707-2010.

Wang, J., C. Ge, Z. Yang, E. J. Hyer, J. S. Reid, B.-N. Chew, M. Mahmud, Y. Zhang, and M. Zhang (2013), Mesoscale modeling of smoke transport over the Southeast Asian Continent: Interplay of sea breeze, trade wind, typhoon, and topography, *Atmos. Res., 122,* 486-503, doi:10.1016/j.atmosres.2012.05.009.

Wang, Q., D. J. Jacob, J. A. Fisher, J. Mao, E. M. Leibensperger, C. C. Carouge, P. Le Sager, Y. Kondo, J. L. Jimenez, M. J. Cubison, and S. J. Doherty (2011), Sources of carbonaceous aerosols and deposited black carbon in the Arctic in winter-spring: implications for radiative forcing, *Atmos. Chem. Phys., 11,* 12453-12473, doi:10.5194/acp-11-12453-2011.

WHO (2006), WHO Air quality guidelines for particulate matter, ozone, nitrogen dioxide and sulfur dioxide.

Chapter 4.

Sources, seasonality, and trends of Southeast US aerosol: an integrated analysis of surface, aircraft, and satellite observations with the GEOS-Chem chemical transport model[1]

Abstract

We use an ensemble of surface (EPA CSN, IMPROVE, SEARCH, AERONET), aircraft (SEAC^{4}RS), and satellite (MODIS, MISR) observations over the Southeast US during the summer-fall of 2013 to better understand aerosol sources in the region and the relationship between surface particulate matter (PM) and aerosol optical depth (AOD). The GEOS-Chem global chemical transport model (CTM) with 25 x 25 km^2 resolution over North America is used as a common platform to interpret measurements of different aerosol variables made at different times and locations. Sulfate and organic aerosol (OA) are the main contributors to surface $PM_{2.5}$ (mass concentration of PM finer than 2.5 μm aerodynamic diameter) and AOD over the Southeast US, with OA acquiring an increasing role over the past decade as SO_2 emissions have declined. Biogenic isoprene and monoterpenes are the dominant source of OA, and may contribute to sulfate formation through the production of Criegee intermediates as SO_2 oxidants. 40% of the total aerosol column is above the planetary boundary layer (PBL), mostly from PBL ventilation. The sulfate aerosol is acidic, despite an excess of ammonia emissions, and this could

[1]Kim, P. S., et al. (2015), Sources, seasonality, and trends of Southeast US aerosol: an integrated analysis of surface, aircraft, and satellite observations with the GEOS-Chem chemical transport model, in prep.

reflect hindrance to sulfate-ammonium equilibrium by uptake of organic gases. The vertical profile of aerosol extinction over the Southeast US follows closely that of aerosol mass. GEOS-Chem reproduces total column aerosol mass over the Southeast US within 6% and column aerosol extinction within 16%. The large AOD decline from summer to winter is mainly driven by sharp declines in both sulfate and OA from August to October. These declines are due in part to a shutdown in isoprene/monoterpene emissions and in part to a UV-driven seasonal shift in photochemical regime from low-NO_x to high-NO_x conditions. Surface $PM_{2.5}$ shows far less summer-to-winter decrease than AOD due to compensating effects from a shallower and less ventilated PBL in winter. The SEAC4RS aircraft data demonstrate that the AODs measured from space are fundamentally consistent with surface $PM_{2.5.}$ This implies that satellites can be used reliably to infer $PM_{2.5}$ air quality if a good CTM representation of the aerosol vertical distribution is available.

4.1 Introduction

There is considerable interest in using satellite retrievals of aerosol optical depth (AOD) to map particulate matter concentrations (PM) in surface air and the implications for public health [*Y. Liu et al., 2004; H. Zhang et al., 2009; van Donkelaar et al., 2010, 2015; X. Hu et al., 2014*]. The relationship between PM and AOD is a function of the vertical distribution and optical properties of the aerosol. It is generally derived from a global chemical transport model (CTM) simulating the different aerosol components over the depth of the atmospheric column [*van Donkelaar et al., 2012, 2013; Boys et al., 2014*]. Sulfate and organic matter are the dominant aerosol components worldwide [*Q. Zhang et al., 2007; Jimenez et al., 2009*], thus it is

important to evaluate the ability of CTMs to simulate their concentrations and vertical distributions. Here we use the GEOS-Chem CTM to interpret a large ensemble of aerosol chemical and optical observations from surface, aircraft, and satellite platforms during the NASA SEAC^{4}RS campaign in the Southeast US in August-September 2013. Our objective is to better understand the relationship between PM and AOD, and the ability for CTMs to simulate it, with focus on the factors controlling sulfate and organic aerosol (OA).

The Southeast US is a region of particular interest for PM air quality and for aerosol radiative forcing of climate [*Goldstein et al., 2009*]. $PM_{2.5}$ (the mass concentration of particulate matter finer than 2.5 μm aerodynamic diameter, of most concern for public health) is in exceedance of the current US air quality standard, 12 μg m^{-3} on an annual mean basis, in several counties (http://www.epa.gov/airquality/particlepollution/actions.html). Concentrations have been decreasing in response to regulation targeted at protecting public health. **Figure 4.1** shows the summertime (JJA) mean concentrations of aerosol components for 2003-2013 from surface monitoring stations in the Southeast US managed by the US Environmental Protection Agency [*US EPA, 1999*]. Sulfate concentrations decreased by ~60% over the period, while OA concentrations decreased by ~30% [*Hand et al., 2012b; Blanchard et al., 2013; Hidy et al., 2014*]. These changes have shifted the relative importance of sulfate and OA, with implications for aerosol hygroscopicity, light extinction, and radiative forcing [*Attwood et al., 2014*]. Decreasing aerosol has been linked to rapid warming in the Southeast US over the past two decades [*Leibensperger et al., 2012ab*].

The sulfate decrease is driven by the decline of sulfur dioxide (SO_2) emissions from coal combustion [*Hand et al., 2012b*], though the mechanisms responsible for oxidation of SO_2 to sulfate are not well quantified. Better understanding of the mechanisms is important because dry

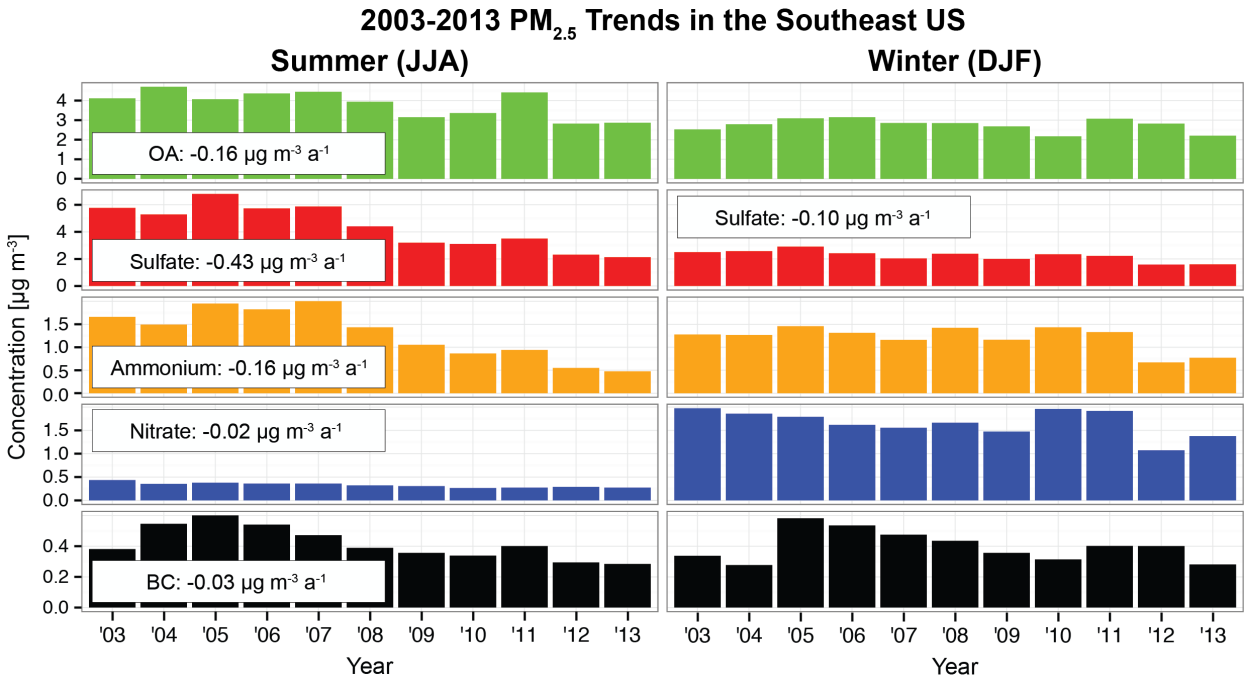

Figure 4.1: Trends in mean surface $PM_{2.5}$ in the Southeast US for 2003-2013. (Left) June-August averages for each component are calculated by combining data from the EPA CSN and IMPROVE networks over the Southeast US domain defined in **Figure 4.2**. Ammonium is only measured by CSN. Organic aerosol (OA) and black carbon (BC) are only from IMPROVE because of change in the CSN measurement protocol over the 2003-2013 period and differences in the OA measurements between the two networks (see text for details). OA is inferred here from measured organic carbon (OC) using an OA/OC mass ratio of 1.92 as in *Attwood et al.* [2014]. Note the different scales in different panels (sulfate and OA contribute most of $PM_{2.5}$). Trends are calculated using the Theil-Sen estimator. All trends are significant at the $\alpha = 0.05$ level. (Right) Same except for December-February. Only the sulfate trend is significant in winter.

deposition competes with oxidation as a sink of SO_2, so that faster oxidation produces more sulfate [*Chin and Jacob, 1996*]. Standard model mechanisms assume that SO_2 is oxidized to sulfate by the hydroxyl radical (OH) in the gas phase, and by hydrogen peroxide (H_2O_2) and ozone in clouds (aqueous phase). A model intercomparison by *McKeen et al.* [2007] for the Northeast US revealed a general failure of models to reproduce observed sulfate concentrations, sometimes by a factor of 2 or more. This could reflect errors in oxidation mechanisms, oxidant concentrations, or frequency of cloud processing. New laboratory data suggest that Criegee

intermediates (CIs) formed from alkene ozonolysis could be important SO_2 oxidants [*Mauldin et al., 2012; Welz et al., 2012*], especially over the summertime Southeast US where large emission of isoprene from vegetation is a source of CIs [*Pierce et al., 2013; Sarwar et al., 2014*].

The factors controlling OA are highly uncertain. OA originates from anthropogenic, biogenic, and open fire sources [*de Gouw and Jimenez, 2009*]. It is directly emitted as primary OA (POA), and also produced in the atmosphere as secondary OA (SOA) from oxidation of volatile organic compounds (VOCs). Current models cannot reproduce observed OA variability, implying fundamental deficiency in the model mechanisms [*Heald et al., 2006a; Tsigaridis et al., 2014*]. A key uncertainty for air quality policy is the fraction of OA that can be controlled [*Carlton et al., 2010*], as most of SOA is thought to be biogenic in origin. Gas/particle partitioning of organic material depends on the pre-existing aerosol concentration [*Donahue et al., 2006*], so that "biogenic" SOA may be enhanced in the presence of anthropogenic aerosol [*Weber et al., 2007*]. The SOA yield from VOC oxidation also depends on the concentration of nitrogen oxide radicals [$NO_x \equiv NO + NO_2$; *Kroll et al., 2005, 2006; A. Chan et al. 2010; Hoyle et al., 2011; Xu et al., 2014*]. NO_x in the Southeast US is mostly from fossil fuel combustion and is in decline due to emission controls [*Russell et al., 2012*], adding another complication in the relationship between OA concentrations and anthropogenic sources.

Long-term $PM_{2.5}$ records for the Southeast US are available from the EPA CSN, IMPROVE, and SEARCH networks of surface sites [*Malm et al., 1994; Edgerton et al., 2005; Solomon et al., 2014*]. Satellite measurements of AOD from the MODIS and MISR instruments have been operating continuously since 2000 [*Diner et al., 2005; Remer et al., 2005; Levy et al., 2013*]. Both surface and satellite observations show a strong aerosol seasonal cycle in the Southeast US, with a maximum in summer and minimum in winter. *Goldstein et al.* [2009]

observed that the amplitude of the seasonal cycle of $PM_{2.5}$ measured at surface sites [maximum/minimum ratio of ~1.5; *Hand et al., 2012a*] is much smaller than the seasonal cycle of AOD measured from space [ratio of ~3-4; *Alston et al., 2012*]. They hypothesized that this could be due to a summertime source of biogenic SOA aloft. Subsequent work by *Ford and Heald* [2013] supported that hypothesis on the basis of spaceborne CALIOP lidar measurements of elevated light extinction above the planetary boundary layer (PBL). As shown below, another simple explanation for the difference in seasonal amplitude between satellite AOD and surface $PM_{2.5}$ is the seasonal variation in the PBL height.

The NASA SEAC^{4}RS aircraft campaign in August-September 2013 [*Toon et al., 2015*] offers a powerful resource for better understanding the factors controlling aerosol concentrations in the Southeast US and the relationship between surface PM and AOD measured from space. The aircraft payload included measurements of aerosol composition, size distributions, and light extinction. Flights provided dense coverage of the Southeast US (**Figure 4.2**) including extensive PBL mapping and vertical profiling. AERONET sun photometers deployed across the region provided high-accuracy ground-based AOD measurements [*Holben et al., 1998*] (http://aeronet.gsfc.nasa.gov/new_web/dragon.html). Additional field campaigns focused on Southeast US air quality during summer 2013 included SENEX (aircraft) based in Tennessee [*Warneke et al., 2015*], DISCOVER-AQ (aircraft) based in Houston [*Crawford and Pickering, 2014*], and SOAS (surface) based in Alabama (http://soas2013.rutgers.edu). We use the GEOS-Chem CTM with 0.25^o x 0.3125^o horizontal resolution as a platform to exploit this ensemble of observational constraints by (1) determining the consistency between different measurements, (2) interpreting the measurements in terms of their implications for the sources of sulfate and OA in the Southeast US, (3) explaining the seasonal aerosol cycle in the satellite and surface data,

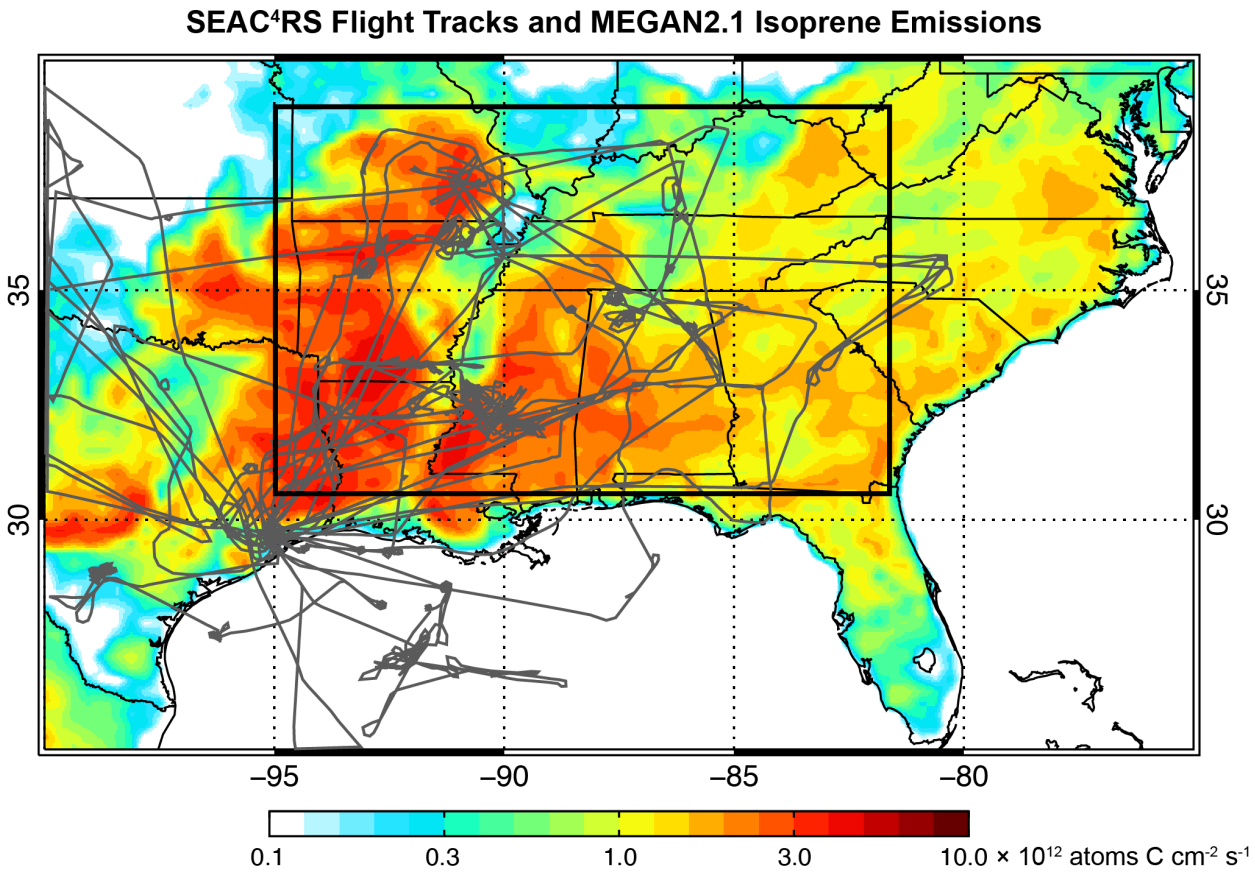

Figure 4.2: Flight tracks of the DC-8 aircraft during SEAC^{4}RS and mean MEGAN2.1 isoprene emissions for August-September 2013. The thick black line delineates the Southeast US domain as defined in this paper [95° W – 81.5° W, 30.5° N – 39° N].

and (4) assessing the ability of CTMs to relate satellite measurements of AOD to surface PM.

4.2 The GEOS-Chem CTM

GEOS-Chem has been used extensively to simulate aerosol concentrations over the US including comparisons to observations [*Park et al., 2003, 2004, 2006; Drury et al., 2010; Heald et al., 2012; Leibensperger et al., 2012a; Walker et al., 2012; L. Zhang et al., 2012; Ford and Heald, 2013*]. Here we use GEOS-Chem version 9-02 (http://geos-chem.org) with detailed

oxidant-aerosol chemistry and the updates described below. Our SEAC^{4}RS simulation for August-October 2013 is driven by Goddard Earth Observing System (GEOS-FP) assimilated meteorological data from the NASA Global Modeling and Assimilation Office (GMAO). The GEOS-FP meteorological data have a native horizontal resolution of 0.25° x 0.3125° with 72 vertical pressure levels and 3 h temporal frequency (1 h for surface variables and mixing depths). We use the native resolution in GEOS-Chem over North America and adjacent oceans [130° - 60° W, 20 - 60° N] to simulate the August 1 – October 31, 2013 period with a 5-minute transport time step. This is nested within a global simulation at 4^o x 5^o horizontal resolution to provide dynamic boundary conditions. The global simulation is initialized on June 1, 2012 with climatological model fields and spun up for 14 months, effectively removing the sensitivity to initial conditions.

GEOS-Chem simulates the mass concentrations of all major aerosol components including sulfate, nitrate, and ammonium [SNA; *Park et al., 2006; L. Zhang et al., 2012*], organic carbon [OC; *Heald et al., 2006a, 2011; Fu et al., 2009*], black carbon [BC; *Q. Wang et al., 2014*], dust in four size bins [*Fairlie et al., 2007*], and sea salt in two size bins [*Jaegle et al., 2011*]. Aerosol chemistry is coupled to HO_x-NO_x-VOC-O_3-BrO_x tropospheric chemistry with recent updates to the isoprene oxidation mechanism as described by *Mao et al.* [2013]. Gas/particle partitioning of SNA aerosol is computed with the ISORROPIA II thermodynamic module [*Fontoukis and Nenes, 2007*], as implemented in GEOS-Chem by *Pye et al.* [2009]. Aerosol wet and dry deposition are described by *H. Liu et al.* [2001] and *L. Zhang et al.* [2001] respectively. OC is the carbon component of OA, and we infer OA from OC by assuming OA/OC mass ratios for different OC sources as given by *Canagaratna et al.* [2015]. Model results are presented below either as OC or OA depending on the measurement to which they are

compared. Measurements from surface networks are as OC while the aircraft measurements are as OA.

Table 1 lists GEOS-Chem emissions in the continental United States (CONUS) for 2013. Values for the Southeast US in August-September are in parentheses. Emissions outside the CONUS are as in *Kim et al.* [2013] and are used in the global simulation to derive the boundary conditions for the nested grid. US anthropogenic emissions are from the EPA National Emissions Inventory for 2010 (NEI08v2). The NEI emissions are mapped over the 0.25^o x 0.3125^o GEOS-Chem grid and scaled to 2013 by the ratio of national annual totals (http://www.epa.gov/ttnchie1/trends/). For BC and SO_2 this would imply 3% and 10% decreases from 2010 to 2013 respectively, but we prescribe instead a 30% decrease for both to better match observed BC concentrations and trends in sulfate wet deposition. Our SO_2 emission adjustment is more consistent with the latest version of the EPA inventory (NEI11v1), which indicates a 34% decline between 2010 and 2013, and the observed trend in surface concentrations from the SEARCH network, which indicates a ~50% decline in the Southeast US over the same years [*Hidy et al., 2014*]. The NEI08 NH_3 emissions are scaled to 2^o x 2.5^o gridded monthly totals from the MASAGE inventory, which provides a good simulation of ammonium wet deposition in the US [*Paulot et al., 2014*].

Open fires have a pervasive influence on OA and BC over the US [*Park et al., 2007*]. During SEAC^{4}RS the Southeast US was affected by both long-range transport of smoke from wildfires in the West [*Peterson et al., 2014; Saide et al., 2015*] and local agricultural fires. We use the Quick Fire Emissions Dataset [QFED2; *Darmenov and da Silva, 2013*], which provides daily open fire emissions at 0.1^o x 0.1^o resolution. Diurnal scale factors peaking at 10-19 local time are applied to the QFED2 daily emissions following recommendations from the Western

Table 4.1: Contiguous US (CONUS) Emissions for 2013[a]

Source	NO_x [Tg N]	CO [Tg]	SO_2 [Tg S]	NH_3 [Tg]	BC [Tg]	OC [Tg]	Isoprene[b] [Tg C]	Monoterpenes[b] [Tg C]
Anthropogenic[c]	2.7 (0.07)	29.8 (0.65)	2.8 (0.14)	3.5[d] (0.11)	0.26 (0.008)	0.58 (0.01)	-	-
Open Fires[e]	0.14 (0.004)	7.9 (0.21)	0.13 (0.002)	0.44 (0.008)	0.19 (0.003)	0.93 (0.01)	-	-
Soil[f]	0.69 (0.03)	-	-	-	-	-	-	-
Vegetation	-	-	-	0.17 (0.002)	-	-	12.2 (2.2)	4.1 (0.5)
Total	3.5 (0.11)	37.7 (0.85)	2.9 (0.14)	4.1 (0.12)	0.45 (0.01)	1.5 (0.02)	12.2 (2.2)	4.1 (0.5)

[a]Annual totals. Emissions in the Southeast US for the two-month SEAC[4]RS period (August-September) are shown in parentheses. The Southeast US domain is as defined in **Figure 4.2**.
[b]Biogenic VOC emissions are from the MEGAN2.1 inventory [*Guenther et al., 2012*] with isoprene emissions decreased by 15%.
[c]Anthropogenic emissions are from the EPA National Emissions Inventory (NEI08v2) scaled nationally to 2013 and with additional adjustments described in the text.
[d]Agricultural ammonia emissions are from the MASAGE inventory on a 2^o x 2.5^o grid [*Paulot et al., 2014*], and are distributed on the 0.25^o x 0.3125^o grid following NEI08v2 as described in the text.
[e]Open fire emissions are from the Quick Fire Emissions Dataset [*Darmenov and da Silva, 2013*], with adjustments described in the text.
[f]Soil and fertilizer NO_x emissions are from the BDSNP algorithm [*Hudman et al., 2012*]. Fertilizer emissions are included in the anthropogenic total.

Regional Air Partnership [*WRAP, 2005*] as in *Saide et al.* [2015]. We inject 35% of fire emissions above the boundary layer between 680 and 450 hPa to account for plume buoyancy [*Turquety et al., 2007; Fischer et al., 2014*].

Biogenic VOC emissions are from the MEGAN2.1 inventory of *Guenther et al.* [2012]. Isoprene emissions are decreased by 15% to better match SEAC[4]RS observations of isoprene and formaldehyde concentrations and surface fluxes [*Travis et al., 2015; Wolfe et al., 2015; Zhu et al., 2015*]. **Figure 4.2** shows the SEAC[4]RS flight tracks superimposed on the distribution of isoprene emissions. Total emissions over the Southeast US (domain outlined in **Figure 4.2**)

during the 2-month SEAC^{4}RS period were 2.2 Tg C for isoprene and 0.5 Tg C for monoterpenes. Monoterpenes did not exceed isoprene emission anywhere.

Sulfate was too low in our initial simulations of the SEAC^{4}RS observations. We addressed this problem by including CIs as additional SO_2 oxidants in the model as previously implemented in GEOS-Chem by *Pierce et al.* [2013]. Oxidation of isoprene and monoterpenes provide a large source of CIs in the Southeast US during the summer; *Sipila et al.* [2014] estimated CI molar yields of 0.58 ± 0.26 from isoprene, 0.15 ± 0.07 from α–pinene and 0.27 ± 0.12 from limonene. *Sarwar et al.* [2014] previously found that simulation of sulfate with the CMAQ CTM compared better with summertime surface observations in the Southeast US when CI + SO_2 reactions were included in the chemical mechanism. Production of sulfate from CI chemistry may be limited by competition for CIs between SO_2 and water vapor and depends on the respective reaction rate constants [*Welz et al., 2012; J. Li et al., 2013; Newland et al., 2014; Sipila et al., 2014; Stone et al., 2014*]. Here we use CI chemistry from the Master Chemical Mechanism [MCMv3.2; *Jenkins et al., 1997; Saunders et al., 2003*] with the CI + SO_2 rate constant from *Welz et al.* [2012] and the CI + H_2O rate constant upper bound from *Stone et al.* [2014], such that the CI + SO_2 pathway dominates. This would not be the case using the standard CI + H_2O rate constant in MCM [*Millet et al., 2015*] or if reaction with the water vapor dimer is important [*Chao et al., 2015*]. Our results thus represent an upper bound on the CI contribution to sulfate production as in *Pierce et al.* [2013].

A number of mechanisms of varying complexity have been proposed to model OA chemistry [*Donahue et al., 2006; Henze et al., 2006; Ervens et al., 2011; Spracklen et al., 2011; Murphy et al., 2012; Barsanti et al., 2013; Hermansson et al., 2014*]. These mechanisms tend to be computationally expensive and appear to have only limited success in reproducing the

observed variability of OA concentrations. Here we use a simple linear approach to simulate five components of OA – anthropogenic POA and SOA, open fire POA and SOA, and biogenic SOA. Anthropogenic and open fire POA emissions are from the NEI08 and QFED2 inventories described above. For anthropogenic and open fire SOA, we adopt the *Hodzic and Jimenez* [2011] empirical parameterization that assumes irreversible condensation of the oxidation products of VOC precursor gases (AVOC and BBVOC respectively). AVOCs and BBVOCs are emitted in proportion to CO, with an emission ratio of 0.069 g AVOC g^{-1} CO [*Hayes et al., 2014*] and 0.013 g BBVOC g^{-1} CO [*Cubison et al., 2011*]. They are both oxidized by OH in the model with a rate constant of 1.25 x 10^{-11} cm^3 $molecule^{-1}$ s^{-1} to generate SOA.

We assume biogenic SOA to be produced with a yield of 3% from isoprene and 5% from monoterpenes, formed at the point of emission. Laboratory studies have shown that different biogenic SOA formation mechanisms operate depending on the NO_x concentration, which determines the fate of the organic peroxy radicals (RO_2) produced from VOC oxidation [*Kroll et al., 2005, 2006; A. Chan et al., 2010; Xu et al., 2014*]. In the high-NO_x regime the RO_2 radicals react with NO, while in the low-NO_x regime they react with HO_2, other RO_2 radicals, or isomerize. During SEAC^{4}RS the two regimes were of comparable importance [*Travis et al., 2015*]. We use four separate tracers in the model to track SOA formed from isoprene and monoterpenes via the high- and low-NO_x pathways. This tracer separation is purely diagnostic as SOA yields are assumed the same in both pathways. The SOA is apportioned to the high- or low-NO_x tracer by the fraction of RO_2 reacting with NO at the point and time of emission.

GEOS-Chem computes the AOD for each aerosol component *i* by summing the optical depths over all vertical model layers $L = [1,\ldots n]$:

$$\text{AOD} = \sum_i \sum_{L=1}^{n} \alpha_i(L) M_i(L) \quad [1]$$

where $\alpha_i(L)$ and $M_i(L)$ are respectively the component mass extinction efficiency (m^2/g) and partial column mass (g/m^2) for level L. The α_i values are pre-calculated for selected wavelengths using a standard Mie scattering algorithm. The algorithm assumes specified aerosol dry size distributions and optical properties from the Global Aerosol Data Set [GADS; *Koepke et al.*, *1997*], with updates by *Drury et al.* [2010] on the basis of summer observations from the ICARTT aircraft campaign over the eastern US. The mass extinction efficiencies are then adjusted for hygroscopic growth as a function of the local relative humidity (RH), following *R. Martin et al.* [2003]. The total AOD is reported here at 550 nm and is the sum of the contributions from all aerosol components.

Comparison of GEOS-FP PBL heights with lidar and ceilometer data from SEAC^{4}RS, SOAS, and DISCOVER-AQ indicates a 30-50% positive bias across the Southeast US in daytime [*Scarino et al., 2015; Millet et al., 2015*]. We decrease the daytime GEOS-FP PBL heights by 40% in our simulation to correct for this bias. During SEAC^{4}RS, PBL heights were measured by the NASA-Langley High Spectral Resolution Lidar [HSRL; *Hair et al., 2008*]. The corrected PBL height is typically within 10% of the HSRL data along the SEAC^{4}RS flight tracks, with a mean daytime value (± 1 standard deviation) of 1690 ± 440 m in the HSRL data and 1530 ± 330 m in the model [*Zhu et al., 2015*].

Several companion papers apply the same GEOS-Chem model configuration described above to other analyses of the SEAC^{4}RS data focused on gas-phase chemistry. These include investigation of the factors controlling ozone in the Southeast US [*Travis et al., 2015*], isoprene chemistry and the formation of organic nitrates [*Fisher et al., 2015*], validation of satellite

HCHO data as constraints on isoprene emissions [*Zhu et al., 2015*], and sensitivity to model grid resolution [*K. Yu et al., 2015*]. These studies include extensive comparisons to the gas-phase observations in SEAC^{4}RS. Our focus here will be on the aerosol observations.

4.3 Surface Aerosol Concentrations

We begin by evaluating the simulation of $PM_{2.5}$ and its components against ground observations. Total $PM_{2.5}$ is measured gravimetrically at 35% RH at a large number of EPA monitoring sites (**Figure 4.3**). In addition, filter-based measurements of $PM_{2.5}$ composition are taken every three days at surface networks including the EPA CSN (25 sites in the study domain marked in **Figure 4.2**, mostly in urban areas), IMPROVE (15 sites, mostly in rural areas), and SEARCH (5 sites, urban and suburban/rural). The networks all provide 24-h average concentrations of the major ions (SNA), carbon species (BC and OC), and dust, though there are differences in protocol [*Edgerton et al., 2005; Hidy et al., 2014; Solomon et al., 2014*], in particular with respect to OC artifact correction. The IMPROVE and SEARCH OC are both blank-corrected but in different ways [*Dillner et al., 2009; Chow et al., 2010*], while CSN OC is uncorrected. We apply a constant 0.3 $\mu g/m^3$ background correction to the CSN OC data as in *Hand et al.* [2012a]. The resulting CSN OC measurements are 44% higher than IMPROVE averaged across the Southeast US. We do not discuss sea-salt concentrations as they make a negligible contribution to $PM_{2.5}$ inland (< 0.1 $\mu g/m^3$ averaged across the EPA networks).

Figure 4.3 shows mean August-September 2013 $PM_{2.5}$ at the EPA sites and compares to GEOS-Chem values. During this time, much of the region approaches or exceeds the annual 12 $\mu g\ m^{-3}$ national ambient air quality standard. Concentrations peak over Arkansas, Louisiana, and

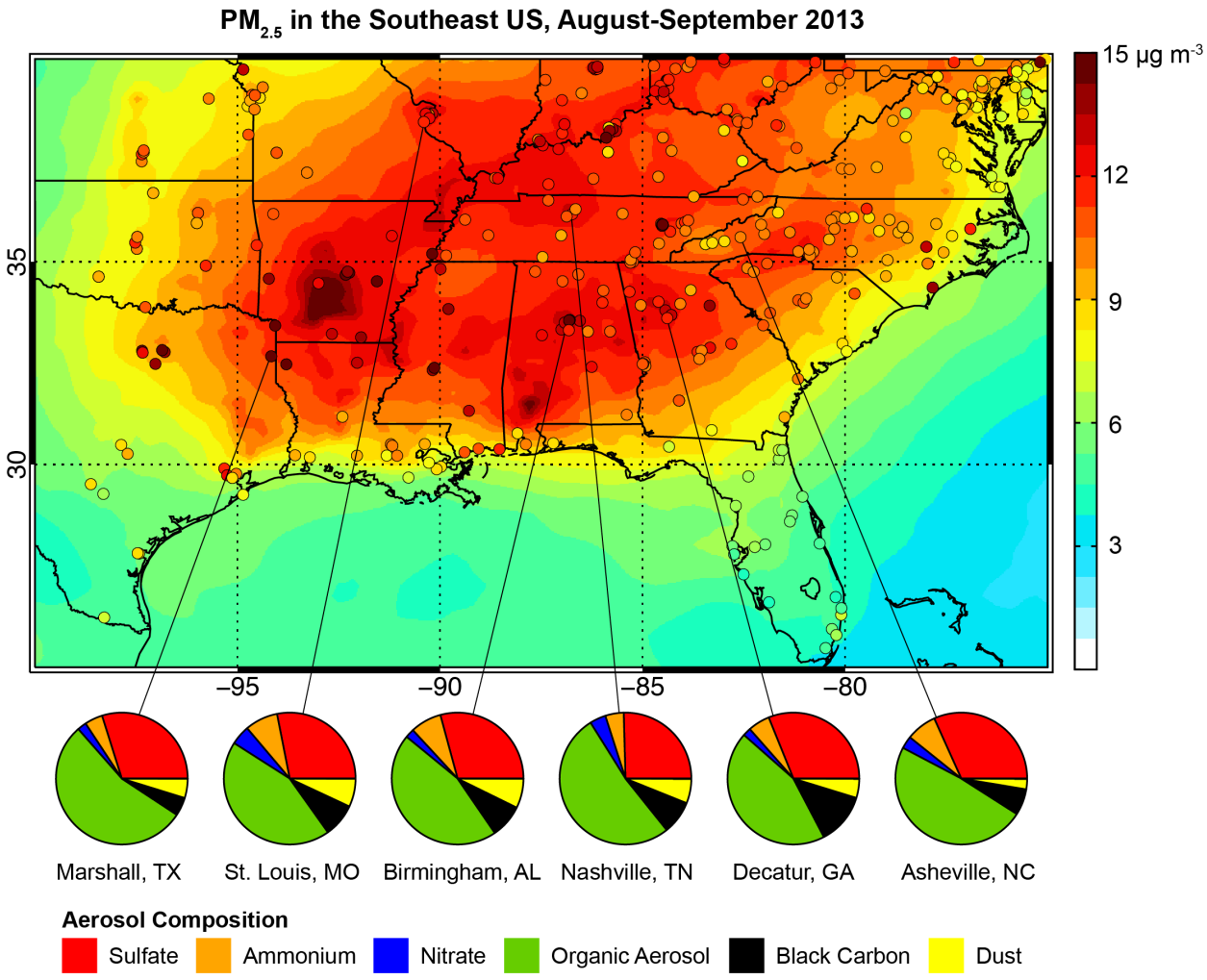

Figure 4.3: Mean $PM_{2.5}$ in the Southeast US in August-September 2013. EPA observations (circles) are compared to GEOS-Chem model values (background). Model values are calculated at 35% relative humidity as per the Federal Reference Method protocol. Observed mean $PM_{2.5}$ speciation by mass is shown in the pie charts for representative CSN sites. Organic aerosol (OA) mass concentrations are derived from measurements of organic carbon (OC) by assuming an OA/OC mass ratio of 1.92 [*Attwood et al., 2014*].

Mississippi, corresponding to the region of maximum isoprene emission in **Figure 4.2**. The spatial distribution and composition of $PM_{2.5}$ is otherwise fairly homogeneous across the Southeast US, reflecting coherent stagnation, mixing, and ventilation of the region [*X. Zhang et al., 2012; Pfister et al., 2015*]. Sulfate accounts on average for 30% of $PM_{2.5}$, while OA accounts for 50%. GEOS-Chem captures the broad features shown in the surface station data with no

significant bias (R = 0.65, normalized mean bias or NMB = -1.4%). The model hotspot in southern Arkansas is due to OA from a combination of biogenic emissions and agricultural fires. As discussed below, agricultural fires make only a small contribution on a regional scale.

The spatial distributions of sulfate and OC concentrations are shown in **Figure 4.4**. The observed and simulated sulfate maxima are shifted to the northeast relative to total $PM_{2.5}$ shown in **Figure 4.3**. GEOS-Chem captures a larger fraction of the observed variability at rural sites (R = 0.78 for IMPROVE) than at urban/suburban sites (R = 0.71 for SEARCH, 0.62 for CSN) as would be expected from the sub-grid scale of urban pollution. The model bias (NMB) is +5% relative to IMPROVE, +10% relative to SEARCH, and +9% relative to CSN. Gas-phase oxidation of SO_2 by CIs contributes 36% of sulfate production over the Southeast US in the model, compared to 42% from in-cloud production (mainly H_2O_2) and 22% from gas-phase oxidation by OH. CIs contribute up to 50% of sulfate formation over Arkansas. Previous studies by *Pierce et al.* [2013] and *Boy et al.* [2013] found similarly large contributions of CIs to sulfate production over forested regions in summer. There is large uncertainty in the CI kinetics, as discussed above. It is possible that the need in GEOS-Chem for a CI pathway to match the sulfate observations could mask an underestimate of aqueous-phase processes that are difficult to constrain.

The observed OC distribution shows a decreasing gradient from southwest to northeast that maps onto the distribution of isoprene emissions shown in **Figure 4.2**. The IMPROVE OC is generally low compared to CSN and SEARCH, as has been noted previously [*Ford and Heald, 2013; Attwood et al., 2014*]. GEOS-Chem reproduces the broad features of the observed OC distribution with moderate skill in capturing the variability (R = 0.64 for IMPROVE, 0.62 for SEARCH, 0.61 for CSN). Model OC is biased high with a NMB of +66% for IMPROVE, +29%

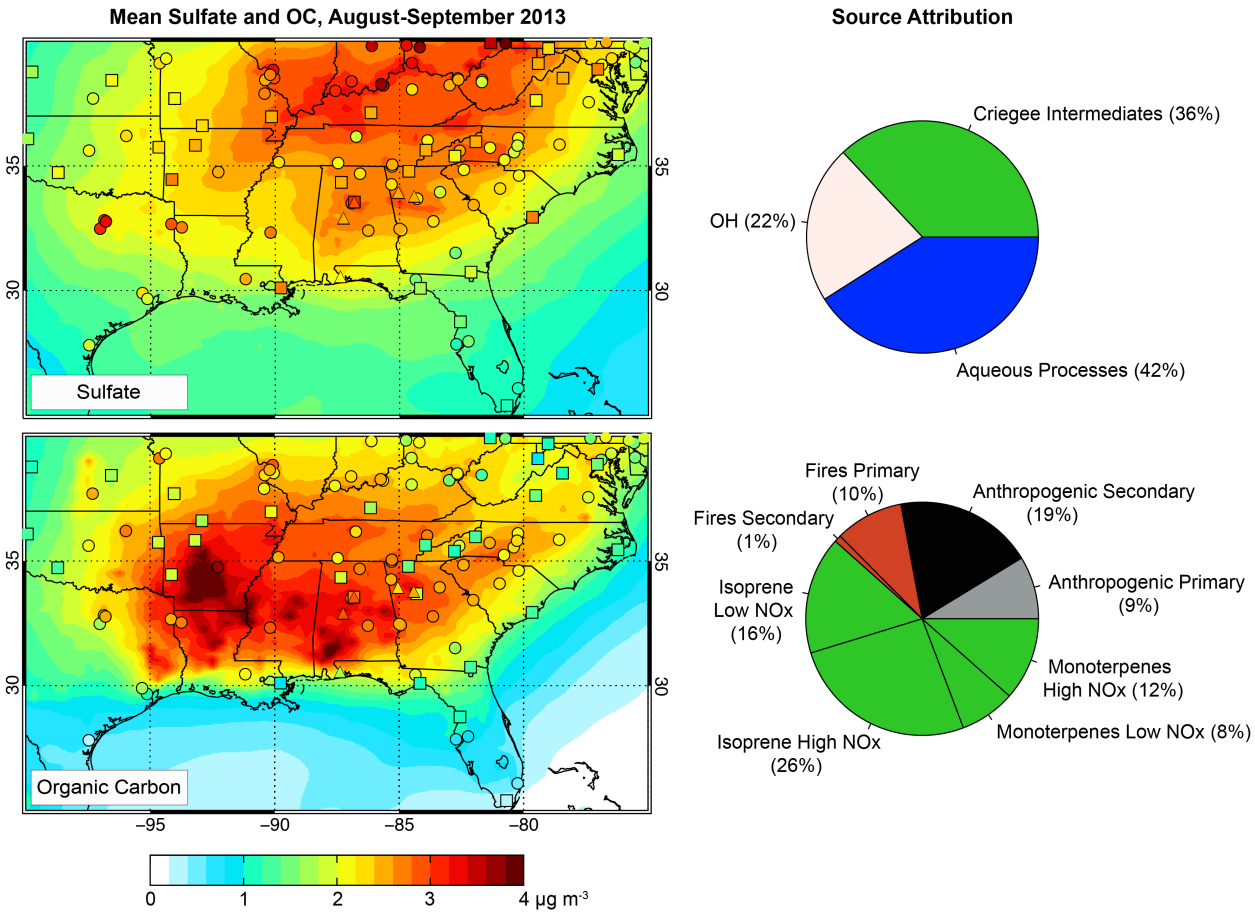

Figure 4.4: Mean sulfate (top) and OC (bottom) surface air concentrations in the Southeast US in August-September 2013. Network observations from CSN (circles), IMPROVE (squares), and SEARCH (triangles) are compared to GEOS-Chem model values (background). OC measurements are artifact corrected as described in the text. Source attribution for sulfate and OC is shown at right as averages for the Southeast US domain defined in **Figure 4.2**. For sulfate, source attribution is by SO_2 oxidant. For OC, source attribution is primary or secondary, by source type, and by NO_x regime.

for SEARCH, and +14% for CSN. The range of NMBs for the different networks could reflect differences in measurement protocols, as described above. We discuss this further in the next Section in the context of the aircraft data.

Source attribution of OC in the model (**Figure 4.4**) suggests a dominance of biogenic sources. Isoprene alone contributes 42% of the regional OC burden. This is in contrast with previous work by *Barsanti et al.* [2013], who fitted chamber observations to a model mechanism

and found monoterpenes to be as or more important than isoprene as a source of OC in the Southeast US (particularly under low-NO_x conditions). SEAC^{4}RS observations of IEPOX-SOA (a tracer of SOA formation from isoprene by the low-NO_x pathway) suggest that if anything the model underestimates the SOA yield from isoprene under those conditions [*W. Hu et al., 2015; Campuzano-Jost et al., 2015*].

Anthropogenic sources in the model contribute 28% to regional OC, roughly evenly distributed across the region. Open fires contribute 11%, mainly from agricultural fires in Arkansas and Missouri. Influence from western US fires was significant in the free troposphere (see Section 4) but did not significantly extend down to the surface.

When all of the components are taken together, we find that 81% of the surface OC in the Southeast US is secondary in origin. This is at the high end of the 30-69% range of previous literature estimates for the region [*Lim and Turpin, 2002; S. Yu et al., 2004; Kleindienst et al., 2007; Blanchard et al., 2008*] and likely reflects the decreasing trend in anthropogenic emissions (**Figure 4.1**). Assuming fossil fractions of 50% and 70% for anthropogenic primary and secondary OC respectively [*Zotter et al., 2014*], we estimate that 18% of the total OC burden is derived from fossil fuel use. This is consistent with an 18% fossil fraction from radiocarbon measurements made on filter samples collected in Alabama during SOAS [*Edgerton et al., 2014*].

4.4 Aerosol Vertical Profile

We now examine the aerosol vertical distribution measured by aircraft, and simulated by GEOS-Chem, for consistency with the surface data and to constrain the relationship between

AOD and surface PM. The NASA DC-8 aircraft made 18 flights based out of the Southeast US during SEAC^{4}RS (**Figure 4.2**). Aerosol mass composition was measured by an Aerosol Mass Spectrometer (AMS) for SNA and OA [*Canagaratna et al., 2007*] and by the NOAA humidified dual single-particle soot photometer for BC [HDSP2; *Schwarz et al., 2008*]. Dust concentrations were measured by the SAGA instrument [*Dibb et al., 2003*], but *Drury et al.* [2010] previously found in ICARTT that these were considerably higher than the values measured by surface networks or simulated in GEOS-Chem. We find the same here, and choose to infer dust concentrations in SEAC^{4}RS from single-particle size and chemical composition measurements made by the PALMS laser mass spectrometer [*Thomson et al., 2000*]. The PALMS data provide the size-resolved number fraction of dust-containing particles, which is then multiplied by the measured aerosol volume distribution from the LARGE instrument [*Thornhill et al., 2008; Chen et al., 2011*] and an assumed density of 2.5 g cm^{-3}. For all comparisons presented below, GEOS-Chem is sampled along the aircraft flight tracks at the time of observation.

Figure 4.5 shows the median sulfate, OA, and dust vertical profiles over the Southeast US during SEAC^{4}RS. Also shown are the median concentrations from the surface networks. For sulfate, the model underestimates the aircraft observations by 20% below 5 km but overestimates the surface observations by +5-10% as discussed in Section 3; these small inconsistent biases may not be significant. The shape of the vertical profile is well simulated. Concentrations are highest near the surface and drop rapidly with altitude, but there is significant mass loading in the lower free troposphere. 40% of the observed sulfate column mass lies above 2 km and this is well simulated by the model (36%). Analysis of SENEX and SEAC^{4}RS vertical profiles by *Wagner et al.* [2015] suggests that most of this free tropospheric sulfate is ventilated from the PBL rather than being produced within the free troposphere from ventilated SO_2. GEOS-Chem

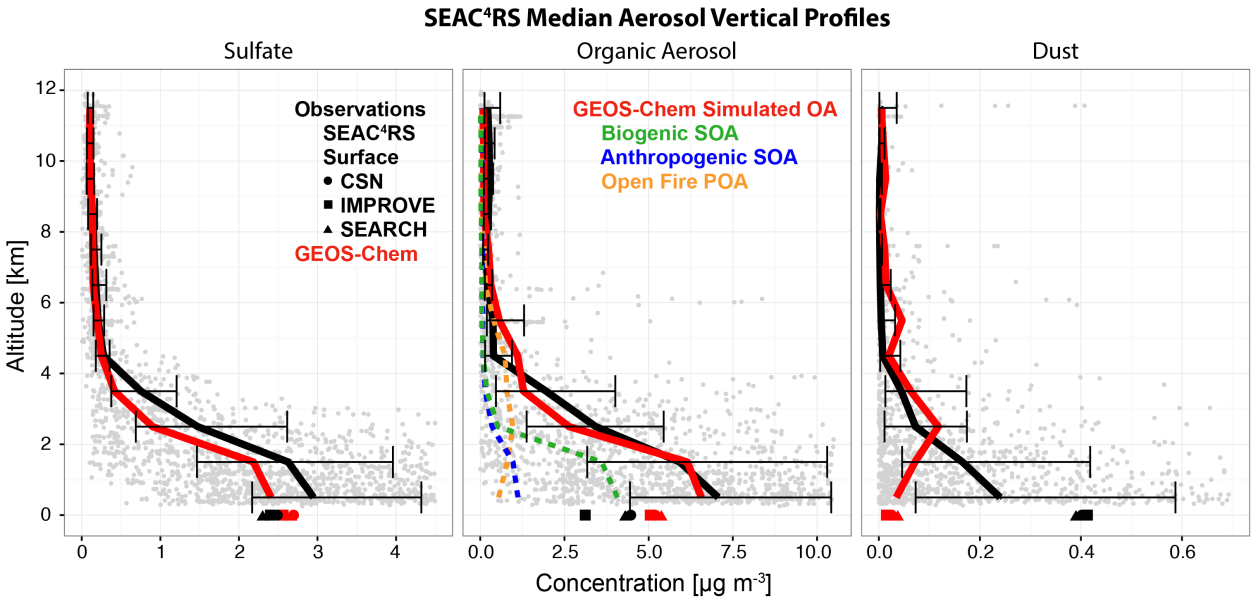

Figure 4.5: Median vertical profiles of aerosol concentrations over the Southeast US (**Figure 4.2**) during the SEAC^{4}RS aircraft campaign (August-September 2013). Observed and simulated profiles of sulfate (left), OA (center), and dust (right) in 1-km bins are shown with the corresponding median surface network observations. OC from the surface networks is converted to OA using an OA/OC ratio of 1.92 as in *Attwood et al.* [2014]. The contributions of anthropogenic SOA, biogenic SOA, and open fire POA to total simulated OA are also shown. The individual observations are shown in gray and the horizontal bars denote the 25th and 75th percentiles of the observations. The choice of scale truncates some very large individual observations.

shows moderate skill in explaining the variability in the aircraft sulfate data (R = 0.81 for all observations in the Southeast US, R = 0.63 below 2 km, R = 0.74 above 2 km).

Similarly to sulfate, OA measured from aircraft peaks at the surface and decreases rapidly with height (**Figure 4.5**). The aircraft OA below 1 km is about twice higher than measured at the surface networks. Half of this discrepancy can be explained by differences in the air sampled, as shown in **Figure 4.5** by the GEOS-Chem simulation sampled along the flight tracks vs. at the surface networks. The remaining discrepancy may reflect differences in instrumentation. The GEOS-Chem simulation matches closely the aircraft observations, while being 14-66% higher than the surface networks as reported above. The vertical distribution is similar to that of sulfate,

with 35% of the total OA column above 2 km both in the model and in the observations. The GEOS-Chem source attribution, also shown in **Figure 4.5**, indicates that open fires contribute 50% of OA in the free troposphere. This fire influence is seen in the observations as occasional plumes of OA up to 6-7 km altitude (individual gray dots in **Figure 4.5**). Fire plumes can be problematic for interpreting the AOD/PM relationship for individual scenes but much less so in a temporal average where the influence on the column is small. Simulating fire influence successfully in the model does require buoyant injection of fire emissions in the free troposphere, as noted in previous studies [*Turquety et al., 2007; Fischer et al., 2014*].

Comparison of GEOS-Chem to the individual OA observations along the aircraft flight tracks shows good simulation of the variability (R = 0.82 for all observations, R = 0.71 below 2 km, R = 0.68 above 2 km). This is despite (or maybe because of) our use of a very simple parameterization for the OA source. The successful GEOS-Chem simulation of the OA vertical profile argues against a large source from aqueous-phase cloud processing associated with the frequent shallow cumulus convection encountered during SEAC^{4}RS. This is supported by the work of *Wagner et al.* [2015], who found little OA enhancement in air masses processed in this cumulus wet convection.

Dust made only a minor contribution to total aerosol mass in the Southeast US during SEAC^{4}RS, accounting for less than 10% of observed surface $PM_{2.5}$ (**Figure 4.3**). The PBL dust concentrations inferred from PALMS observations are roughly consistent with the surface data but the model is much lower (**Figure 4.5**). This reflects a southern bias in the model transport of Saharan dust [*Fairlie et al., 2007*], but is of little consequence for the simulation of $PM_{2.5}$ or the AOD/PM relationship over the Southeast US. **Figure 4.5** shows few free tropospheric plumes in the SEAC^{4}RS observations. This is consistent with the dust climatology compiled from CALIOP

data by *D. Liu et al.* [2008], which shows few elevated dust layers over the Southeast US during the summer that could obfuscate the relationship between surface PM and AOD.

Figure 4.6 compiles the median observed and simulated vertical profiles of aerosol concentrations and composition during SEAC^{4}RS. OA and sulfate dominate at all altitudes. Ammonium is associated with sulfate as discussed in the next Section. OA accounts for most of $PM_{2.5}$ below 1 km, with a mass fraction F_{OA} = [OA]/[$PM_{2.5}$] of 0.66 g g^{-1} (0.65 in GEOS-Chem). **Figure 4.1** shows a lower F_{OA} in the IMPROVE surface observations, increasing from 0.31 g g^{-1} to 0.41 g g^{-1} between 2003 and 2013. As pointed out above, the difference between the aircraft observations and IMPROVE may reflect in part a difference in air masses sampled and in part a difference in OA instrumentation or artifact correction. The aircraft data indicate most of the aerosol mass to be OA at all altitudes. The aerosol column is mostly in the PBL, but 40% is above 2 km and 10% above 5 km (**Figure 4.6**, right panel). GEOS-Chem reproduces closely the observed vertical distribution of aerosol mass, and this is an important result for application of the model to derive the AOD/PM relationship.

4.5 Sulfate Aerosol Neutralization

Neutralization of sulfate aerosol by ammonia has important implications for the aerosol phase and hygroscopicity, for the formation of aerosol nitrate [*S. Martin et al., 2004; J. Wang et al., 2008*], and for the formation of SOA [*Froyd et al., 2010; Eddingsaas, et al., 2012; Budisulistiorini et al., 2013*]. **Figure 4.6** shows ammonium to be the third most important aerosol component by mass in the Southeast US in summer after OA and sulfate. Summertime ammonium concentrations have declined at approximately the same rate as sulfate from 2003 to

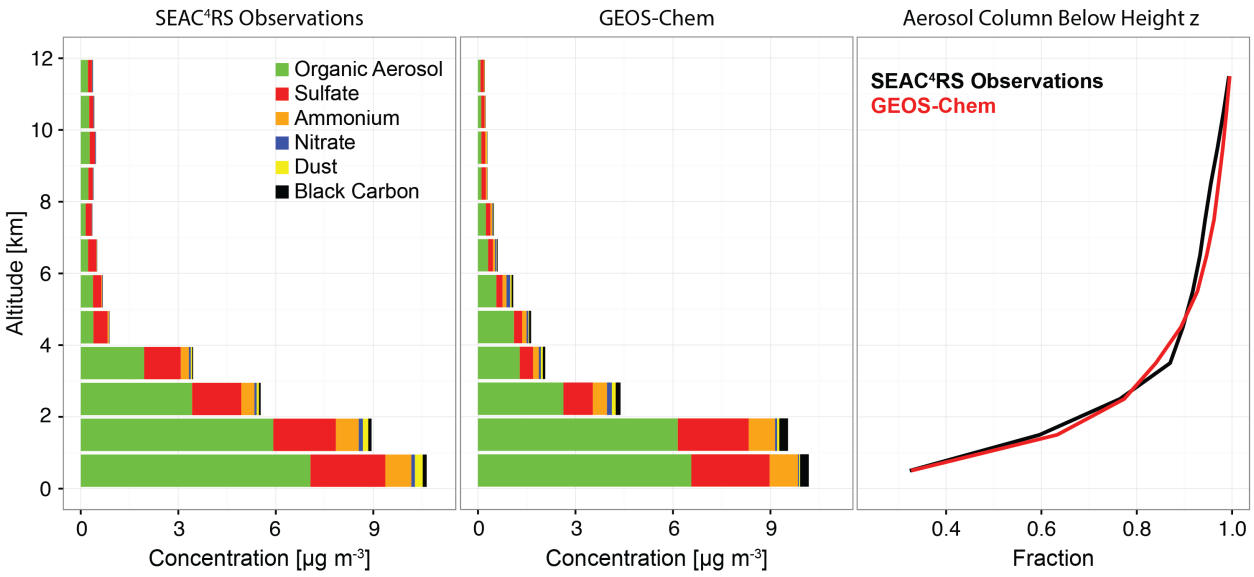

Figure 4.6: Median vertical profiles of aerosol concentration and composition over the Southeast US during SEAC^{4}RS (August-September 2013). Observations from the DC-8 aircraft (left) are compared to GEOS-Chem values sampled at the aircraft times and locations (center). Also shown is the observed and simulated fraction of the total aerosol mass column below a given height (right). The Southeast US domain is as defined in **Figure 4.2**.

2013 (**Figure 4.1** and *Blanchard et al.* [2013]). However, we find no significant trend over that time in ammonium wet deposition fluxes over the Southeast US (National Atmospheric Deposition Program*, 2015*), in contrast to a ~50% decline in sulfate wet deposition. This implies that ammonia emissions have not decreased but the partitioning into the aerosol has.

One would expect ammonium aerosol trends to follow those of sulfate if the aerosol was neutralized, so that partitioning of ammonia into the aerosol is limited by the supply of sulfate. Assuming that the SNA aerosol is externally mixed from other ionic aerosol components such as dust, the degree of neutralization can be computed from the neutralization fraction $f = [NH_4^+]/(2[SO_4^{2-}] + [NO_3^-])$ where concentrations are molar. $f = 1$ corresponds to fully neutralized aerosol, $f < 1$ to acidic aerosol. **Figure 4.7** shows this neutralization fraction in the observations and the model. The sulfate aerosol is fully neutralized in the model but is consistently acidic in the observations, with median neutralization fractions of 0.55 mol mol^{-1} in the CSN data and 0.68

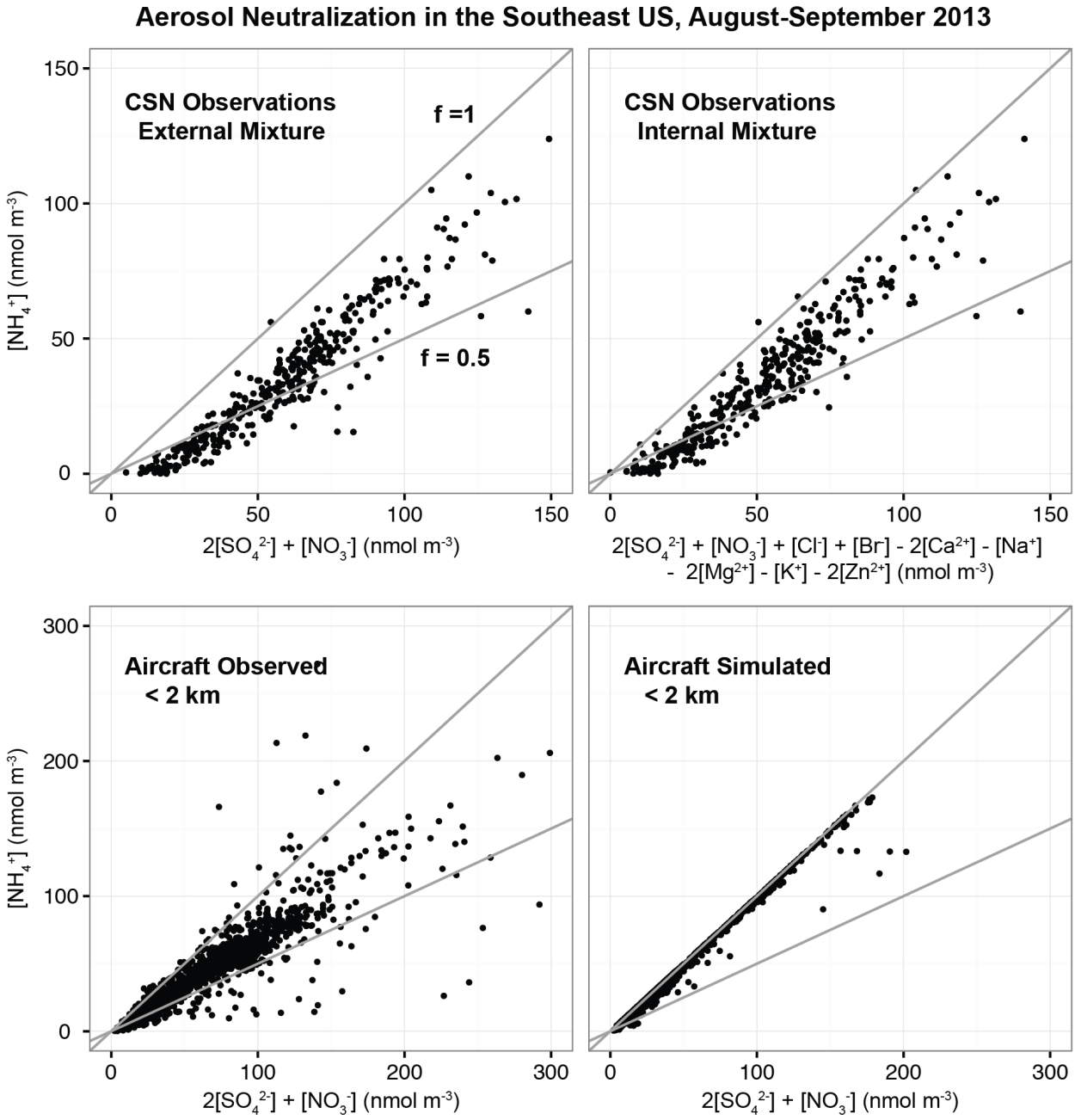

Figure 4.7: Sulfate aerosol neutralization fraction in the Southeast US (August-September 2013). The neutralization fraction for an external sulfate-nitrate-ammonium (SNA) mixture is given by the $f = [NH_4^+]$ vs. $2[SO_4^{2-}] + [NO_3^-]$ molar relationship, and this can be adjusted for an internal mixture by considering additional ions. The top panels show observations from the CSN network assuming an external (left) or internal (right) mixture; there is little difference between the two because the concentrations of additional ions are usually small. The bottom panels show the SEAC^{4}RS aircraft observations below 2 km and corresponding GEOS-Chem values. Also shown are the lines corresponding to full neutralization of the sulfate aerosol ($f = 1$) and to highly acidic NH_4HSO_4 conditions ($f = 0.5$).

mol mol^{-1} in the SEAC^{4}RS data below 2 km. The CSN data include full ionic analysis and we examined whether internal mixing of SNA aerosol with other ions could affect the neutralization fraction. The top right panel of **Figure 4.7** shows that it does not, reflecting the low concentrations of these other ions. Aside from discrepancy between model and observations, one would expect ammonia at thermodynamic equilibrium to be fully partitioned into acidic aerosol, so that ammonium in the observations should not respond to a decrease in sulfate. The observed ammonium decrease over the 2003-2013 period thus poses a puzzle.

A possible explanation is that ammonia uptake by acidic aerosol may be inhibited by competing uptake of organic gases. This has been demonstrated in a laboratory study by *Liggio et al.* [2011], who show that the time constant for ammonia to be taken up by acid sulfate aerosol increases with the ratio of organic gases to sulfate and may be hours to days. We tested this hypothesis by examining the relationship between the model neutralization bias (difference between simulated and observed *f*) and the OA concentration in the aircraft observations below 1 km, assuming sulfate and OA to be mixed. We find a significant correlation (R = -0.33), as shown in **Figure 4.8**, which provides some support for organic-driven inhibition of ammonia uptake by acid sulfate aerosol.

The full neutralization of sulfate aerosol in the model, in contrast to observations, leads to bias in the simulated aerosol phase and hygroscopicity for relating AOD to PM. Calculations by *J. Wang et al.* [2008] for ammonium-sulfate particles of different compositions show a 10-20% sensitivity of the mass extinction efficiency to the neutralization fraction, with the effect changing sign depending on composition and RH. An additional effect of full neutralization in the model would be to allow formation of ammonium nitrate aerosol, but nitrate aerosol is negligibly small in the model as it is in the observations (**Figure 4.6**). At the high temperatures

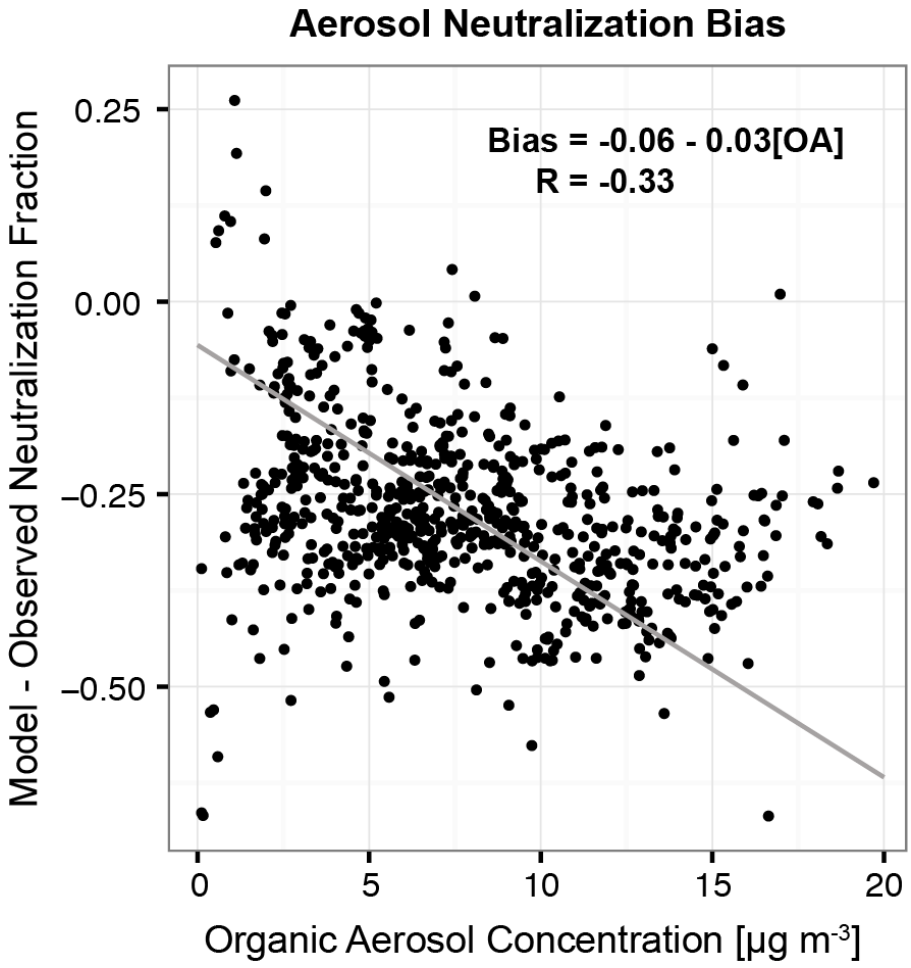

Figure 4.8: Correlation of the sulfate neutralization bias in GEOS-Chem with organic aerosol (OA) concentrations. The ordinate shows the difference between simulated and observed neutralization fraction $f = [NH_4^+]/(2[SO_4^{2-}] + [NO_3^-])$ along the SEAC^{4}RS flight tracks in the Southeast US below 1 km. OA is from the aircraft observations. The regression coefficients shown inset are calculated using reduced-major-axis regression.

over the Southeast US in the summer, we find in the model that the product of HNO_3 and NH_3 partial pressures is generally below the equilibrium constant for formation of nitrate aerosol. By contrast, surface network observations in winter show nitrate to be a large component of surface $PM_{2.5}$ [**Figure 4.1**; *Hand et al., 2012b; Ford and Heald, 2013*], reflecting both lower temperatures and the lower levels of sulfate and OA.

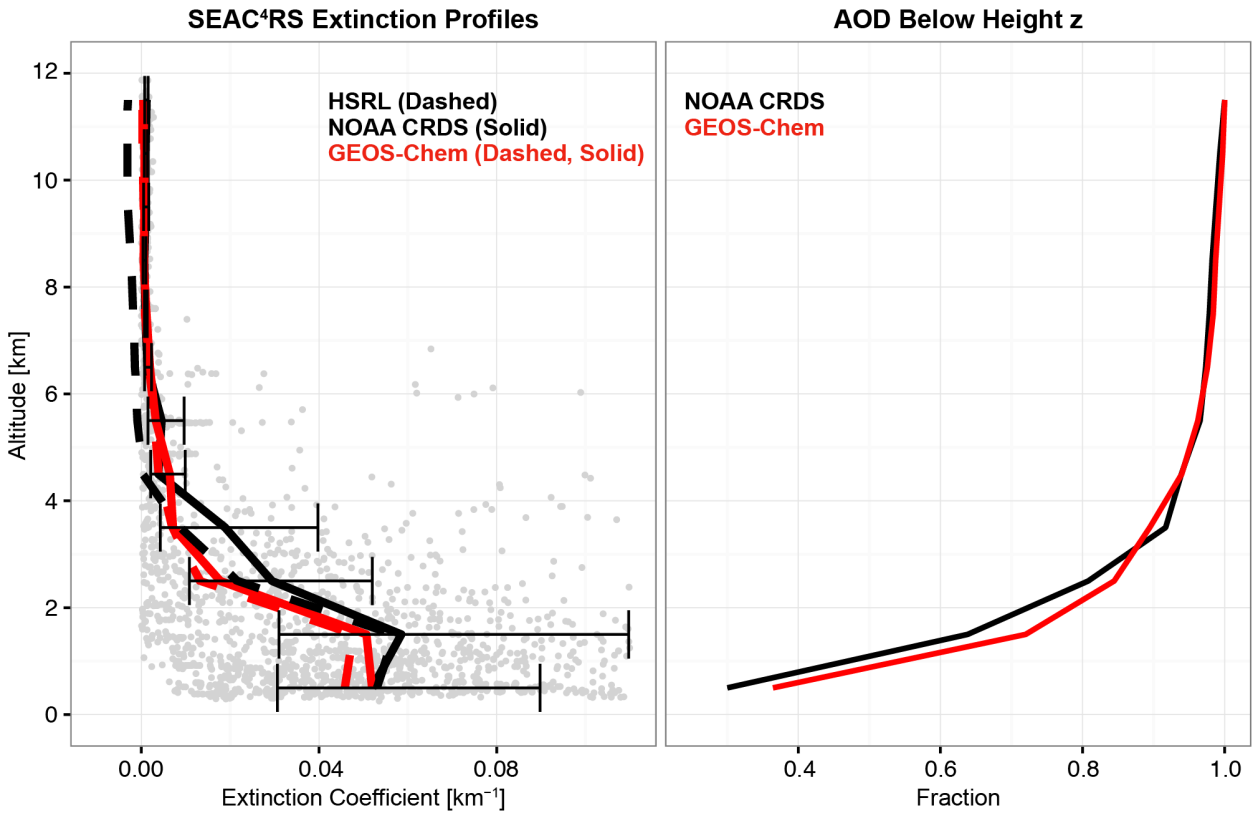

Figure 4.9: Median vertical profiles of aerosol extinction coefficients (532 nm) over the Southeast US during SEAC^{4}RS. The left panel shows independent observations from the NASA HSRL and NOAA CRDS instruments, with GEOS-Chem sampled at the times and locations of the available instrument data. The individual CRDS observations are shown in gray and the horizontal bars denote the 25th and 75th percentiles of the CRDS observations for each 1 km bin. The choice of scale truncates some very large individual observations. The right panel shows the observed (CRDS) and simulated fraction of the total AOD below a given height (right). The Southeast US domain is as defined in **Figure 4.2**.

4.6 Aerosol Extinction and Optical Depth

We turn next to light extinction measurements made onboard the DC-8 to better understand the relationship between the vertical profiles of aerosol mass (Section 4) and AOD. Aerosol extinction coefficients were measured on the SEAC^{4}RS aircraft remotely by the NASA HSRL and locally by the NOAA cavity ringdown spectrometer [CRDS; *Langridge et al., 2011*]. **Figure 4.9** compares the two measurements with the GEOS-Chem simulation. Though the two

instruments sampled different regions of the atmosphere at any given time, the mission median profiles are similar. The exception is between 2 and 4 km where the CRDS extinction coefficient is higher, presumably when the DC-8 was near clouds and the HSRL does not retrieve data. The shapes of the vertical extinction profiles are consistent with aerosol mass (**Figure 4.6**). The fraction of total column extinction due to aerosol below 2 km is 78% for the HSRL data (80% in GEOS-Chem when sampled at the observation times) and 64% for the CRDS data (69% in GEOS-Chem). The atmosphere below 2 km contributes more to total aerosol extinction than to aerosol mass (60%, see Section 4) because of higher RH and hence hygroscopic growth of particles. Almost all of the column extinction is below 5 km (94% for the CRDS and 93% for GEOS-Chem). Integrated up to the ceiling of the DC-8 aircraft, the median AODs from HSRL and the CRDS are 0.14 and 0.17 respectively (0.12 and 0.15 for GEOS-Chem).

Figure 4.10 shows maps of the mean AOD over the Southeast US in August-September 2013 as measured by AERONET, MISR, MODIS on the Aqua satellite, and simulated by GEOS-Chem. The model is sampled at the local satellite overpass times (1030 for MISR and 1330 for MODIS). We use the Version 31 Level 3 product from MISR (gridded averages at 0.5^o x 0.5^o resolution) and the Collection 6 Level 3 product from MODIS (gridded averages at 1^o x 1^o resolution). We exclude MODIS observations with cloud fraction greater than 0.5 or AOD greater than 1.5 to account for cloud contamination and sensor saturation as in *Ford and Heald* [2013]. We use the Level 2 cloud-filtered daytime average AERONET observations, which can be viewed as ground truth.

Comparison of daily collocated MODIS and MISR retrievals with AERONET observations shows high correlation and low bias (statistics inset in **Figure 4.10**). MODIS shows a broad maximum over the Southeast US that corresponds well with observed $PM_{2.5}$ in **Figure**

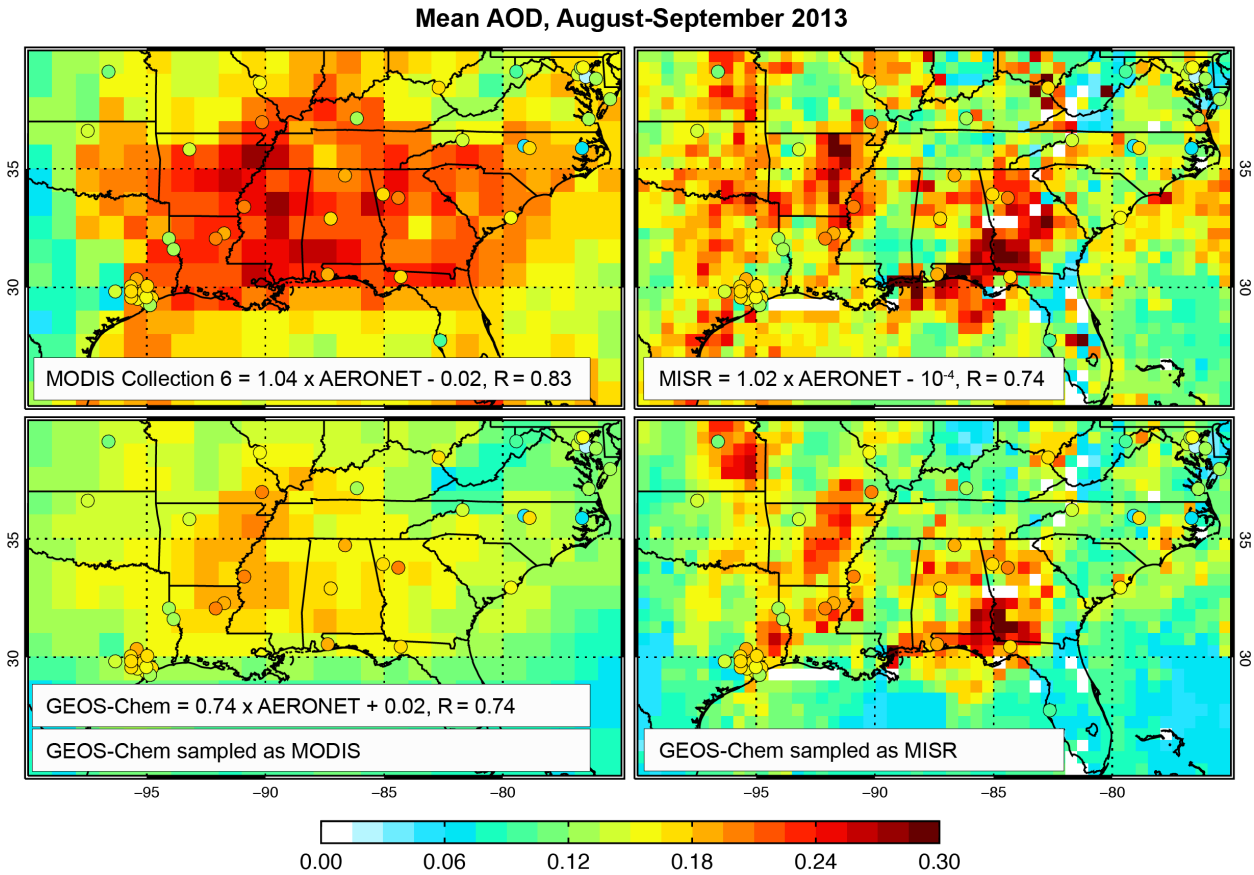

Figure 4.10: Mean aerosol optical depths (AODs) over the Southeast US during SEAC^{4}RS (August-September 2013). AERONET data are shown as circles and are the same in all panels. The top panels show MODIS and MISR satellite observations with comparison statistics to AERONET (correlation coefficients, reduced-major-axis regression lines). The bottom panels show GEOS-Chem model values sampled at the same locations and times as the satellite retrievals. The noise in the MISR panels reflects infrequent sampling (9-day return time, compared to 1-day for MODIS).

4.3. There is greater heterogeneity in the MISR average due to sparse sampling. GEOS-Chem captures the spatial pattern of the regional AOD enhancement when sampled with the different retrievals and underestimates the magnitude by 16% (NMB relative to AERONET), consistent with the underestimate of the aircraft aerosol extinction data.

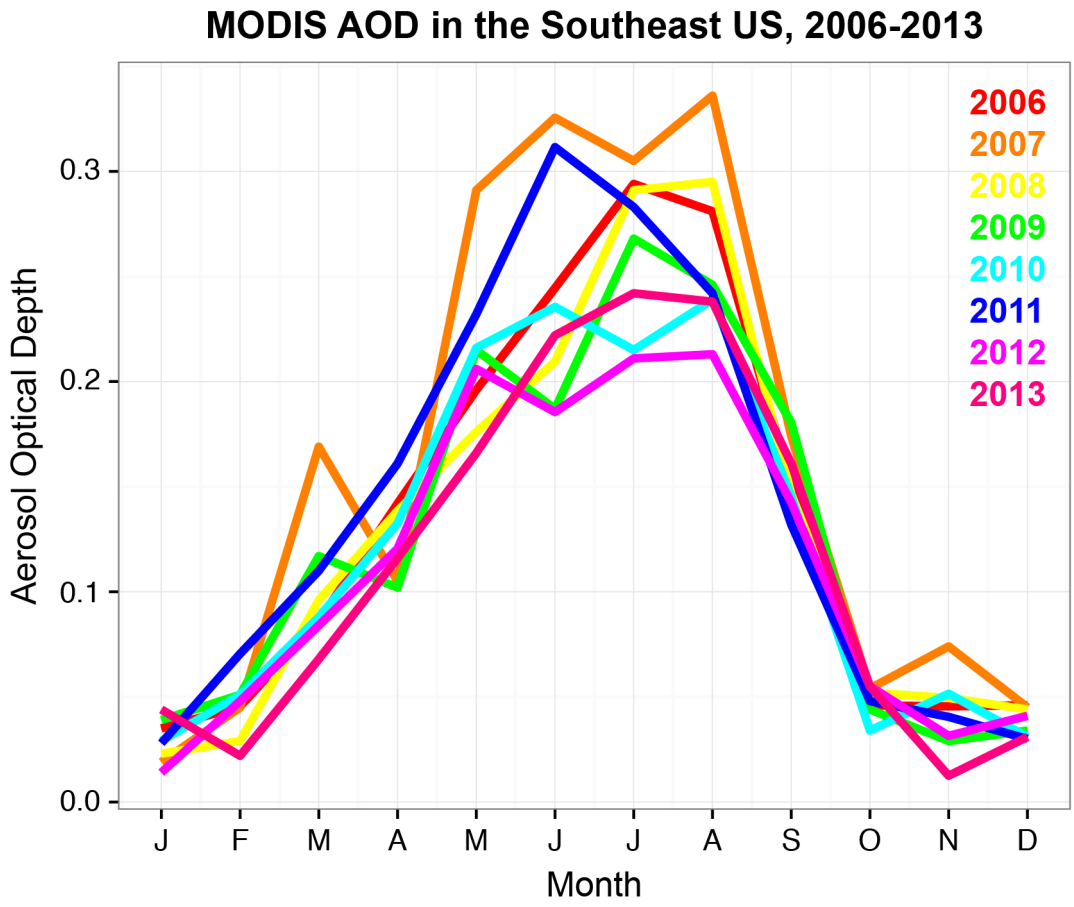

Figure 4.11: Seasonal variation of MODIS AOD over the Southeast US for 2006-2013. The Southeast US domain is as defined in **Figure 4.2**.

4.7 The Aerosol Seasonal Cycle

As pointed out in the Introduction, there has been considerable interest in interpreting the aerosol seasonal cycle over the Southeast US and the difference in seasonal amplitude between AOD and surface $PM_{2.5}$ [*Goldstein et al. 2009, Ford and Heald, 2013*]. **Figure 4.11** shows MODIS monthly average AOD over the Southeast US for 2006-2013. The observed AOD in 2013 shows a seasonal cycle consistent with previous years. There has been a general decline in the seasonal amplitude over 2006-2013 driven by the summertime decrease, with 2011 being anomalous because of large fires [*NOAA, 2011*]. The same long-term decrease and 2011

anomaly are seen in the surface $PM_{2.5}$ data (**Figure 4.1**). Examination of **Figure 4.11** reveals that the entirety of the seasonal decrease from summer to winter takes place as a sharp transition in the August-October window, in all years.

We analyzed the causes of this August-October transition using the GEOS-Chem simulation of the SEAC^{4}RS period. **Figure 4.12** (top panel) shows timeseries of daily median AOD from AERONET, GEOS-Chem sampled at the times and locations of the AERONET observations, and MODIS over the Southeast US. The difference between AERONET and MODIS can be explained by differences in sampling (they otherwise correspond well with each other, see Section 6). Observations through early September show large oscillations with a ~7-10 day period driven by frontal passages. These are well reproduced by the model. The observed AODs then fall sharply in mid-September and again this is well reproduced by GEOS-Chem. The successful simulation of the August-October seasonal transition implies that we can use the model to understand this transition. **Figure 4.12** also shows the sulfate and OA contributions to GEOS-Chem AOD. Sulfate aerosol contributes as much to column light extinction as OA, despite lower concentrations, due to its higher mass extinction efficiency. Both the sulfate and OA contributions to AOD fall during the seasonal transition.

We find that the sharp drops in sulfate and OA concentrations over August-October are due to two common factors. The first factor is a decline in isoprene and monoterpene emissions due to cooler surface temperatures and leaf senescence (panel B of **Figure 4.12**). As shown in **Figure 4.4**, these emissions account for most of OA in summer. The reduction in biogenic emissions also affects sulfate concentrations through the diminished production of CIs.

The second factor is a transition in the photochemical regime. *Kleinman* [1991] and *Jacob et al.* [1995] found that the eastern US undergoes a seasonal transition from NO_x-limited

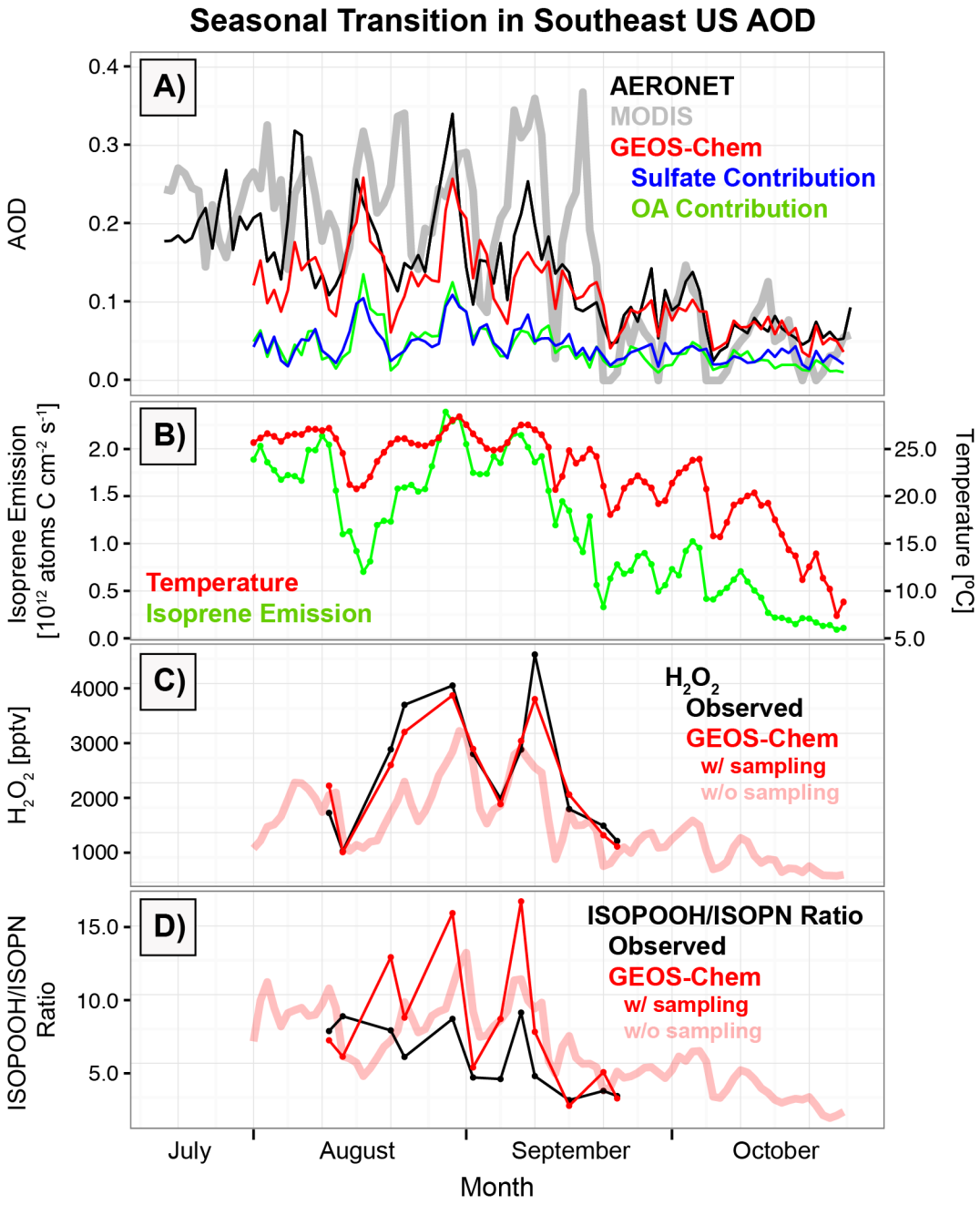

Figure 4.12: Seasonal transition of aerosol optical depth (AOD) and related variables over the Southeast US (August-October). (A) AODs measured by MODIS and AERONET, and GEOS-Chem values sampled at AERONET times and locations with contributions from sulfate and OA. (B) 24-h average MEGAN2.1 isoprene emissions and GEOS-FP surface temperatures. (C) H_2O_2 concentrations measured from the aircraft below 1 km altitude and simulated by GEOS-Chem sampled at the times and locations of the observations. Median values are shown for each flight over the Southeast US. GEOS-Chem H_2O_2 concentrations averaged over the entire region (i.e. without sampling) are shown separately and extend into October. (D) Same as (C) but for the ratio of isoprene peroxides (ISOPOOH) to isoprene nitrates (ISOPN). The Southeast US domain is as defined in **Figure 4.2**.

to NO_x-saturated conditions in September, driven by rapid decline in the UV radiation needed to produce hydrogen oxide (HO_x) radicals. This titrates H_2O_2 production and suppresses corresponding sulfate formation. H_2O_2 concentrations measured from the aircraft and simulated by GEOS-Chem illustrate this seasonal transition (panel C of **Figure 4.12**), with additional low events in August-September associated with rain (scavenging H_2O_2).

The seasonal transition in photochemical regime also involves a shift from low-NO_x to high-NO_x conditions in the fate of the RO_2 radicals produced from isoprene and monoterpene oxidation. This would affect the resulting SOA yield [*Marais et al., 2015*] but is not represented in GEOS-Chem. The bottom panel of **Figure 4.12** shows the ratio of isoprene hydroperoxides (ISOPOOH) to isoprene nitrate (ISOPN) concentrations measured in the PBL during SEAC^{4}RS by the Caltech CIMS [*Crounse et al., 2006; St. Clair et al., 2010*] and simulated by GEOS-Chem. ISOPOOH is formed under low-NO_x conditions, while ISOPN is formed under high-NO_x conditions. Both observations and the model show a decline in the ISOPOOH/ISOPN concentration ratio over the course of SEAC^{4}RS, with the model showing extended decline into October. If the SOA yield is higher under low-NO_x conditions [*Kroll et al., 2005, 2006; Xu et al. 2014*] then this would also contribute to the seasonal decline in OA.

In sharp contrast to AOD, surface $PM_{2.5}$ in the Southeast US shows no significant seasonality in 2013 (**Figure 4.13**, top panel). The lack of a seasonal cycle can be explained by taking into account the seasonal variation in PBL height (**Figure 4.13**, middle panel). The product of surface $PM_{2.5}$ and PBL height, measuring the PBL contribution to the AOD (assuming a constant mass extinction efficiency), has a seasonal variation similar to the AOD measured from space and half the amplitude (**Figure 4.13**, bottom panel). Thus surface $PM_{2.5}$ seasonality is damped by PBL height, while AOD seasonality is more a measure of aerosol sources. We

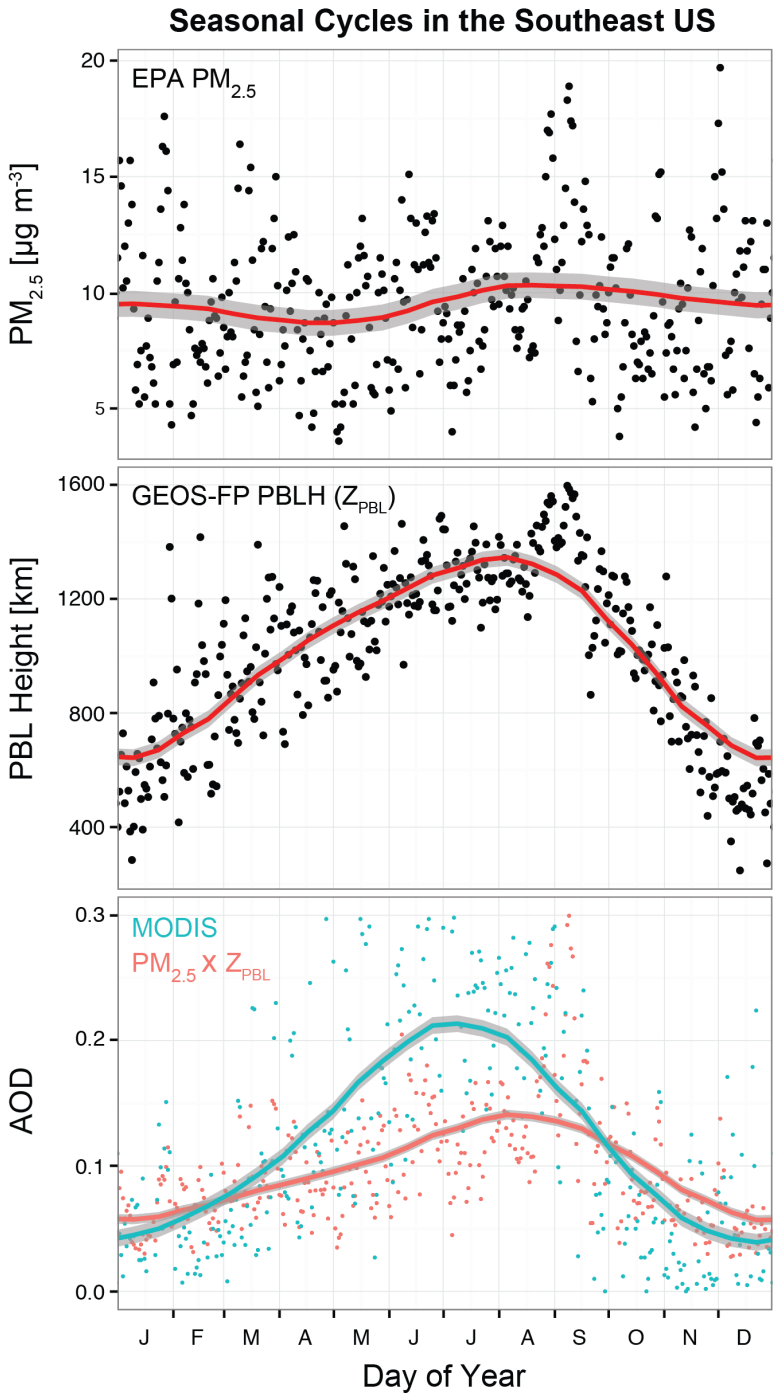

Figure 4.13: Seasonal aerosol cycle in the Southeast US in 2013. (Top) Daily mean EPA $PM_{2.5}$. (Middle) Daily maximum PBL height from GEOS-FP (Z_{PBL}) with 40% downward correction applied year-round (see Section 2). (Bottom) Daily mean AOD from MODIS and the calculated PBL contribution ($PM_{2.5} \times Z_{PBL}$) assuming a constant mass extinction efficiency of 10 m^2/g. Smoothed curves for all panels are calculated using a low-pass filter. All values are averaged over the Southeast US as defined in **Figure 4.2**.

showed previously that ~30% of the aerosol extinction in SEAC^{4}RS was contributed by PBL venting to the lower free troposphere (**Figure 4.9**). This venting is much less efficient in winter [*Heald et al., 2006b*], which would further damp the seasonality in surface PM.

4.8 Conclusions

We have used a large ensemble of surface, aircraft, and satellite observations during the SEAC^{4}RS field campaign over the Southeast US in August-September 2013 to better understand (1) the sources of sulfate and organic aerosol (OA) in the region; (2) the relationship between the aerosol optical depth (AOD) measured from space and the fine particulate matter concentration ($PM_{2.5}$) measured at the surface; and (3) the seasonal aerosol cycle and the apparent inconsistency between satellite and surface measurements. Our work used the GEOS-Chem global chemical transport model (CTM) with 0.25^o x 0.3125^o (~25 x 25 km^2) horizontal resolution over North America as an integrative platform to compare and interpret the ensemble of observations.

$PM_{2.5}$ surface observations are fairly homogenous across the Southeast US, reflecting regional coherence in stagnation, mixing, and ventilation. Sulfate and OA account for the bulk of $PM_{2.5}$. GEOS-Chem captures the observed spatial distributions of sulfate and OA with no significant bias for sulfate and a +14-66% bias for OA. Interpretation of the OA bias is complicated by differences in sampling and protocol between surface networks. Model results suggest that oxidation of SO_2 by Criegee intermediates (CIs) accounts for 36% of sulfate formation over the Southeast US in summer, although that result depends on uncertain CI kinetics. OA originates mostly from biogenic isoprene (40%) and monoterpenes (20%), with

additional sources from human activity (30%) and open fires (10%).

Aircraft vertical profiles show that 60% of the aerosol column mass is in the PBL below 2 km, 30% is in the lower free troposphere at 2-5 km, and 10% is above 5 km. This is well reproduced in GEOS-Chem. OA accounts for 65% of the aerosol column mass in the observations and this is well simulated by the model. The OA measured from the aircraft is higher than from the surface networks and this appears to reflect in part differences in instrumentation. The successful simulation of OA vertical profiles argues against a large source in the free troposphere other than PBL ventilation. Occasional fire and dust plumes were observed in the free troposphere but have little impact on temporal averages.

Sulfate aerosol over the Southeast US is observed to be acidic despite an excess of ammonia being present. This is inconsistent with thermodynamic equilibrium and with the observation of a 2003-2013 decline in ammonium aerosol concentrations paralleling that of sulfate. We find that the departure from equilibrium is correlated with OA in the aircraft observations, supporting laboratory findings by *Liggio et al.* [2011] that organic gases compete with ammonia for uptake by acid sulfate aerosol. This may have important implications for aerosol hygroscopicity and chemistry.

The vertical profile of aerosol light extinction measured from the aircraft follows closely that of aerosol mass. GEOS-Chem has a 16% low bias in aerosol extinction and simulates correctly the vertical profile. The aerosol above the PBL accounts for 30% of column light extinction, vs. 40% of column mass, reflecting the lower RH at higher altitudes. Sulfate accounts for as much of the column light extinction as OA, despite lower mass concentrations. Evaluation of MODIS and MISR AOD retrievals with AERONET shows excellent agreement. GEOS-Chem is 16% too low, consistent with its bias relative to the aircraft extinction data. The overall

analysis demonstrates consistency and closure between AODs measured from space and from the surface, aircraft aerosol extinction and mass profiles, and surface $PM_{2.5}$ measurements, the largest discrepancy being in the measurement of OA by different instrumentation.

We found that the previously reported summer-to-winter decrease in MODIS AOD data over the Southeast US is driven by a sharp August-to-October transition, in all years. This seasonal transition is well captured by GEOS-Chem where it is caused by declines in both sulfate and OA, due to two common factors. First, a decline in isoprene and monoterpene emissions reduces biogenic SOA formation and SO_2 oxidation from the production of CIs. Second, transition in the NO_x photochemical regime driven by a sharp drop in UV radiation titrates H_2O_2 and associated sulfate production, and also shifts the OA formation mechanism from low-NO_x to high-NO_x conditions.

Previous studies have pointed out an apparent inconsistency between the large seasonal variation of AOD measured from space and the much weaker seasonal variation of $PM_{2.5}$ measured at the surface. We find that this can be largely explained by the seasonal trend in PBL mixing and ventilation, dampening the effect of decreased wintertime PM sources on the surface concentrations. Overall our results show that measured AODs from space are fundamentally consistent with measurements of $PM_{2.5}$ air quality in the Southeast US. This implies that satellite measurements can reliably be used to infer $PM_{2.5}$ if a good CTM representation of PBL mixing and ventilation is available.

Acknowledgements

We are grateful to the entire NASA SEAC^{4}RS team for their help in the field. We thank Aaron van Donkelaar, Eloise Marais, Loretta Mickley, Randall Martin, Ann Dillner, Ralph Kahn, Armin Sorooshian, and Jenny Hand for helpful discussions and Sajeev Philip for assistance with downloading meteorological fields. This work was funded by the NASA Tropospheric Chemistry Program and by a Department of Energy Office of Science Graduate Fellowship to PSK made possible in part by the American Recovery and Reinvestment Act of 2009, administered by ORISE-ORAU under contract no. DE-AC05-06OR23100.

References

Alston, E. J., I. N. Sokolik, and O. V. Kalashnikova (2012), Characterization of atmospheric aerosol in the US Southeast from ground- and space-based measurements over the past decade, *Atmos. Meas. Tech., 5,* 1667-1682, doi:10.5194/amt-5-1667-2012.

Attwood, A. R., et al. (2014), Trends in sulfate and organic aerosol mass in the Southeast U.S.: Impact on aerosol optical depth and radiative forcing, *Geophys. Res. Lett., 41,* 7701-7709, doi:10.1002/2014GL061669.

Barsanti, K. C., A. G. Carlton, and S. H. Chung (2013), Analyzing experimental data and model parameters: implications for predictions of SOA using chemical transport models, *Atmos. Chem. Phys., 13,* 12073-12088, doi:10.5194/acp-13-12073-2013.

Blanchard, C. L., G. M. Hidy, S. Tanenbaum, E. Edgerton, B. Hartsell, and J. Jansen (2008), Carbon in southeastern US aerosol particles: empirical estimates of secondary organic aerosol formation, *Atmos. Environ., 42,* 6710-6720, doi:10.1016/j.atmosenv.2008.04.011.

Blanchard, C. L., G. M. Hidy, S. Tanenbaum, E. S. Edgerton, and B. E. Hartsell (2013), The Southeastern Aerosol Research and Characterization (SEARCH) study: Temporal trends in gas and PM concentrations and composition, 1999-2010, *J. Air Waste Manage. Assoc., 63*(3), 247-259, doi:10.1080/10962247.2012.748523.

Boy, M., et al. (2013), Oxidation of SO_2 by stabilized Criegee Intermediate (sCI) radicals as a crucial source for atmospheric sulfuric acid concentrations, *Atmos. Chem. Phys, 13,* 3865-3879, doi:10.5194/acp-13-3865-2013.

Boys, B. L., et al. (2014), Fifteen-year global time series of satellite-derived fine particulate matter, *Environ. Sci. Technol., 48,* 11109-11118, doi:10.1021/es502113p.

Budisulistiorini, S. H., et al. (2013), Real-time continuous characterization of secondary organic aerosol derived from isoprene epoxydiols in downtown Atlanta, Georgia, using the Aerodyne Chemical Speciation Monitor, *Environ. Sci. Technol., 47,* 5686-5694, doi:10.1021/es400023n.

Campuzano-Jost, P., et al. (2014), Secondary organic aerosol (SOA) derived from isoprene epoxydiols: Insights into formation, aging, and distribution over the continental US from the DC3 and SEAC4RS campaigns, Abstract A33M-02 presented at 2014 Fall Meeting, AGU, San Francisco, Calif., 15-19 Dec.

Canagaratna, M. R., et al. (2007), Chemical and microphysical characterization of ambient aerosols with the aerodyne aerosol mass spectrometer, *Mass Spectrometry Reviews, 26*(2), 185-222, doi:10.1002/mas.20115.

Canagaratna, M. R., et al. (2015), Elemental ratio measurements of organic compounds using aerosol mass spectrometry: characterization, improved calibration, and implications,

Atmos. Chem. Phys., *15,* 253-272, doi:10.5194/acp-15-253-2015.

Carlton, A. G., R. W. Pinder, P. K. Bhave, and G. A. Pouliot (2010), To what extent can biogenic SOA be controlled?, *Environ. Sci. Technol., 44,* 3376-3380, doi:10.1021/es903506b.

Chan, A. W. H., M. N. Chan, J. D. Surratt, P. S. Chhabra, C. L. Loza, J. D. Crounse, L. D. Yee, R. C. Flagan, P. O. Wennberg, and J. H. Seinfeld (2010), Role of aldehyde chemistry and NO_x concentrations in secondary organic aerosol formation, *Atmos. Chem. Phys., 10,* 7169-7188, doi:10.5194/acp-10-7169-2010.

Chao, W., J.-T. Hsieh, C.-H. Chang, and J. J. Lin (2015), Direct kinetic measurement of the reaction of the simplest Criegee intermediate with water vapor, *Science, 347*(6223), 751-754, doi:10.1126/science.1261549.

Chen, G., et al. (2011), Observations of Saharan dust microphysical and optical properties from the Eastern Atlantic during NAMMA airborne field campaign, *Atmos. Chem. Phys., 11,* 723-740, doi:10.5194/acp-11-723-2011.

Chin, M., and D. J. Jacob (1996), Anthropogenic and natural contributions to tropospheric sulfate: A global model analysis, *J. Geophys. Res., 101*(D13), 18691-18699, doi:10.1029/96JD01222.

Chow, J. C., J. G. Watson, L.-W. A. Chen, J. Rice, and N. H. Frank (2010), Quantification of $PM_{2.5}$ organic carbon sampling artifacts in US networks, *Atmos. Chem. Phys., 10,* 5223-5239, doi:10.5194/acp-10-5223-2010.

Crawford, J. H., and K. E. Pickering (2014), DISCOVER-AQ: Advancing strategies for air quality observations in the next decade, *Environmental Manager,* 4-7.

Crounse, J. D., K. A. McKinney, A. J. Kwan, and P. O. Wennberg (2006), Measurement of gas-pase hydroperoxides by chemical ionization mass spectrometry, *Anal. Chem., 78,* 6726-6732, doi:10.1021/ac0604235.

Cubison, M. J., et al. (2011), Effects of aging on organic aerosol from open biomass burning smoke in aircraft and laboratory studies, *Atmos. Chem. Phys., 11,* 12049-12064, doi:10.5194/acp-11-12049-2011.

Darmenov, A. and A. da Silva (2013), The Quick Fire Emissions Dataset (QFED) – Documentation of versions 2.1, 2.2, and 2.4, NASA Technical Report Series of Global Modeling and Data Assimilation, NASA TM-2013-104606, 32, 183 pp.

de Gouw, J. A., and J. L. Jimenez (2009), Organic aerosols in the Earth's atmosphere, *Environ. Sci. Technol., 43,* 7614-7618, doi:10.1021/es9006004.

Dibb, J. E., R. W. Talbot, E. M. Scheuer, G. Seid, M. A. Avery, and H. B. Singh (2003), Aerosol

chemical composition in Asian continental outflow during the TRACE-P campaign: comparison with PEM-West B, *J. Geophys. Res., 108,* 8815, doi:10.1029/2002JD003111, D21.

Dillner, A. M., C. H. Phuah, and J. R. Turner (2009), Effects of post-sampling conditions on ambient carbon aerosol filter measurements, *Atmos. Environ., 43,* 5937-5943, doi:10.1016/j.atmosenv.2009.08.009.

Diner, D., et al. (2005), The value of multiangle measurements for retrieving structurally and radiatively consistent properties of clouds, aerosols, and surfaces, *Remote Sens. Environ., 97,* 495-518, doi:10.1016/j.rse.2005.06.006.

Donahue, N. M., A. L. Robinson, C. O. Stanier, and S. N. Pandis (2006), Coupled partitioning, dilution, and chemical aging of semivolatile organics, *Environ. Sci. Technol., 40,* 2635-2643, doi:10.1021/es052297c.

Drury, E., D. J. Jacob, R. J. D. Spurr, J. Wang, Y. Shinozuka, B. E. Anderson, A. D. Clarke, J. Dibb, C. McNaughton, and R. Weber (2010), Synthesis of satellite (MODIS), aircraft (ICARTT), and surface (IMPROVE, EPA-AQS, AERONET) aerosol observations over eastern North America to improve MODIS aerosol retrievals and constrain surface aerosol concentrations and sources, *J. Geophys. Res., 115,* D14204, doi:10.1029/2009JD012629.

Eddingsaas, N. C., D. G. VanderVelde, and P. O. Wennberg (2010), Kinetics and products of the acid-catalyzed ring-opening of atmospherically relevant butyl epoxy alcohols, *J. Phys. Chem. A, 114,* 8106-8113, doi:10.1021/jp103907c.

Edgerton, E. S., B. E. Hartsell, R. D. Saylor, J. J. Jansen, D. A. Hansen, and G. M. Hidy (2005), The Southeastern Aerosol Research and Characterization Study: Part II. Filter-based measurements of fine and coarse particulate matter mass and composition, *J. Air & Waste Manage. Assoc., 52,* 1527-1542, doi:10.1080/10473289.2005.10464744.

Edgerton, E. S., et al. (2014), First look at ^{14}C data during the Centreville, AL SOAS campaign, presented at the SAS Data Workshop, Boulder, Co., 31 Mar. – 2 Apr.

EPA (1999), Particulate matter ($PM_{2.5}$) speciation guidance, Final draft, Edition 1, October 7, 1999. U.S. Environmental Protection Agency, Monitoring and Quality Assurance Group, Emissions, Monitoring, and Analysis Division, Office of Air Quality Planning and Standards, Research Triangle Park, NC. http://www.epa.gov/ttn/amtic/files/ambient/pm25/spec/specfinl.pdf.

Ervens, B., B. J. Turpin, and R. J. Weber (2011), Secondary organic aerosol formation in cloud droplets and aqueous particles (aqSOA): a review of laboratory, field and model studies, *Atmos. Chem. Phys., 11,* 11069-11102, doi:10.5194/acp-11-11069-2011.

Fairlie, T. D., D. J. Jacob, and R. J. Park (2007), The impact of transpacific transport of mineral

dust in the United States, *Atmos. Environ., 41,* 1251-1266, doi:10.1016/j.atmosenv.2006.09.048.

Fischer, E. V., et al. (2014), Atmospheric peroxyacetyl nitrate (PAN): a global budget and source attribution, *Atmos. Chem. Phys., 14,* 2679-2698, doi:10.5194/acp-14-2679-2014.

Fisher, J. A., et al. (2015), Isoprene nitrate chemistry in the Southeast US constrained by aircraft ($SEAC^4RS$) and ground-based (SOAS) observations: Implications for NO_x and aerosol budgets, in prep.

Ford, B., and C. L. Heald (2013), Aerosol loading in the Southeastern United States: reconciling surface and satellite observations, *Atmos. Chem. Phys., 13,* 9269-9283, doi:10.5194/acp-13-9269-2013.

Fountoukis, C., and A. Nenes (2007), ISORROPIA II: a computationally efficient thermodynamic equilibrium model for K^+-Ca^{2+}-Mg^{2+}-NH_4^+-Na^+-SO_4^{2-}-NO_3^--Cl^--H_2O aerosols, *Atmos. Chem. Phys., 7,* 4639-4659, doi:10.5194/acp-7-4639-2007.

Froyd, K. D., S. M. Murphy, D. M. Murphy, J. A. de Gouw, N. C. Eddingsaas, and P. O. Wennberg (2010), Contribution of isoprene-derived organosulfates to free tropospheric aerosol mass, *Proc. Natl. Acad. Sci., 107*(50), 21360-21365, doi:10.1073/pnas.1012561107.

Fu, T. M., D. J. Jacob, and C. L. Heald (2009), Aqueous-phase reactive uptake of dicarbonyls as a source of organic aerosol over eastern North America, *Atmos. Environ., 43,* 1814-1822, doi: 10.1016/j.atmosenv.2008.12.029.

Goldstein, A. H., C. D. Koven, C. L. Heald, and I. Y. Fung (2009), Biogenic carbon and anthropogenic pollutants combine to form a cooling haze over the southeastern United States, *Proc. Natl. Acad. Sci., 106*(22), 8835-8840, doi:10.1073/pnas.0904128106.

Guenther, A. B., X. Jiang, C. L. Heald, T. Sakulyanontvittaya, T. Duhl, L. K. Emmons, and X. Wang (2012), The Model of Emissions of Gases and Aerosols from Nature version 2.1 (MEGAN2.1): an extended and updated framework for modeling biogenic emissions, *Geosci. Model Dev., 5,* 1471-1492, doi:10.5194/gmd-5-1471-2012.

Hair, J. W., C. A. Hostetler, A. L. Cook, D. B. Harper, R. A. Ferrare, T. L. Mack, W. Welch, L. R. Izquierdo, and F. E. Hovis (2008), Airborne High Spectral Resolution Lidar for profiling aerosol optical properties, *Appl. Optics, 47,* 6734-6752, doi:10.1364/AO.47.006734.

Hand, J. L., B. A. Schichtel, M. Pitchford, W. C. Malm, and N. H. Frank (2012a), Seasonal composition of remote and urban fine particulate matter in the United States, *J. Geophys. Res., 117,* D05209, doi:10.1029/2011JD017122.

Hand, J. L., B. A. Schichtel, W. C. Malm, and M. L. Pitchford (2012b), Particulate sulfate ion

concentration and SO_2 emission trends in the United States from the early 1990s through 2010, *Atmos. Chem. Phys., 12,* 10353-10365, doi:10.5194/acp-12-10353-2012.

Hayes, P. L., et al. (2014), Modeling the formation and aging of secondary organic aerosols in Los Angeles during CalNex 2010, *Atmos. Chem. Phys. Discuss, 14,* 32325-32391, doi:10.5194/acpd-14-32325-2014.

Heald, C. L., et al. (2006a), Concentrations and sources of organic carbon aerosols in the free troposphere over North America, *J. Geophys. Res., 111,* D23S47, doi:10.1029/2006JD007705.

Heald, C. L., D. J. Jacob, R. J. Park, B. Alexander, T. D. Fairlie, R. M. Yantosca, and D. A. Chu (2006b), Transpacific transport of Asian anthropogenic aerosols and its impact on surface air quality in the United States, *J. Geophys. Res., 111,* D14310, doi:10.1029/2005JD006847.

Heald, C. L., et al. (2011), Exploring the vertical profile of atmospheric organic aerosol: comparing 17 aircraft field campaigns with a global model, *Atmos. Chem. Phys., 11,* 12673-12696, doi:10.5194/acp-11-12673-2011.

Heald, C. L., et al. (2012), Atmospheric ammonia and particulate inorganic nitrogen over the United States, *Atmos. Chem. Phys., 12,* 10295-10312, doi:10.5194/acp-12-10295-2012.

Henze, D. K., and J. H. Seinfeld (2006), Global secondary organic aerosol from isoprene oxidation, *Geophys. Res. Lett., 33,* L09812, doi:10.1029/2006GL025976.

Hermansson, E., P. Roldin, A. Rusanen, D. Mogensen, N. Kivekas, R. Vaananen, M. Boy, and E. Swietlicki (2014), Biogenic SOA formation through gas-phase oxidation and gas-to-particle partitioning – a comparison between process models of varying complexity, *Atmos. Chem. Phys., 14,* 11853-11869, doi:10.5194/acp-14-11853-2014.

Hidy, G. M., C. L. Blanchard, K. Baumann, E. Edgerton, S. Tanenbaum, S. Shaw, E. Knipping, I. Tombach, J. Jansen, and J. Walters (2014), Chemical climatology of the southeastern Unisted States, 1999-2013, *Atmos. Chem. Phys., 14,* 11893-11914, doi:10.5194/acp-14-11893-2014.

Hodzic, A., and J. L. Jimenez (2011), Modeling anthropogenically controlled secondary organic aerosols in a megacity: a simplified framework for global and climate models, *Geosci. Model Dev., 4,* 901-917, doi:10.5194/gmd-4-901-2011.

Holben, B., et al. (1998), AERONET – A federated instrument network and data archive for aerosol characterization, *Remote Sens. Environ., 66,* 1-16, doi:10.1016/S0034-4257(98)00031-5.

Hoyle, C., et al. (2011), A review of the anthropogenic influence on biogenic secondary organic aerosol, *Atmos. Chem. Phys., 11,* 321-343, doi:10.5194/acp-11-321-2011.

Hu, W., et al. (2015), Characterization of a real-time tracer for isoprene epoxydiols-derived secondary organic aerosol (IEPOX-SOA) from aerosol mass spectrometer measurements, in prep.

Hu, X., L. A. Walker, A. Lyapustin, Y. Wang, and Y. Liu (2014), 10-year spatial and temporal trends of $PM_{2.5}$ concentrations in the southeastern US estimated using high-resolution satellite data, *Atmos. Chem. Phys., 14,* 6301-6314, doi:10.5194/acp-14-6301-2014.

Hudman, R. C., N. E. Moore, A. K. Mebust, R. V. Martin, A. R. Russell, L. C. Valin, and R. C. Cohen (2012), Steps towards a mechanistic model for global soil nitric oxide emissions: implementation and space-based constraints, *Atmos. Chem. Phys., 12,* 7770 – 7795, doi:10.5194/acp-12-7779-2012.

Jacob, D. J., L. W. Horowitz, J. W. Munger, B. G. Heikes, R. R. Dickerson, R. S. Artz, and W. C. Keene (1995), Seasonal transition from NO_x- to hydrocarbon-limited conditions for ozone production over the eastern United States in September, *J. Geophys. Res., 100*(D5), 9315-9324, doi:10.1029/94JD03125.

Jaegle, L., P. K. Quinn, T. S. Bates, B. Alexander, and J.-T. Lin (2011), Global distribution of sea salt aerosols: new constraints from in situ and remote sensing observations, *Atmos. Chem. Phys., 11,* 3137-3157, doi:10.5194/acp-11-3137-2011.

Jenkin, M. E., S. M. Saunders, and M. J. Pilling (1997), The tropospheric degradation of volatile organic compounds: A protocol for mechanism development, *Atmos. Environ., 31,* 81-104, doi:10.1016/s1352-2310(96)00105-7.

Jimenez, J., et al. (2009), Evolution of organic aerosols in the atmosphere, *Science, 326*(5959), 1525-1529, doi:10.1126/science.1180353.

Kim, P. S., D. J. Jacob, X. Liu, J. X. Warner, K. Yang, K. Chance, V. Thouret, and P. Nedelec (2013), Global ozone-CO correlations from OMI and AIRS: constraints on tropospheric ozone sources, *Atmos. Chem. Phys., 13,* 9321-9335, doi:10.5194/acp-13-9321-2013.

Kleindienst, T. E., M. Jaoui, M. Lewandowski, J. H. Offenberg, C. W. Lewis, P. V. Bhave, and E. O. Edney (2007), Estimates of the contributions of biogenic and anthropogenic hydrocarbons to secondary organic aerosol at a southeastern US location, *Atmos. Environ., 41,* 8288-8300, doi:10.1016/j.atmosenv.2007.06.045.

Kleinman, L. I., (1991), Seasonal dependence of boundary layer peroxide concentration: The low and high NO_x regimes, *J. Geophys. Res., 96(D11),* 20721 – 20733, doi:10.1029/91JD02040.

Koepke P., M. Hess, I. Schult, and E. P. Shettle (1997), Global Aerosol Data Set, Max-Planck-Institut fur Meteorologie, Hamburg.

Kroll, J. H., N. L. Ng, S. M. Murphy, R. C. Flagan, and J. H. Seinfeld (2005), Secondary organic aerosol formation from isoprene photooxidation under high-NO_x conditions, *Geophys. Res. Lett., 32,* L18808, doi:10.1029/2005GL023637.

Kroll, J. H., N. L. Ng, S. M. Murphy, R. C. Flagan, and J. H. Seinfeld (2006), Secondary organic aerosol formation from isoprene photooxidation, *Environ. Sci. Technol., 40,* 1869-1877, doi:10.1021/es0524301.

Langridge, J. M., M. S. Richardson, D. Lack, D. Law, and D. M. Murphy (2011), Aircraft instrument for comprehensive characterization of aerosol optical properties, Part I: Wavelength-dependent optical extinction and its relative humidity dependence measured using cavity ringdown spectroscopy, *Aerosol Sci. Technol., 45*(11), 1305:1318, doi:10.1080/02786826.2011.592745.

Leibensperger, E. M., L. J. Mickley, D. J. Jacob, W.-T. Chen, J. H. Seinfeld, A. Nenes, P. J. Adams, D. G. Streets, N. Kumar, and D. Rind (2012), Climatic effects of 1950-2050 changes in US anthropogenic aerosols – Part 1: Aerosol trends and radiative forcing, *Atmos. Chem. Phys., 12,* 3333-3348, doi:10.5194/acp-12-3333-2012.

Leibensperger, E. M., L. J. Mickley, D. J. Jacob, W.-T. Chen, J. H. Seinfeld, A. Nenes, P. J. Adams, D. G. Streets, N. Kumar, and D. Rind (2012b), Climatic effects of 1950-2050 changes in US anthropogenic aerosols – Part 2: Climate response, *Atmos. Chem. Phys., 12,* 3349-3362, doi:10.5194/acp-12-3349-2012.

Levy, R. C., S. Mattoo, L. A. Munchak, L. A. Remer, A. M. Sayer, F. Patadia, and N. C. Hsu (2013), The Collection 6 MODIS aerosol products over land and ocean, *Atmos. Meas. Tech., 6,* 2989-3034, doi:10.5194/amt-6-2989-2013.

Li, J., Q. Ying, B. Yi, and P. Yang (2013), Role of stabilized Criegee Intermediates in the formation of atmospheric sulfate in eastern United States, *Atmos. Environ., 79,* 442-447, doi:10.106/j.atmosenv.2013.06.048.

Liggio, J., S.-M. Li, A. Vlasenko, C. Stroud, and P. Makar (2011), Depression of ammoniua uptake to sulfuric acid aerosols by competing uptake of ambient organic gases, *Environ. Sci. Technol., 45,* 2790-2796, doi:10.1021/es103801g.

Lim, H.-J., and B. J. Turpin (2002), Origins of primary and secondary organic aerosol in Atlanta: results of time-resolved measurements during the Atlanta Supersite Experiment, *Environ. Sci. Technol., 36,* 4489-4496, doi:10.1021/es0206487.

Liu, D., Z. Wang, Z. Liu, D. Winker, and C. Trepte (2008), A height resolved global view of dust aerosols from the first year CALIPSO lidar measurements, *J. Geophys. Res., 113,* D16214, doi:10.1029/2007JD009776.

Liu, H., D. J. Jacob, I. Bey, and R. M. Yantosca (2001), Constraints from ^{210}Pb and ^{7}Be on wet deposition and transport in a global three-dimensional chemical tracer model driven by

assimilated meteorological fields, *J. Geophys. Res.*, *106*(D11), 12109–12128, doi:10.1029/2000JD900839.

Liu Y., R. J. Park, D. J. Jacob, Q. Li, V. Kilaru, and J. A. Sarnat (2004), Mapping annual mean ground-level $PM_{2.5.}$ concentrations using Multiangle Imaging Spectroradiometer aerosol optical thickness over the contiguous United States, *J. Geophys, Res., 109,* D22206, doi:10.1029/2004JD005025.

Mao, J., F. Paulot, D. J. Jacob, R. C. Cohen, J. D. Crounse, P. O. Wennberg, C. A. Keller, R. C. Hudman, M. P. Barkley, and L. W. Horowitz (2013), Ozone and organic nitrates over the eastern United States: Sensitivity to isoprene chemistry, *J. Geophys. Res. Atmos., 118,* 11256-11268, doi:10.1002/jgrd/50817.

Malm, W. C., J. F. Sisler, D. Huffman, R. A. Eldred, and T. A. Cahill (1994), Spatial and seasonal trends in particle concentration and optical extinction in the United States, *J. Geophys. Res., 99*(D1), 1347-1370, doi:10.1029/93JD02916.

Marais, E., et al. (2015), Isoprene aerosol yield quantified with space-based relationships between aerosol optical depth and formaldehyde: Contrasting regimes in Africa and the Southeast US, in prep.

Martin, R. V., D. J. Jacob, R. M. Yantosca, M. Chin, and P. Ginoux (2003), Global and regional decreases in tropospheric oxidants from photochemical effects of aerosols, *J. Geophys. Res., 108,* 4097, doi:10.1029/2002JD002622.

Martin, S. T., H.-H. Hung, R. J. Park, D. J. Jacob, R. J. D. Spurr, K. V. Chance, and M. Chin (2004), Effects of the physical state of tropospheric ammonium-sulfate-nitrate particles on global aerosol direct radiative forcing, *Atmos. Chem. Phys., 4,* 183-214, doi:10.5194/acp-4-183-2004.

Mauldin III, R. L., T. Berndt, M. Sipila, P. Paasonen, T. Petaja, S. Kim, T. Kurten, F. Stratmann, V.-M. Kerminen, and M. Kulmala (2012), A new atmospherically relevant oxidant of sulphur dioxide, *Nature, 488,* 193-196, doi:10.1038/nature11278.

McKeen, S., et al. (2007), Evaluation of several $PM_{2.5}$ forecast models using data collected during the ICARTT/NEAQS 2004 field study, *J. Geophys. Res., 112,* D10S20, doi:10.1029/2006JD007608.

Millet, D. B., et al. (2015), A large and ubiquitous source of atmospheric formic acid, *Atmos. Chem. Phys. Discuss., 15,* 4537-4599, doi:10.5194/acpd-15-4537-2015.

Murphy, B. N., N. M. Donahue, C. Fountoukis, M. Dall'Osto, C. O'Dowd, A. Kiendler-Scharr, and S. N. Pandis (2012), Functionalization and fragmentation during ambient organic aerosol aging: application of the 2-D volatility basis set to field studies, *Atmos. Chem. Phys., 12,* 10797-10816, doi:10.5194/acp-12-10797-2012.

NADP (2015), National Atmospheric Deposition Program Animated Maps, Available at: http://nadp.sws.uiuc.edu/data/animaps.aspx, Accessed: March 7, 2015.

Newland, M. J., A. R. Rickard, M. S. Alam, L. Vereecken, A. Munoz, M. Rodenas, and W. J. Bloss (2014), Kinetics of stabilised Criegee intermediates derive from alkene ozonolysis: reactions with SO_2, H_2O and decomposition under boundary layer conditions, *Phys. Chem. Chem. Phys., 17,* 4076-4088, doi:10.1039/c4cp04186k.

NOAA National Climatic Data Center (2011), State of the Climate: Wildfires for Annual 2011, published online December 2011, retrieved on March 26, 2015 from http://www.ncdc.noaa.gov/sotc/fire/2011/13.

Park, R. J., D. J. Jacob, M. Chin, and R. V. Martin (2003), Sources of carbonaceous aerosols over the United States and implications for natural visibility, *J. Geophys. Res., 108*(D12), 4355, doi:10.1029/2002JD003190.

Park, R. J., D. J. Jacob, B. D. Field, R. M. Yantosca, and M. Chin (2004), Natural and transboundary pollution influences on sulfate-nitrate-ammonium aerosols in the Untied States: Implications for policy, *J. Geophys. Res., 109,* D15204, doi:10.1029/2003JD004473.

Park, R. J., D. J. Jacob, N. Kumar, and R. M. Yantosca (2006), Regional visibility statistics in the United States: Natural and transboundary pollution influences, and implications for the Regional Haze Rule, *Atmos. Environ., 40,* 5405-5423, doi:10.1016/j.atmosenv.2006.04.059.

Park, R. J., D. J. Jacob, and J. A. Logan (2007), Fire and biofuel contributions to annual mean aerosol mass concentrations in the United States, *Atmos. Environ., 41,* 7389-7400, doi:10.1016/j.atmosenv.2007.05.061.

Paulot, F., D. J. Jacob, R. W. Pinder, J. O. Bash, K. Travis, and D. K. Henze (2014), Ammonia emissions in the Untied States, European Union, and China derived by high-resolution inversion of ammonium wet deposition data: Interpretation with a new agricultural emissions inventory (MASAGE_NH3), *J. Geophys. Res. Atmos., 119,* 4343-4364, doi:10.1002/2013JD021130.

Peterson, D. A., E. J. Hyer, J. R. Campbell, M. D. Fromm, J. W. Hair, C. F. Butler, and M. A. Fenn (2015), The 2013 Rim Fire: Implications for predicting extreme fire spread, pyroconvection, and smoke emissions, *Bull. Amer. Meteor. Soc.,* doi:10.1175/BAMS-D-14-00060.1.

Pfister, L., et al. (2015), A meteorological overview of the SEAC^{4}RS mission, *in prep.*

Pierce, J. R., M. J. Evans, C. E. Scott, S. D. D' Andrea, D. K. Farmer, E. Swietlicki, and D. V. Spracklen (2013), Weak global sensitivity of cloud condensation nuclei and aerosol indirect effect to Criegee + SO_2 chemistry, *Atmos. Chem. Phys., 13,* 3163-3176,

doi:10.5194/acp-13-3163-2013.

Pye, H. O. T., H. Liao, S. Wu, L. J. Mickley, D. J. Jacob, D. K. Henze, and J. H. Seinfeld (2009), Effect of changes in climate and emissions on future sulfate-nitrate-ammonium aerosol levels in the United States, *J. Geophys. Res., 114,* D01205, doi:10.1029/2008JD010701.

Remer, L. A., et al. (2005), The MODIS aerosol algorithm, products, and validation, *J. Atmos. Sci., 62,* 947-973, doi:10.1175/jas3385.1.

Russell, A. R., L. C. Valin, and R. C. Cohen (2012), Trends in OMI NO_2 observations over the United States: effects of emission control technology and the economic recession, *Atmos. Chem. Phys., 12,* 12197-12209, doi:10.5194/acp-12-12197-2012.

Saide, P. E., et al. (2015), Revealing important nocturnal and day-to-day variations in fire smoke emissions through a novel multiplatform inversion, submitted.

Sarwar, G., H. Simon, K. Fahey, R. Mathur, W. S. Goliff, and W. R. Stockwell (2014), Impact of sulfur dioxide oxidation by Stabilized Criegee Intermediate on sulfate, *Atmos. Environ., 85,* 204-214, doi:10.1016/j.atmosenv.2013.12.013.

Saunders, S. M., M. E. Jenkin, R. G. Derwent, and M. J. Pilling (2003), Protocol for the development of the Master Chemical Mechanism, MCM v3 (Part A): Tropospheric degradation of non-aromatic volatile organic compounds, *Atmos. Chem. Phys., 3,* 161-180, doi:10.5194/acp-3-161-2003.

Schwarz, J. P., et al. (2008), Measurement of the mixing state, mass, and optical size of individual black carbon particles in urban and biomass burning emissions, *Geophys. Res. Lett., 35*(13), doi:10.1029/2008gl033968.

Sipila, M., et al. (2014), Reactivity of stabilize Criegee intermediates (sCIs) from isoprene and monoterpene ozonolysis toward SO_2 and organic acids, *Atmos. Chem. Phys., 14,* 12143-12153, doi:10.5194/acp-14-12143-2014.

Solomon, P. A., D. Crumpler, J. B. Flanagan, R. K. M. Jayanty, E. E. Rickman, and C. E. McDade (2014), U.S. National $PM_{2.5}$ Chemical Speciation Monitoring Networks – CSN and IMPROVE: Description of Networks, *J. Air Waste Manage. Assoc., 64*(12), 1410-1438, doi:10.1080/10962247.2014.956904.

Spracklen, D. V., et al. (2011), Aerosol mass spectrometer constraint on the global secondary organic aerosol budget, *Atmos. Chem. Phys., 11,* 12109-12136, doi:10.5194/acp-11-12109-2011.

St. Clair, J. M., D. C. McCabe, J. D. Crounse, U. Steiner, and P. O. Wennberg (2010), Chemical ionization tandem mass spectrometer for the in situ measurement of methyl hydrogen peroxide, *Rev. Sci. Instrum., 81,* 094102-094106, doi:10.1063/1.3480552.

Stone, D., M. Blitz, L. Daubney, N. U. Howes, and P. Seakins (2014), Kinetics of CH_2OO reactions with SO_2, NO_2, NO, H_2O, and CH_3CHO as a function of pressure, *Phys. Chem. Chem. Phys., 16,* 1139-1149, doi:10.1039/c3cp54391a.

Thomson, D. S., M. E. Schein, and D. M. Murphy, Particle analysis by laser mass spectrometry WB-57F instrument overview (2000), *Aerosol Sci. Technol., 33(1-2),* 153-169, doi:10.1080/027868200410903.

Thornhill, K. L., et al. (2008), The impact of local sources and long-range transport on aerosol properties over the northeast U.S. region during INTEX-NA, *J. Geophys. Res., 113,* D08201, doi:10.1029/2007JD008666.

Toon, O. B., et al. (2015), Planning, implementation, and scientific goals of the Studies of Emissions and Atmospheric Composition, Clouds, and Climate Coupling by Regional Surveys ($SEAC^4RS$) field mission, in prep.

Travis, K., et al. (2015), Declining NO_x in the Southeast US and implications for ozone-NO_x-VOC chemistry, *in prep.*

Tsigaridis, K. et al. (2014), The AeroCom evaluation and intercomparison of organic aerosol in global models, *Atmos. Chem. Phys., 14,* 10845-10895, doi:10.5194/acp-14-10845-2014.

Turquety, S., et al. (2007), Inventory of boreal fire emissions for North America in 2004: the importance of peat burning and pyro-convective injections, *J. Geophys. Res., 112(D12),* D12S03, doi:10.1029/2006JD007281.

van Donkelaar, A., R. V. Martin, M. Brauer, R. Kahn, R. Levy, C. Verduzco, and P. J. Villeneuve (2010), Global estimates of ambient fine particulate matter concentrations from satellite-based aerosol optical depth: development and application, *Environ. Health Perspect., 118(6),* 847-855, doi:10.1289/ehp.0901623.

van Donkelaar, A., R. V. Martin, A. N. Pasch, J. J. Szykman, L. Zhang, Y. X. Wang, and D. Chen (2012), Improving the accuracy of daily-satellite-derived ground-level fine aerosol concentration estimates for North America, *Environ. Sci. Technol., 46,* 11971-11978, doi:10.1021/es3025319.

van Donkelaar, A., R. V. Martin, R. J. D. Spurr, E. Drury, L. A. Remer, R. C. Levy, and J. Wang (2013), Optimal estimation for global ground-level fine particulate matter concentrations, *J. Geophys. Res. Atmos., 118,* 5621-5636, doi:10.1002/jgrd.50479.

van Donkelaar, A., R. V. Martin, M. Brauer, and B. L. Boys (2015), Use of satellite observations for long-term exposure assessment of global concentrations of fine particulate matter, *Environ. Health Perspect., 123(2),* 135-143, doi:10.1289/ehp.1408646.

Wagner, N., et al. (2015), In situ vertical profiles of aerosol extinction, mass, and composition over the southeast United States during SENEX and SEAC4RS: Observations of a

modest aerosol enhancement aloft, *Atmos. Chem. Phys. Discuss., 15,* 3127-3172, doi:10.5194/acpd-15-3127-2015.

Walker, J. M., S. Philip, R. V. Martin, and J. H. Seinfeld (2012), Simulation of nitrate, sulfate, and ammonium aerosols over the United States, *Atmos. Chem. Phys., 12,* 11213-11227, doi:10.5194/acp-12-11213-2012.

Wang, J., D. J. Jacob, and S. T. Martin (2008), Sensitivity of sulfate direct climate forcing to the hysteresis of particle phase transitions, *J. Geophys. Res., 113,* D11207, doi:10.1029/2007JD009368.

Wang, Q., D. J. Jacob, J. R. Spackman, A. E. Perring, J. P. Schwarz, N. Moteki, E. A. Marais, C. Ge, J. Wang, and S. R. H. Barrett (2014), Global budget and radiative forcing of black carbon aerosol: Constraints from pole-to-pole (HIPPO) observations across the Pacific, *J. Geophys. Res. Atmos., 119,* 195-206, doi:10.1002/2013JD020824.

Warneke, C., et al. (2015), Instrumentation and measurement strategy for the NOAA SENEX aircraft campaign as part of the Southeast Atmosphere Study 2013, in prep.

Weber, R., et al. (2007), A study of secondary organic aerosol formation in the anthropogenic-influenced southeastern United States, *J. Geophys. Res., 112,* D13302, doi:10.1029/2007JD008408.

Welz, O., J. D. Savee, D. L. Osborn, S. S. Vasu, C. J. Percival, D. E. Shallcross, and C. A. Taatjes (2012), Direct kinetic measurements of Criegee Intermediate (CH_2OO) formed by reaction of CH_2I with O_2, *Science, 335,* 204-207.

Wolfe, G. M., et al. (2015), Airborne flux observations provide novel constraints on sources and sinks of reactive gases in the lower atmosphere, submitted.

WRAP, Western Regional Air Partnership (2005), Development of 2000-04 Baseline Period and 2018 Projection Year Emission Inventories, Prepared by Air Sciences, Inc. Project No. 178-8.

Xu, L., M. S. Kollman, C. Song, J. E. Shilling, and N. L. Ng (2014), Effects of NO_x on the volatility of secondary organic aerosol from isoprene photooxidation, *Environ. Sci. Technol., 48,* 2253-2262, doi:10.1021/es404842g.

Yu, K., et al. (2015), Impact of grid resolution on the simulation of tropospheric chemistry constrained by observations from the SEAC^{4}RS aircraft campaign, in prep.

Yu, S., R. L. Dennis, P. V. Bhave, and B. K. Ender (2004), Primary and secondary organic aerosols over the United States: estimates on the basis of observed organic carbon (OC) and elemental carbon (EC), and air quality modeled primary OC/EC ratios, *Atmos. Environ., 38,* 5257-5268, doi:10.1016/j.atmosenv.2004.02.064.

Zhang, H., R. M. Hoff, and J. A. Engel-Cox (2009), The relation between Moderate Resolution

Imaging Spectroradiometer (MODIS) aerosol optical depth and $PM_{2.5}$ over the United States: a geographical comparison by U.S. Environmental Protection Agency regions, *J. Air Waste Manage. Assoc.,* 59:11, 1358-1369, doi:10.3155/1047-3289.59.11.1358.

Zhang, L., S. Gong, J. Padro, and L. Barrie (2001), A size-segregated particle dry deposition scheme for an atmospheric aerosol module, *Atmos. Environ., 35,* 549-560, doi:10.1016/s1352-2310(00)00326-5.

Zhang, L., D. J. Jacob, E. M. Knipping, N. Kumar, J. W. Munger, C. C. Carouge, A. van Donkelaar, Y. X. Wang, and D. Chen (2012), Nitrogen deposition to the United States: distribution, sources, and processes, *Atmos. Chem. Phys., 12,* 4539-4554, doi:10.5194/acp-12-4539-2012.

Zhang, Q., et al. (2007), Ubiquity and dominance of oxygenated species in organic aerosols in anthropogenically-influenced Northern Hemisphere midlatitudes, *Geophys. Res. Lett., 34,* L13801, doi:10.1029/2007GL029979.

Zhang, X., Z. Liu, A. Hecobian, M. Zheng, N. H. Frank, E. S. Edgerton, and R. J. Weber (2012), Spatial and seasonal variations of fine particle water-soluble organic carbon (WSOC) over the southeastern United States: implications for secondary organic aerosol formation, *Atmos. Chem. Phys., 12,* 6593-6607, doi:10.5194/acp-12-6593-2012.

Zhu, L., et al. (2015), Indirect validation of satellite tropospheric HCHO data during SEAC4RS and application to derive surface HCHO over the continental US, in prep.

Zotter, P., et al. (2014), Diurnal cycle of fossil and nonfossil carbon using radiocarbon analyses during CalNex, *J. Geophys. Res. Atmos., 119,* 6818-6835, doi:10.1002/2013JD021114.

Appendix:

Supplementary Figures and Tables

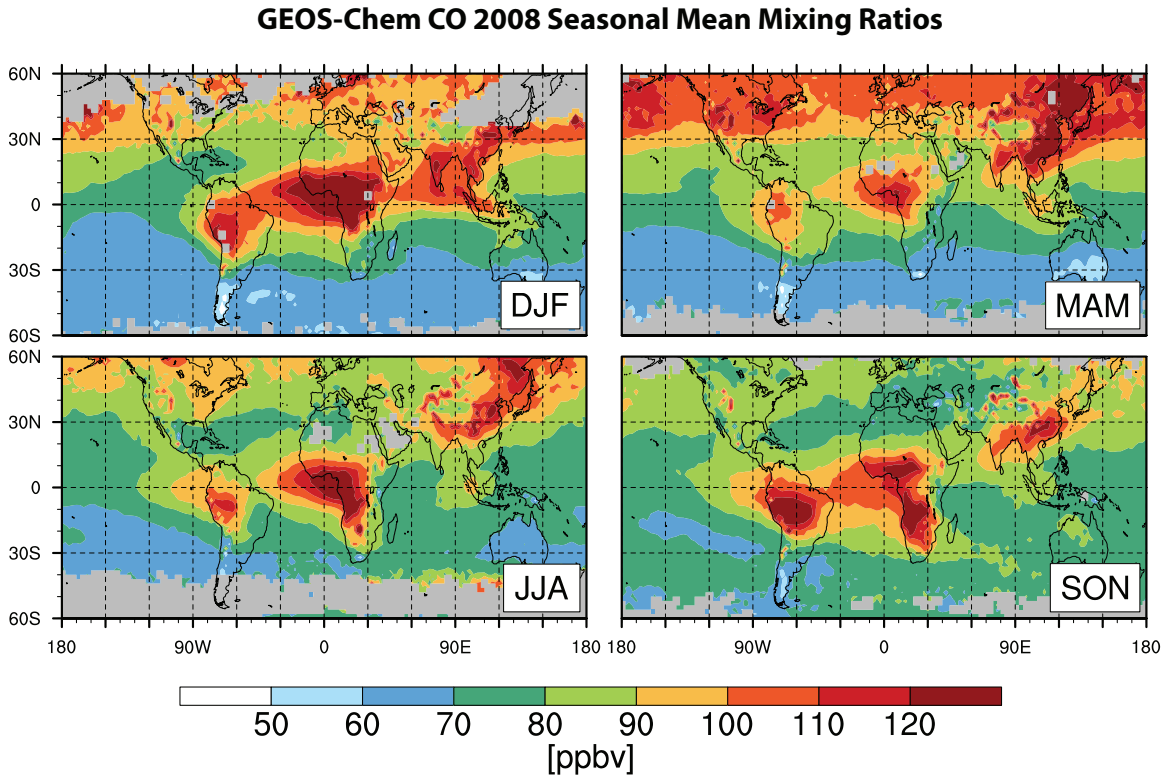

Figure A.1: Seasonal mean GEOS-Chem CO mixing ratios at 700-400 hPa for 2008. Gray indicates insufficient data (see Chapter 2).

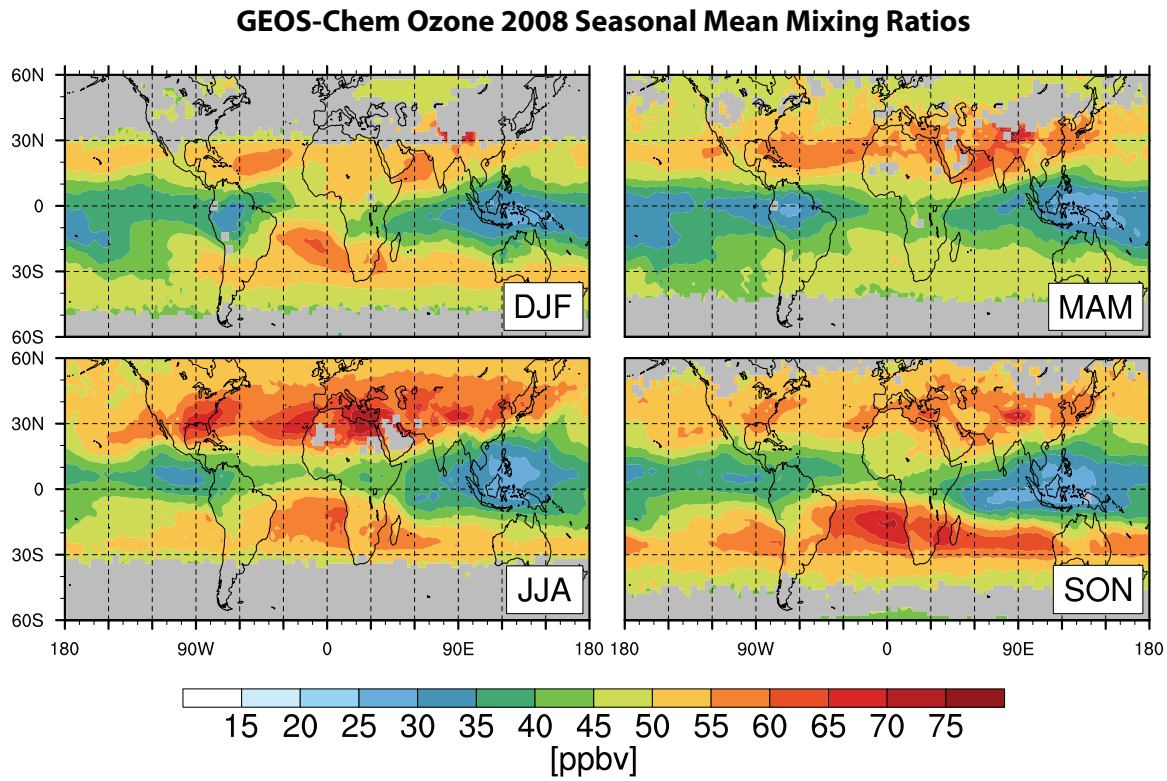

Figure A.2: Same as **Figure A.1** but for GEOS-Chem ozone mixing ratios at 700-400 hPa.

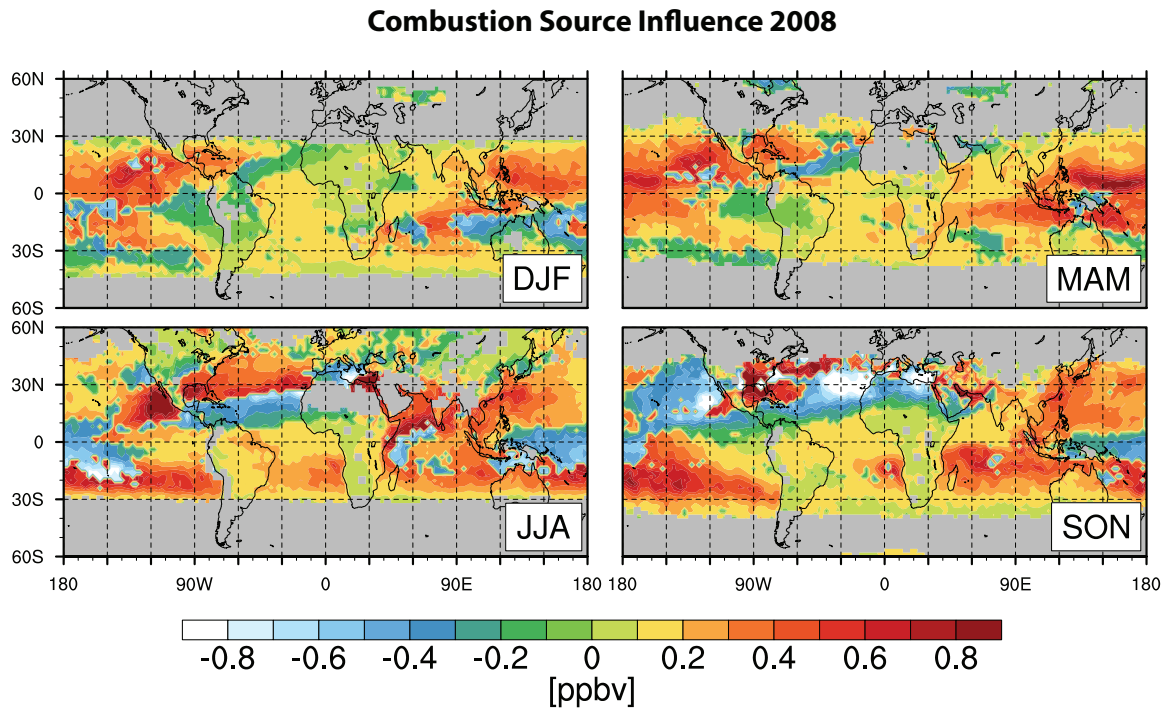

Figure A.3: $d\Delta O_3/dCO$ for a simulation without combustion sources in each season of 2008. Gray indicates insufficient data (see Chapter 2).

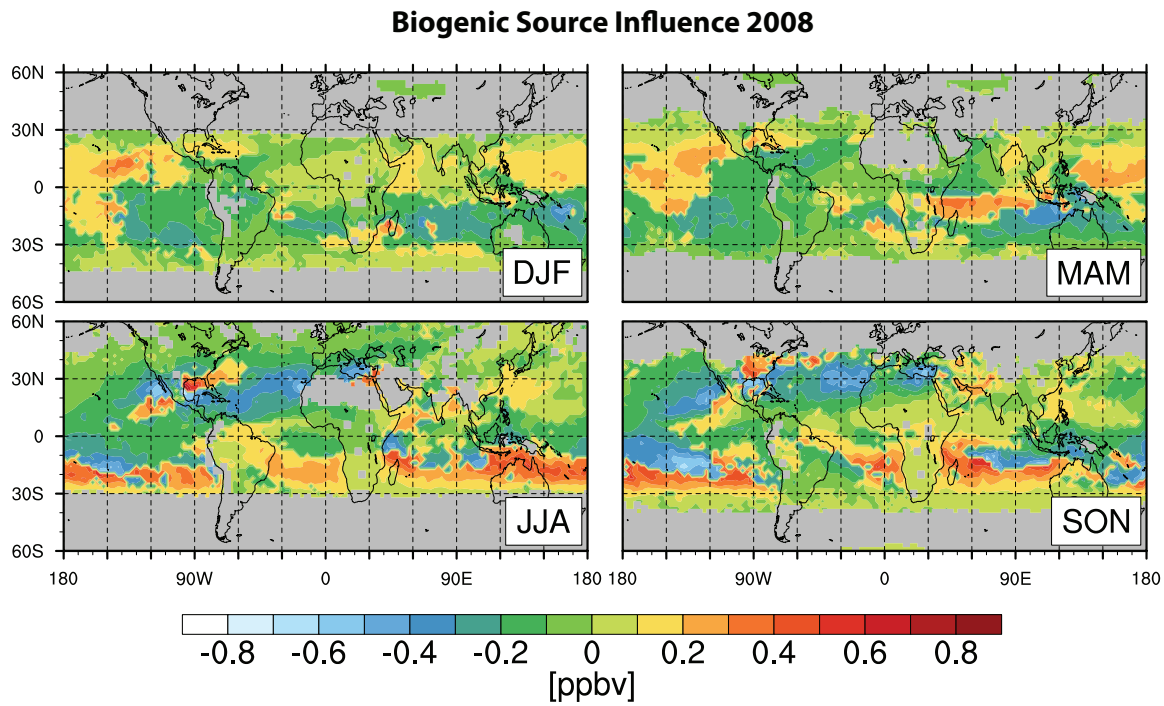

Figure A.4: Same as **Figure A.3** but for a simulation without biogenic sources.

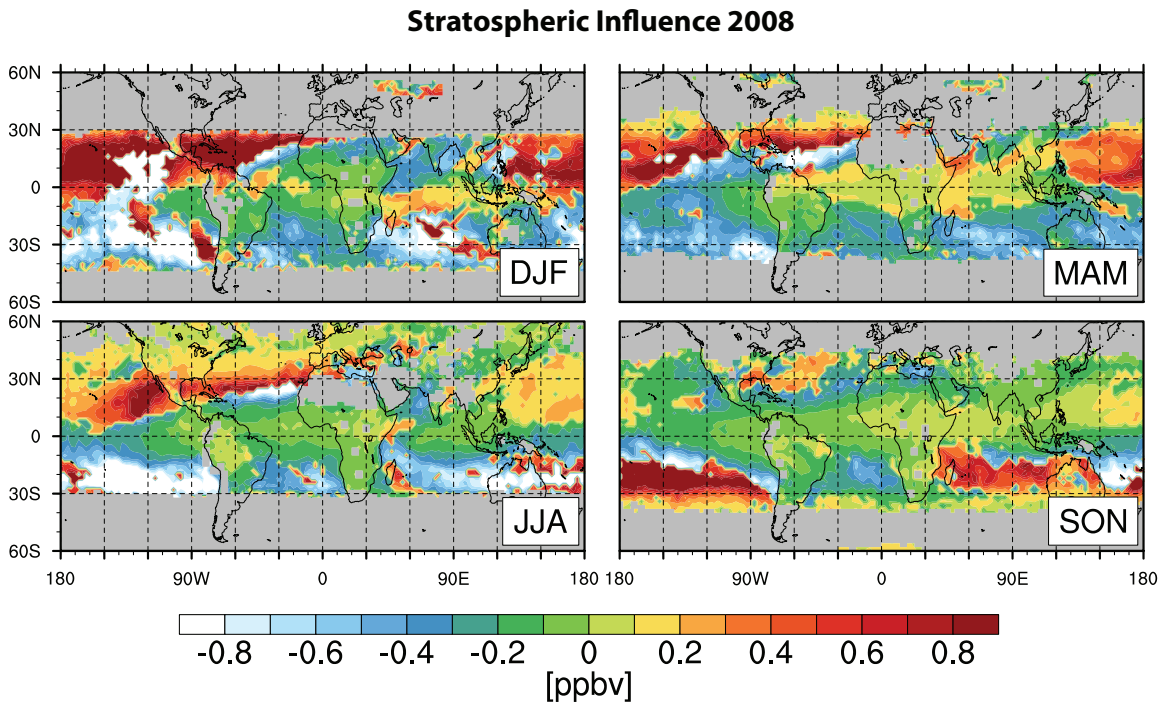

Figure **A.5**: Same as **Figure A.3** but for a simulation without stratospheric influence.

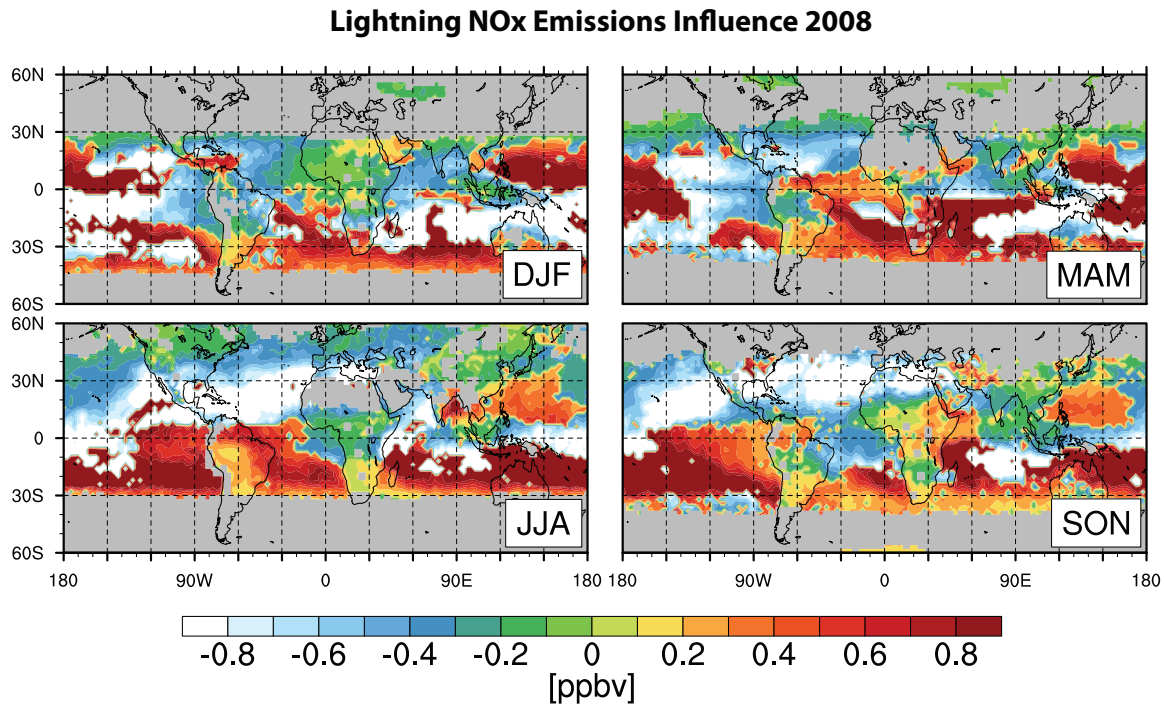

Figure A.6: Same as **Figure A.3** but for a simulation without lightning NO_x emissions.

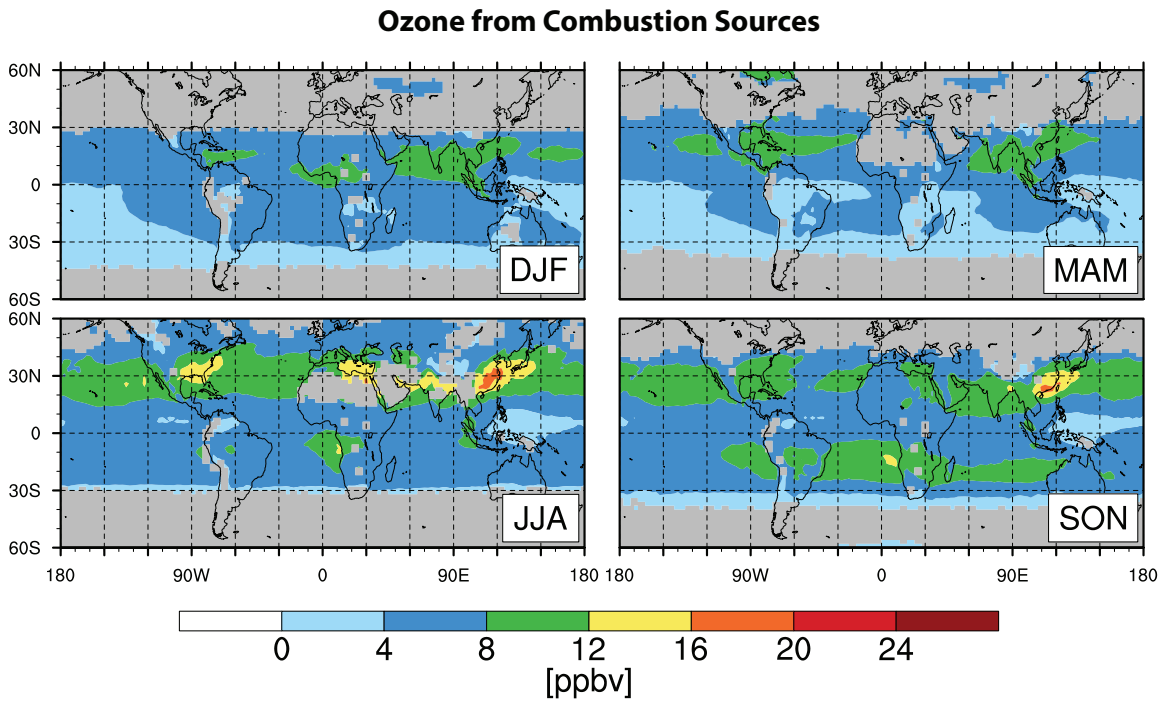

Figure A.7: Seasonal mean GEOS-Chem ozone mixing ratio enhancement from combustion sources at 700-400 hPa for 2008. The enhancement is the difference in ozone from the standard simulation and a simulation without combustion sources as in the right panel of **Figure 2.6** (ΔO_3). Gray indicates insufficient data (see Chapter 2).

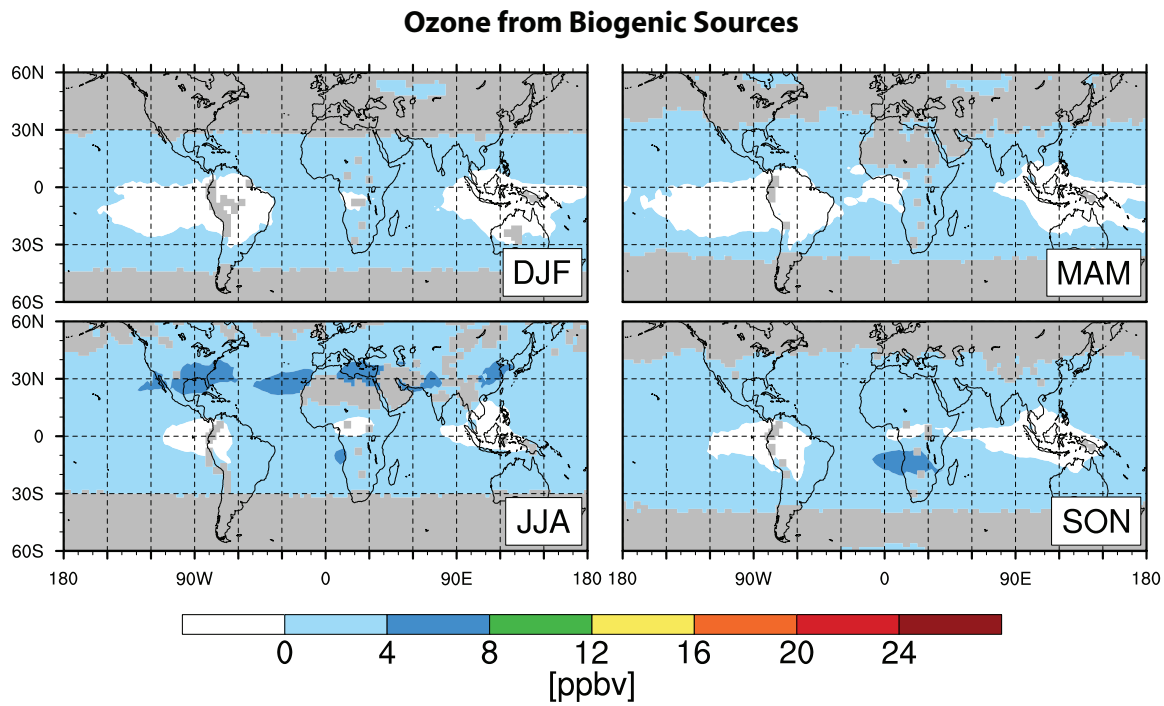

Figure A.8: Same as **Figure A.7** but for biogenic sources.

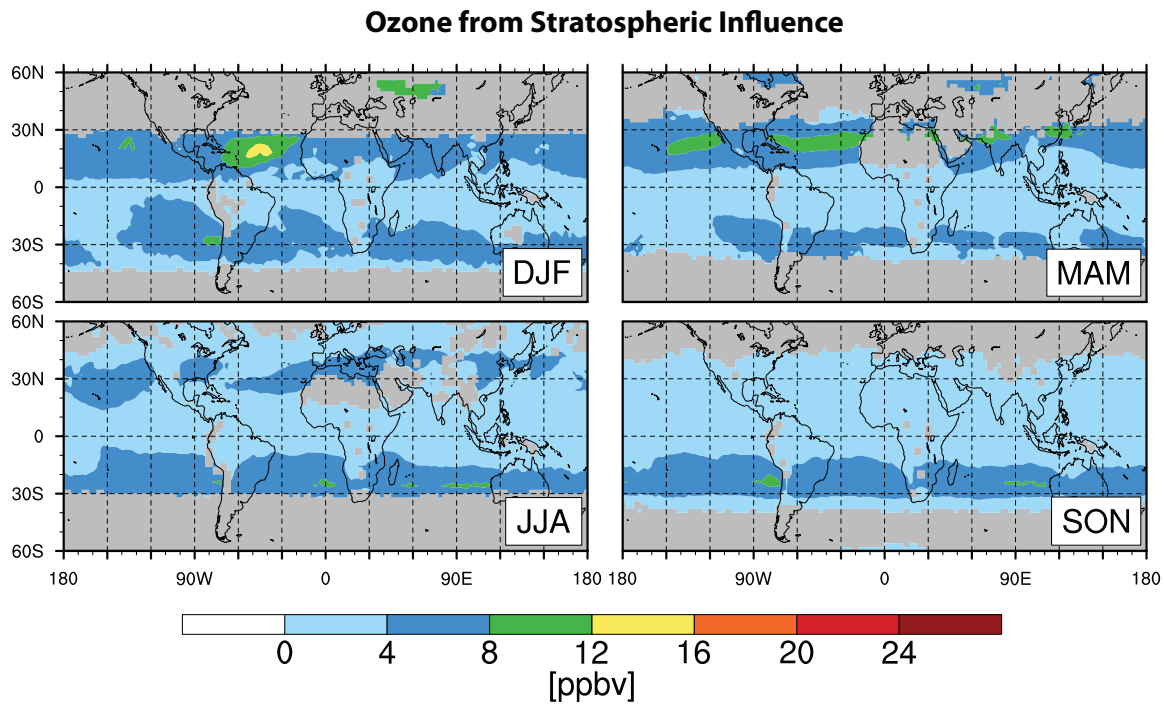

Figure A.9: Same as **Figure A.7** but for stratospheric influence.

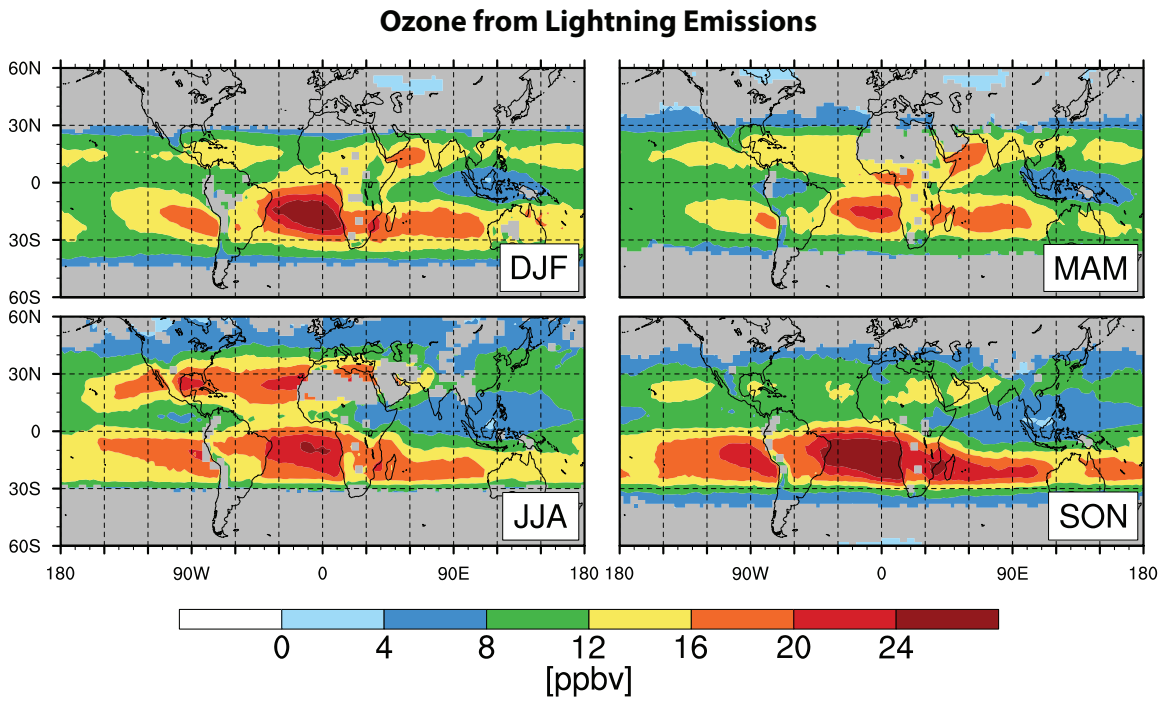

Figure A.10: Same as **Figure A.7** but for lightning NO_x emissions.

Table A.1: Ozone-CO correlations (and reduced major axis regression slopes in parentheses) from MOZAIC (green) and OMI/AIRS (yellow) at MOZAIC destination airports for each season of 2006. Also included below the statistics is the number of flights included in the analysis for each station and season (n). Gray indicates insufficient coincident data for statistical analysis (Chapter 2, Section 2.2.5).

Station	DJF	MAM	JJA	SON
Windhoek, Namibia	0.41 (0.47)	0.21 (0.35)	0.56 (0.31)	0.76 (0.21)
	0.35 (0.40)	0.02 (0.60)	0.49 (0.29)	0.57 (0.46)
	n = 12	n = 16	n = 54	n = 22
Portland, USA			0.15 (0.38)	
			0.49 (0.30)	
			n = 11	
Dallas, USA			0.46 (0.42)	
			0.03 (0.48)	
			n = 25	
Atlanta, USA			0.33 (0.36)	
			0.84 (0.50)	
			n = 10	
Philadelphia, USA			0.49 (0.32)	
			0.23 (0.36)	
			n = 10	
London, UK			0.27 (0.35)	
			0.13 (0.57)	
			n = 12	
Frankfurt, Germany			0.39 (0.31)	
			0.27 (0.60)	
			n = 27	
Vienna, Austria			0.54 (0.25)	
			0.49 (0.56)	
			n = 28	
Tokyo, Japan			0.43 (0.58)	
			0.63 (0.62)	
			n = 13	
Hyderabad, India				0.61 (0.35)
				0.33 (0.37)
				n = 14

Table A.2: Same as **Table A.1** but for each season of 2008.

Station	DJF	MAM	JJA	SON
Windhoek, Namibia	0.19 (0.53)	0.20 (0.32)	0.70 (0.20)	0.28 (0.32)
	0.20 (0.60)	0.05 (0.49)	0.61 (0.19)	0.23 (0.36)
	n = 14	n = 16	n = 51	n = 13
Frankfurt, Germany			0.40 (0.24)	
			0.69 (0.51)	
			n = 19	
Hyderabad, India				0.09 (0.70)
				0.20 (0.89)
				n = 10

Table A.3: 2008 seasonal mean AIRS CO and OMI ozone mixing ratios (ppb) and the corresponding GEOS-Chem values for all simulations for each region analyzed in Section 2.4.2 and shown in **Figure 2.7**.

	a) North Atlantic JJA	b) South Atlantic DJF	c) East Pacific SON
AIRS CO	86.3	98.9	86.2
OMI ozone	59.9	50.0	50.5
GEOS-Chem standard CO	81.5	100.2	80.3
GEOS-Chem standard ozone	63.8	52.6	52.7
GEOS-Chem ozone without combustion sources	52.1	45.3	43.6
GEOS-Chem ozone without biogenic sources	59.9	51.5	50.3
GEOS-Chem ozone without stratospheric sources	58.4	48.2	50.0
GEOS-Chem ozone without lightning NO_x	49.6	30.2	42.1

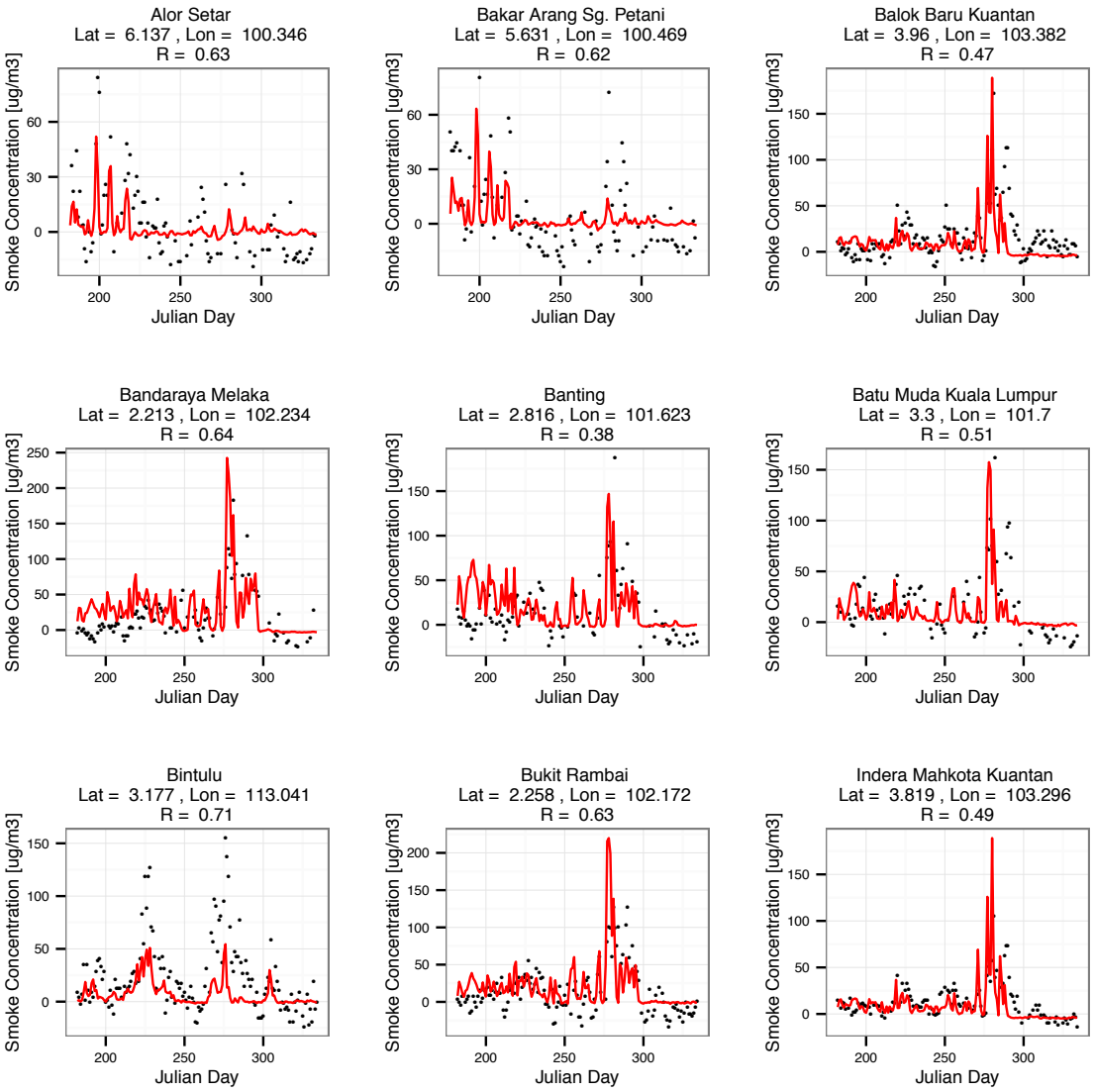

Figure A.11: Time series of observed and simulated 24-h surface mean smoke concentrations at all surface station sites for July – November 2006 (see Chapter 3). Observations are shown in black, GEOS-Chem in red. Site coordinates and temporal correlation coefficients are shown under each station name.

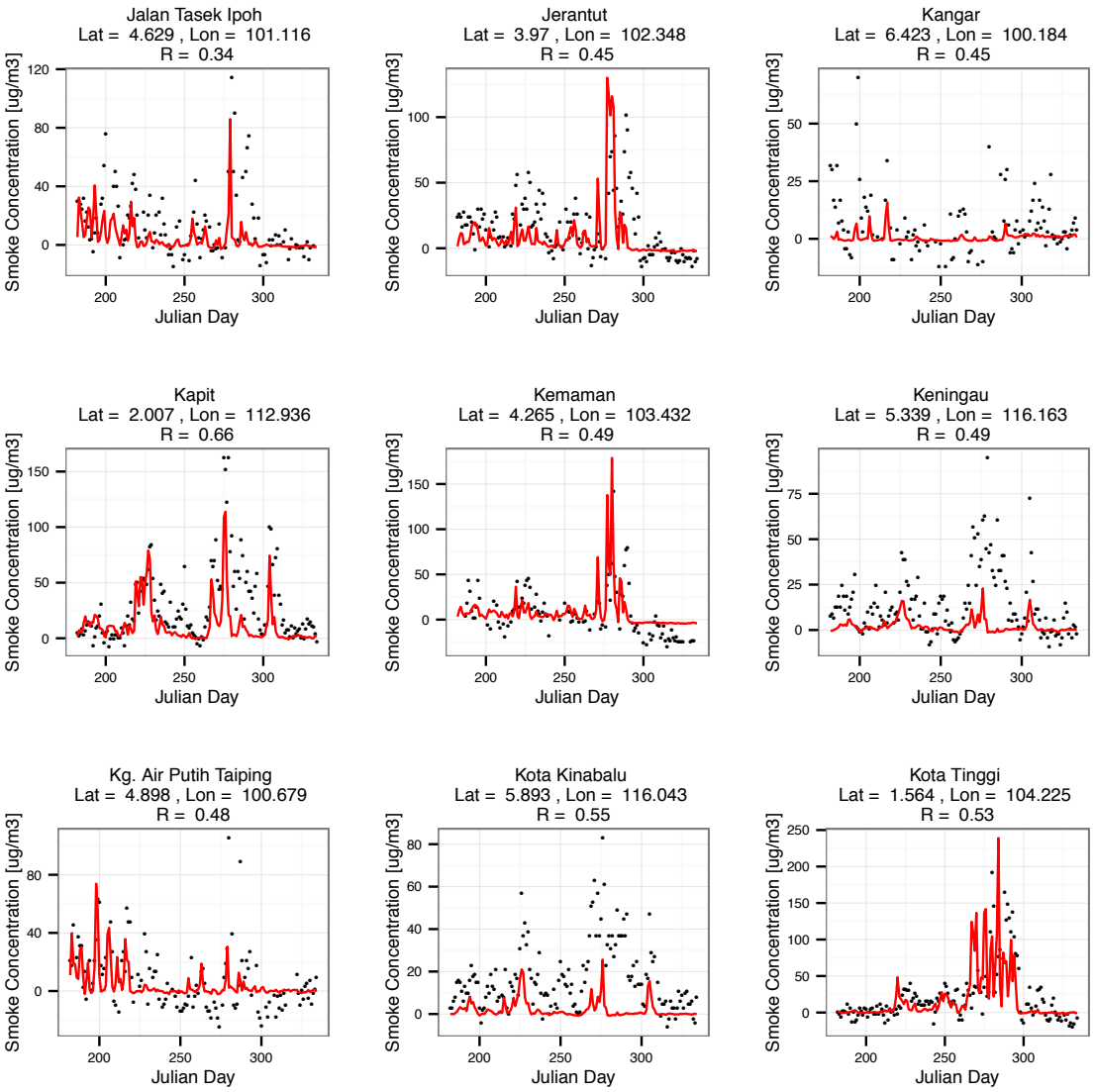

Figure A.11 (Continued)

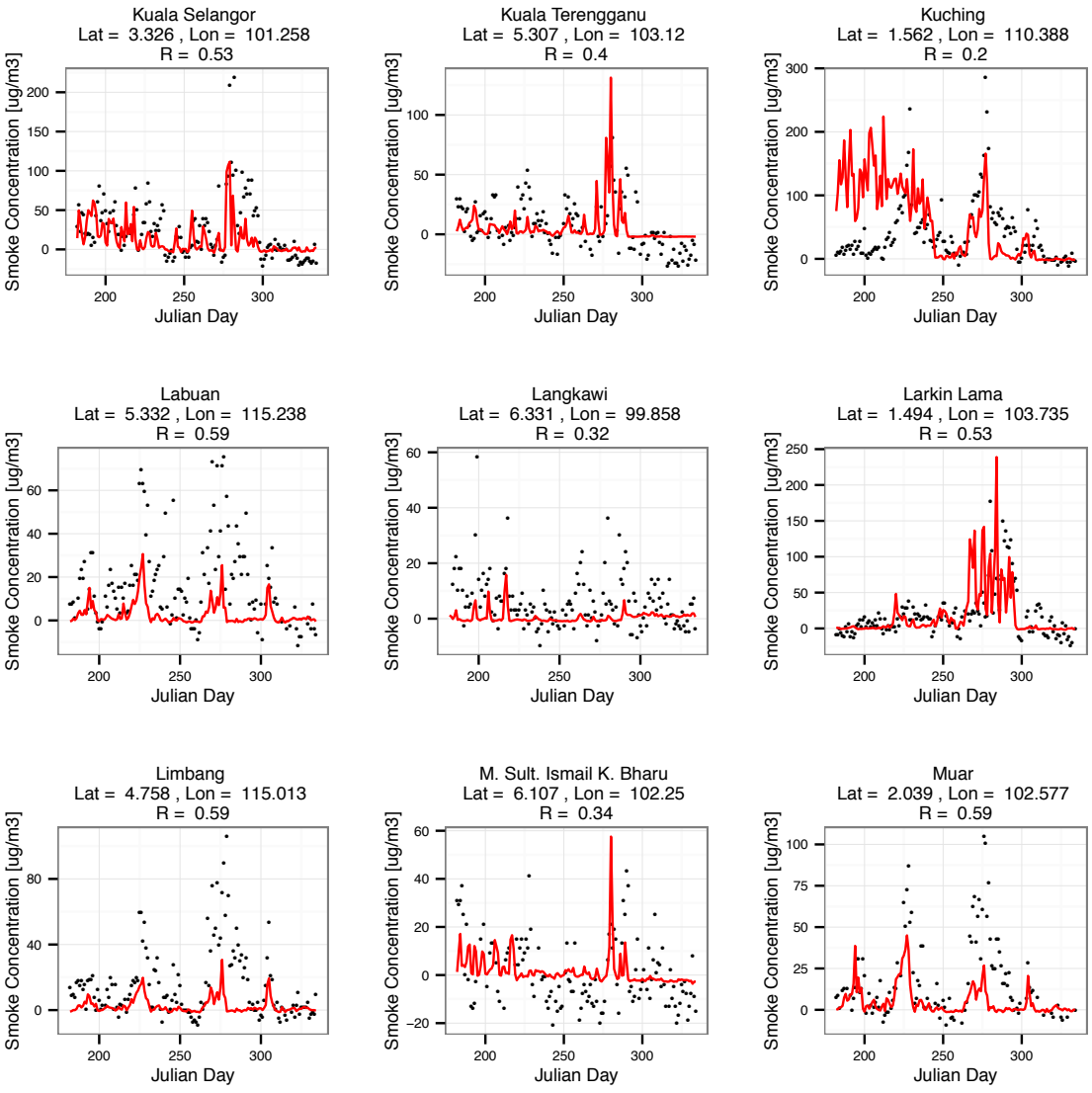

Figure A.11 (Continued)

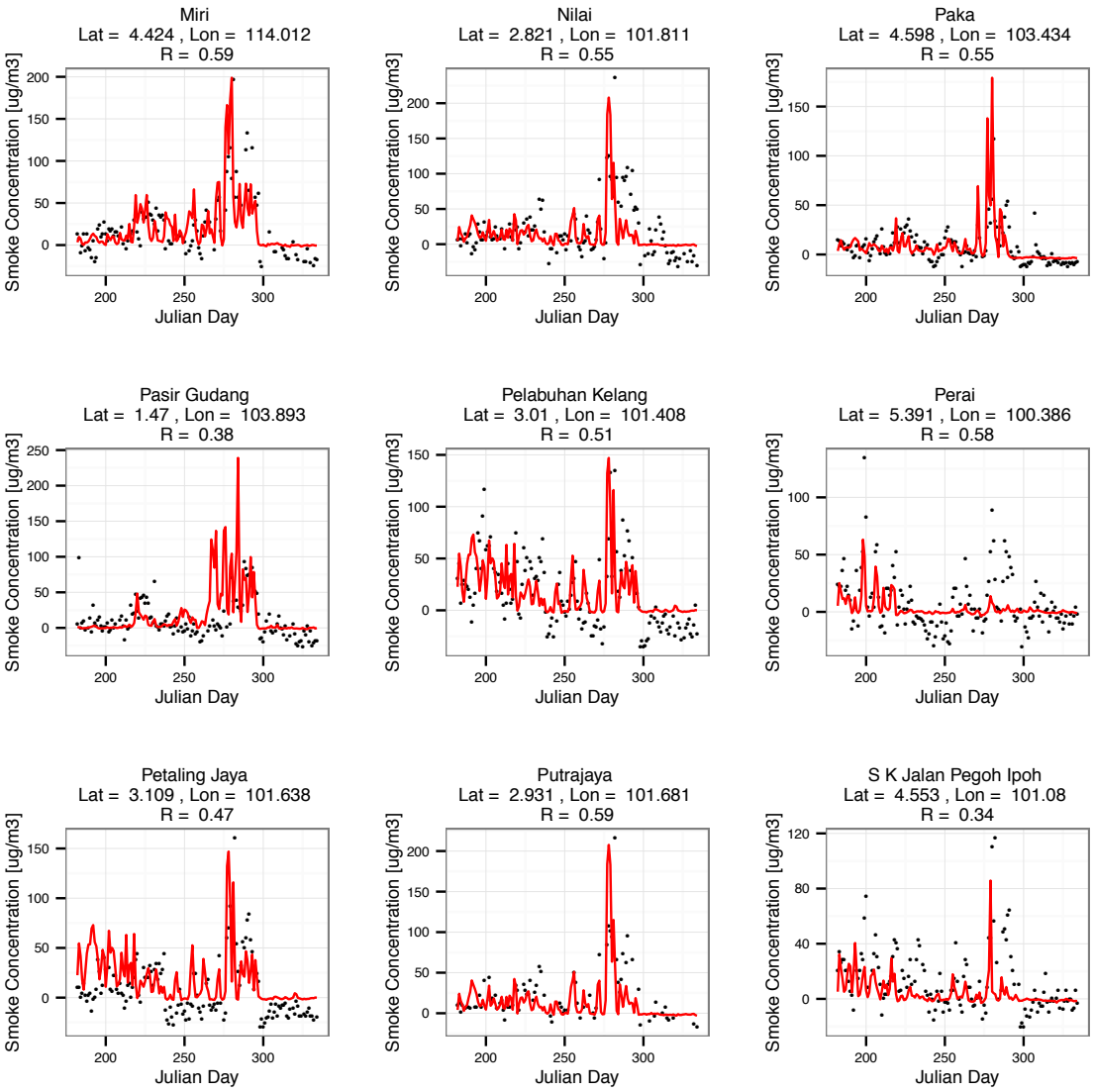

Figure A.11 (Continued)

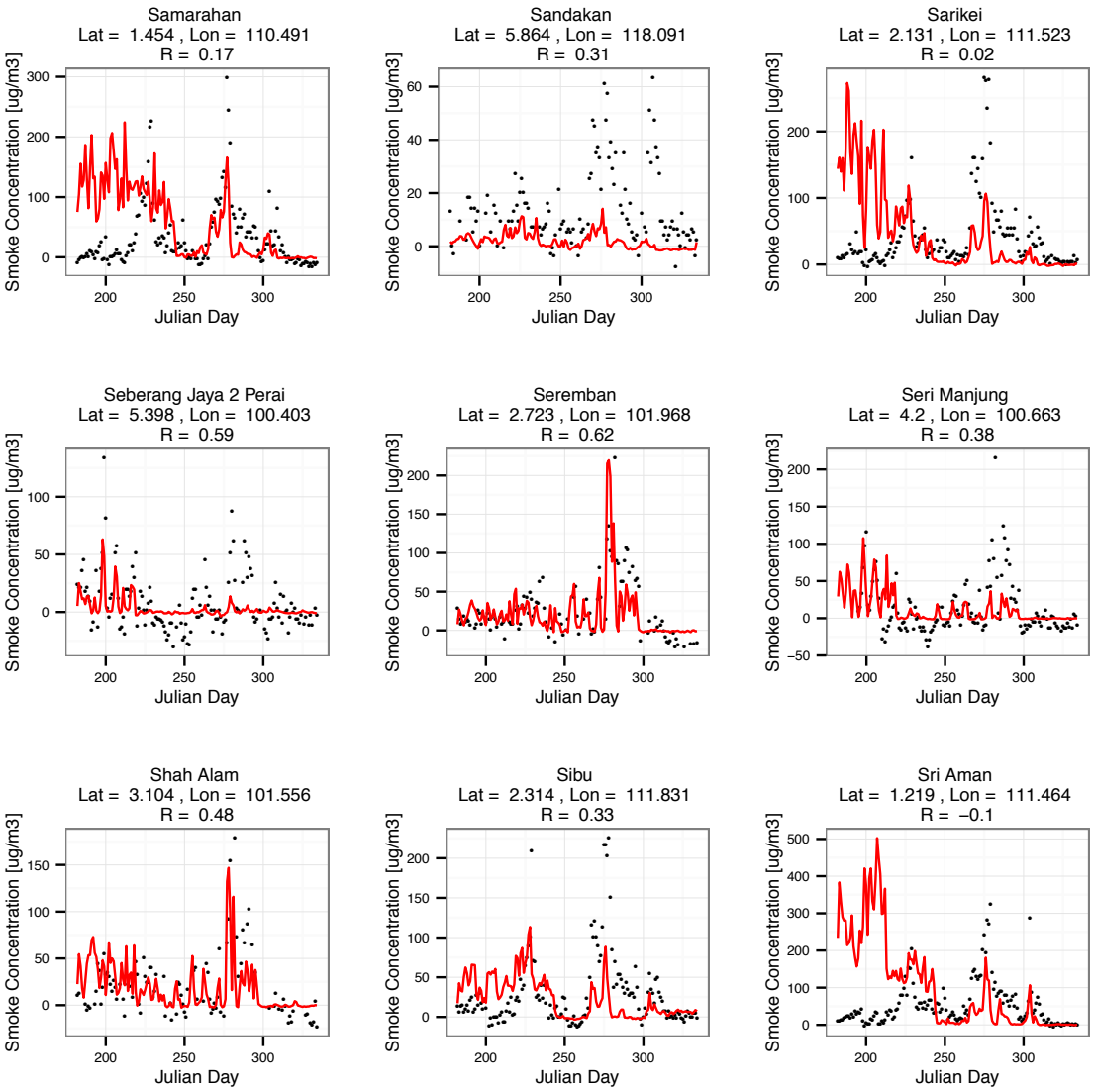

Figure A.11 (Continued)

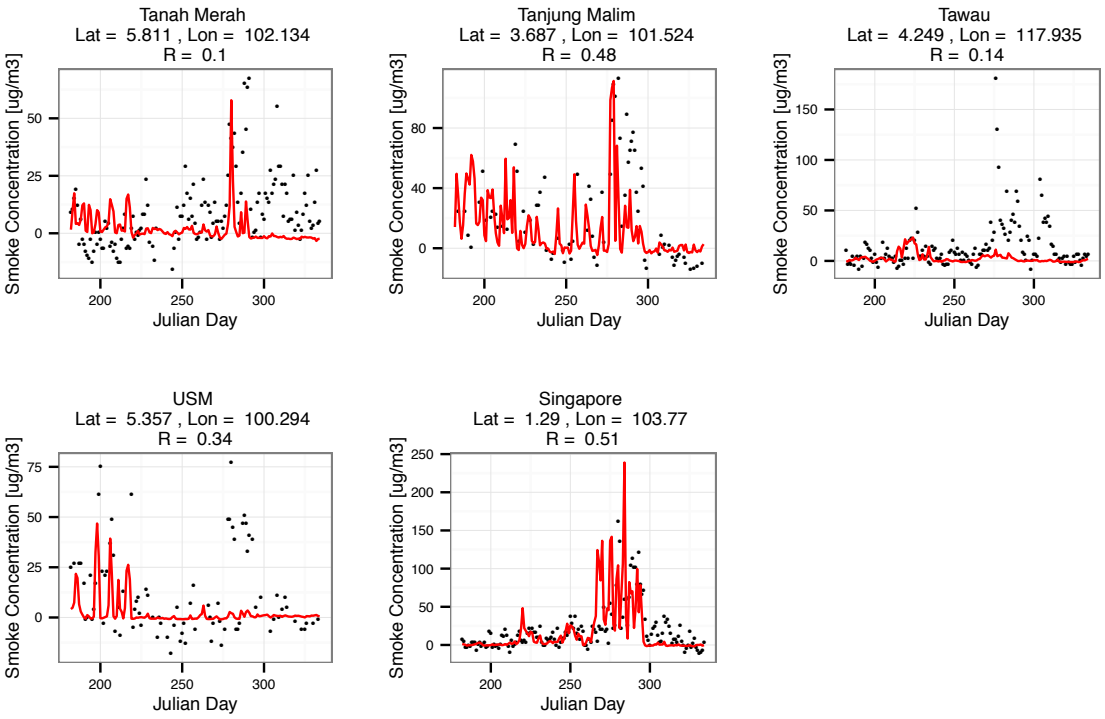

Figure A.11 (Continued)